Development of a High Speed, Robust System for Full Field-of-View 3D Shape Measurements

A Thesis
Submitted to the faculty
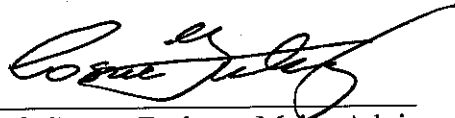of the

Worcester Polytechnic Institute

in partial fulfillment of the requirements for the
Degree of Master of Science
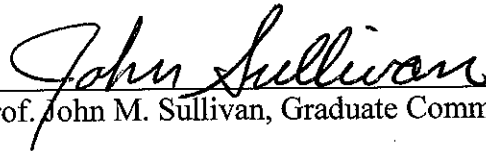in
Mechanical Engineering
by

Michael J. Zervas

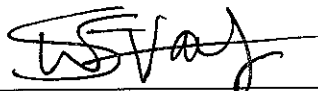22 August 2011

Approved:

_____
Prof. Cosme Furlong, Major Advisor

_____
Prof. John M. Sullivan, Graduate Committee Representative

_____
Prof. Ryszard J. Pryputniewicz, Member, Thesis Committee

_____
Prof. Simon W. Evans, Member, Thesis Committee

ABSTRACT

3D shape measurements are critical in a range of fields, from manufacturing for quality measurements to art conservation for the everlasting archival of ancient sculptures. The most important factor is to gather quantitative 3D information from measurement devices. Currently, there are limitations of existing systems. Many of the techniques are contact methods, proving to be time consuming and invasive to materials. While non-contact methods provide opportunities, many of the current systems are limited in versatility.

This project focuses on the development of a fringe projection based system for 3D shape measurements. The critical advantage of the fringe projection optical technique is the ability to provide full field-of-view (FOV) information on the order from several square millimeters to several square meters. In the past, limitations in speed and difficulties achieving sinusoidal projection patterns have restricted the development of this particular type of system and limited its potential applications. For this reason, direct coding techniques have been incorporated to the developed system that modulate the intensity of each pixel to form a sinusoidal pattern using a 624 nm wavelength MEMS based spatial light modulator. Recovered phase data containing shape information is obtained using varying algorithms that range from a single image FFT analysis to a sixteen image, phase stepping algorithm.

Reconstruction of 3D information is achievable through several image unwrapping techniques. The first is a spatial unwrapping technique for high speed applications. Additionally, the system uses an optimized Temporal Phase Unwrapping (TPU) algorithm that utilizes varying fringe frequencies ranging from 4 to 512 pixels per fringe to recover shape information in the time domain. This algorithm was chosen based on its robustness and accuracy for high resolution applications [Burke et al., 2002]. Also, unwrapping errors are minimized by

approximately 90% as the number of images used is increased from the minimum to maximum fringe density.

Contrary to other systems, the 3D shape measurement system developed in the CHSLT laboratories has unprecedented versatility to accommodate a variety of applications with the *z-depth* resolution of up to 25.4 µm (0.001 inches) and speeds close to 200 frames per second. Hardware systems are integrated into user-friendly software that has been customized for fringe projection. The system has been tested in two extreme environments. The first is for quantification of cracks and potholes in the surface of roads under dynamic conditions. The second application was digitization of an art sculpture under static conditions. The system shows promising results and the potential for high quality images via algorithm optimization. Most importantly, there is potential to present real time 3D information at video speeds.

ACKNOWLEDGEMENTS

TABLE OF CONTENTS

LIST OF FIGURES

LIST OF TABLES

NOMENCLATURE

SLM	Spatial Light Modulator
CCD	Charged Coupled Device
PC	Personal Computer
L	Length from the exit pupil of the spatial light modulator to the reference plane
FOV	Field of View
(O_c, X_c, Y_c, Z_c)	Coordinate axis of the CCD camera
(O_p, X_p, Y_p, Z_p)	Coordinate axis of the spatial light modulator
D	Distance between the spatial light modulator and CCD camera
φ	Wrapped phase calculated from the object and reference combined
$\Delta\varphi$	Phase difference - difference between the phase induced by the projection of the phase on the object and the phase induced by the projected fringes on a reference plane
φ_o	Wrapped Phase calculated from the reference plane
f_o	Spatial frequency of the fringes in appropriately scaled coordinates
Ω	Fringe Locus Function
Z_m	Height of the object as measured a point on the object to the reference plane
I_o	DC component of the 1D Fourier approximation
α_i	Induced phase shift
a	Image Brightness
b	Image Contrast
$I(x,y)$	Intensity Distribution
$\Delta\Phi$	Random phase
BHPF	Butterworth High-Pass Filter

BLPF	Butterworth Low-Pass Filter
D_o	Cutoff frequency
D(u, v)	Euclidian distance function
FFT	Fast Fourier Transformation
TPU	Temporal Phase Unwrapping
CAM	Computer Aided Machining
CAD	Computer Aided Design
DMD	Digital Micro-mirror Device
FPGA	Field Programmable Gate Array
ε	Error
DLP	Digital Light Projector
MEMS	Micro-Electro-Mechanical Systems
VOTERS	Versatile Onboard Traffic Embedded Roaming Sensors
NIST	National Institute of Standards and Technology
SOPRA	Surface Optical Profilometry Roadway Analysis
USPS	United States Postal Service
GPS	Global Positioning System
UPS	Uninterrupted Power Supply
FEM	Finite Element Modeling
RTI	Reflective Transformation Imaging
WAM	Worcester Art Museum

OBJECTIVE

This project is focused on the development of a 3D shape measurement system. The objective is to design, test, and evaluate the system in a variety of applications, such that the versatility and adaptability are unparalleled to current commercial systems. The system capability is demonstrated based on the novel techniques developed for full field-of-view 3D measurements.

1. INTRODUCTION

As technology continues to revolutionize every aspect of society, new opportunities for improved systems and devices present themselves. Particularly in the field of 3D shape measurements, great strides have been made to improve their speed, accuracy, and resolution. The relationship between a component structure and function is critical; thus, insight into 3D geometries provides advantages in a wide range of fields. Applications range from quantitative evaluation of manufactured components to periodic investigations of the structural integrity of existing components.

Current systems for shape measurements have several restrictions. The major disadvantage is that most techniques use contact measurement methods. This surface probing is invasive, time consuming, and potentially dangerous in some applications. Additionally, commercial systems have limiting constraints in terms of the size of the object, positioning of the system, and resolutions. Of particular importance is the development of a system that has the versatility and robustness to meet requirements for different applications.

This project focuses on the development of a novel shape measurement system at the macro level using noninvasive techniques for measurements under a wide range of conditions. The main advantage is that a single, all inclusive device has the resolution and speed to gather quantitative data sufficiently without exhausting expenses on another measurement system or software. The combination of a full field-of-view system with adjustable resolutions and acquisition speeds provides a unique system to those commercially available.

1.1. Importance of a 3D shape measurement system

To better design and manufacture an appropriate 3D shape measurement system, it's important to understand the need for such a device. Each field has its own use and particular application for the system. Correspondingly, the requirements for the system vary greatly according to the application as well. Prior to developing the 3D shape measurement system, these parameters must be explored and the system should be designed with each factor in mind to create an unmatched measurement device; thus separating the developed system from other commercial systems.

1.1.1. System parameters versus application

As a general overview, Z Corporation and the ZScanner^{TM} 700 provide a list of common applications and their major measurement criteria [Grimm, 2009]. Manufacturing is the first main industry to explore 3D measurement systems for a variety of reasons, including benchmarking and archiving of information. Also, regeneration of CAD models if they have been lost or do not exist is critical in design and development. This technology can be expanded into the healthcare industry as a quantitative method to evaluate medical and dental appliances. Also, personal prosthetics can be produced by improving ergonomics to fit the 3D shape of the measured patient. In art conservations and the entertainment industries, 3D measurements could be used for historic preservations or graphical designs and 3D visualizations, respectively.

Within each of the major fields, the applications consider seven main qualities that are outlined in Fig. 1.1. Each of these requirements deserves a more detailed description for a better understanding and to serve as a basis for the development of the current system. These outlined

parameters are the key driving factors in the design, manufacture, and integration of the system under development.
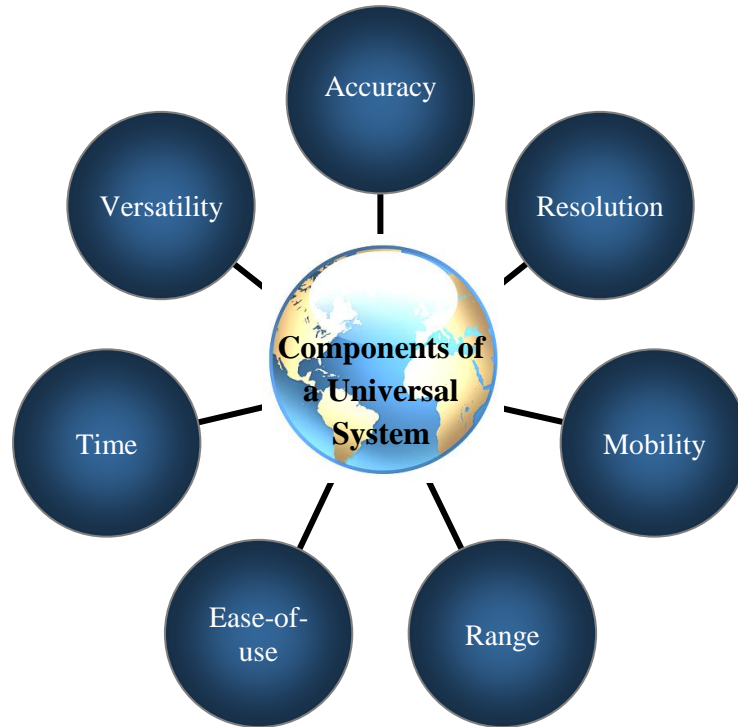
Fig. 1.1. System parameters based on a universal 3D shape
measurement system.

Accuracy of the system relates to how well the 3D data needs to fit the actual physical representation. Along the same lines, the required resolution relates to the maximum detail the system can recover. The mobility of the system describes how easily the system can be transported, setup, and calibrated for a measurement. In essence, the mobility is related to the portability of the system and in many cases is a critical factor in applications depending on the size, weight, and sensitivity of the object to be measured. The field-of-view (FOV) of the system

and depth of field are restrictions of the system's range. Differing measurement techniques will have variable range limitations.

Other factors include the measurement time once the system is set up and operational. This is critical in some instances, such as an assembly line type of application, were components may only have a few seconds to be scanned and benchmarked as part of the evaluation process. Higher speeds and advanced acquisition techniques must be able to handle time limitations. Additionally, incorporation into any commercial environment requires the system be user friendly and easy to operate. The operator must have an understanding of how it works and the tool must be intuitive so that measurements can be made quickly and easily. The final parameter is versatility. The system must be versatile in terms of the number of applications, size and complexity of the objects, and operating conditions.

Although not all of these factors are expected to be met in each and every application, they serve as a guideline for the development. Recognizing and understanding which of these factors is important in a particular application is critical. As an example, in benchmarking for manufacturing, the major criteria are the versatility, accuracy, and range of the system. In graphic design applications, the ease of use, time, and versatility are the most important characteristics.

Current commercial systems are designed with a single application in mind. For that reason, many consumers need to investigate current systems in detail and learn if their particular application fits into the specification. The novel aspect of the developed system is the ability to adopt itself to a variety of applications. In order to design an appropriate technology, an investigation of the current techniques is required.

1.2.   3D shape measurement techniques

There are a variety of techniques currently existing for 3D shape measurements. For simplification, the methodologies are separated into two main groups consisting of the contact methods and non-contact methods. The advantages and disadvantages of each method are described. As part of the design procedure, having an understanding of the current systems, aids in the development of the improved device for 3D shape measurements. Additionally, the advantages and disadvantages of each system in reference to the system requirements are explored to better define the development specifications.

1.2.1.   Contact measurements

A variety of contact systems have been developed based on varying applications. One of the most widely used systems for 3D measurements and tolerance verification is a coordinate measurement machine (CMM). This gives information of the *x, y, z* locations of an object by using a mechanical or optical probe. CMM's also provide information pertaining to an entire list of characteristics defining surface features [Engineers Edge, 2011]:

- Position

- Parallelism/ Perpendicularity/ Angularity

- Profile of a surface or line

- Straightness/ Flatness/ Circularity

- Cylindricity/ Symmetry/ Concentricity

- Datum qualification

One of the major disadvantages of the system is that gathering this type of information is exhaustive in both time and energy since, in many cases, the operation is manual. Additionally, this system is limited in applications because it is dependent on the size of the object that can fit into the measurement system. One sample system by Assurance Technologies, Inc is shown in Fig. 1.2.

Fig. 1.2. Tesa Micro-Hite 3D Coordinate Measuring Machine [Engineers Edge, 2011].

In an application for art conservation, ancient sculptures and statues for digitization come in all sizes, many of which can be very large and very fragile. Portable CMM systems can provide measurements on these objects that are not easily repositionable. Yet, even this portable system has major limitations in terms of measurement speeds and can potentially damage sensitive objects.

The contact methods previously described have a varying range of resolutions and are applicable only to certain measurements. In general, improvements can be made on the speed

and versatility of the 3D measurement system, while retaining the high measurement quality. Yet, the applicability of direct contact measurements is minimal as compared to non-contact measurements for their many advantages.

1.2.2. Non-contact measurements

Noninvasive techniques for surface measurements have become paramount for quality analysis in industrial applications, art conservation and restoration, as well as precision aid in medical procedures. Continued development of a structured light measurement system enhances the versatility, applicability, and repeatability required by industry. Additionally, integration of 3D measurement techniques with computer aided design (CAD) software and computer aided machining (CAM) equipment provides opportunities for reverse engineering [Whitehouse, 1997]. Although this technique is promising, limitations in speed and projection patterns have restricted many systems and their potential applications.

Non-contact methods can provide many advantages over typical contact methods. First, non-contact methods utilizing optical techniques prove to be an extremely versatile measurement method. Within the engineering field, it has been used to solve problems in mechanics and manufacturing technologies, while being used for nondestructive inspection [Cloud, 1998]. With advancements in laser technology and high speed cameras with unmatched resolutions, optical techniques provide endless opportunity in fields beyond just engineering. Other potential areas include art conservation and forensics. The emerging strides in data acquisition and processing provide even greater potential for these types of systems. Some of the commonly known optical

techniques are outlined. Required specifications that directly lead to choice of the currently developed system are explained. Non-contact optical techniques can be classified into several categories:

- Imaging techniques

- Time-of-flight techniques

- Structured light techniques

1.2.2.1. Imaging techniques

Imaging techniques, classified as photogrammetry, use multiple sets of 2D images to recover 3D information. The basic idea is that the 3D positions can be determined knowing one corresponding location on an image. Factors that can be used to recover the shape include shading, focus, and reflectance between images. A similar method called stereoscopy creates the illusion of depth by simulating offset of 'eyes' by using two offset 2D images and the use of special glasses to filter the images [Dodgson, 2003]. The major disadvantage of these techniques is that 3D information is only estimated and there are difficulties in correlation of points, or correspondence, between images. As a result, high resolution and accuracy are difficult to achieve. Yet, the basic technology seems promising as a non-invasive, potentially high speed, measurement system [Dornaika and Hammoudi, 2009].

1.2.2.2. Time-of-flight techniques

Time-of-flight techniques are based on the amount of time a laser pulse takes to get from the system, to the object, then back to a sensor. Using simple mathematics the distances from the system to the object can be recovered. Taking points at multiple locations the 3D information can be used to reconstruct a CAD model of the object. Up to 100,000 points can be measured per second and the system can be used over long distances, on the order of kilometers [Schuon et al., 2008]. One of the disadvantages of this system is that accuracies are compromised because the exact time-of-flight is difficult to determine. Also, errors occur when the pulse hits a point with a large slope because the pulse is essentially averaged, arising to inaccuracies in the measurement. Additionally, the object must remain unmoved during the point measurements, as vibrations or motions will cause invalid reconstruction of 3D information via stitching methods. In many applications pitch or tilt information is required, which can be determined directly using a full field of view system, but is not easily decoded via time-of-flight measurements. Full FOV 3D measurements are difficult with this type of system.

1.2.2.3. Structured light techniques

Structured light techniques are similar to the imaging techniques previously explained. Yet, many of the difficulties in correlation of points are eliminated by utilizing the combination of a projection system and camera. By projecting patterns onto an object and viewing how they deform on the object, 3D points in space can be determined via the method of triangulation from the angle between the projector and camera. There are various methods of coding each pixel to

extract depth information at each point over a full field-of-view. By incorporating wave optic techniques based on interferometry, accuracies of the system can be improved greatly. One particular method is called fringe projection, where phase shifting is incorporated into the system to obtain resolutions on the order of one hundredth of a wavelength.

1.3. System selection

The fringe projection – structured light technique for 3D shape measurements was chosen for development because it offers supreme benefits over other methods for several reasons. Most importantly, it provides high resolution results. Additionally, the FOV accommodates many applications, on the order of mm^2 to m^2. The system has the potential to be used in high speed applications, since it can gather full FOV information in the capture of a single frame. The incorporation of a high speed camera offers even greater potential for measurement of dynamic scenes.

Another key feature of this technique is that it provides the greatest potential for improvement as compared to the other techniques particularly from the projection pattern. The development of the system must have the versatility to accommodate a variety of applications and variations of the projection pattern or technique provides an opportunity to meet this design criterion. The objective is to research and develop a system that can be applied to a variety of fields because there is a great potential for 3D shape measurements in all areas. Understanding the importance of a versatile system is critical in determining the design constraints for the development of the system mechanically, electrically, and in regards to programming.

Through a clear understanding of the principle of structured light projection and the availability of advanced technologies, a procedure has been developed to understand and utilize the key criteria and accommodate the system based on these parameters. A detailed explanation of how the novel system works and how it was manufactured and packaged for use in several applications is described in forthcoming chapters.

2. PRINCIPLES OF STRUCTURED LIGHT PROJECTION

Structured light projection is a technique for recovering shape information as Cartesian *(x,y,z)* coordinates of an object surface. By inducing a known phase shift, the measurement precision can be improved. The most common method of structured light projection is fringe projection. The major advantage of fringe projection over other optical techniques is to provide full field of view information at high resolution based on the method of triangulation. Additionally, camera video speeds are used for gathering and processing information. The fringe projection technique has become popular in a wide range of fields and for a variety of applications. Similar systems have been designed for the inspection of wounds, characterization of MEMS components, and many other kinematic applications that relate to shape and position of a moving object [Gorthi and Rastogi, 2010].

2.1. Basic configuration

The ability to recover 3D information from structured light techniques is highly dependent of the system configuration. The developed system utilizes an off axis setup with a projector and camera. A schematic is shown in Fig. 2.1, where the spatial light modulator (SLM) projects a pattern onto an object that is recorded by a camera separated by an angle. System sensitivity increases with larger angles, but is more susceptible to unresolvable areas caused by shadowing [Bothe et al., 2002], [Xiaobo et al., 2008].
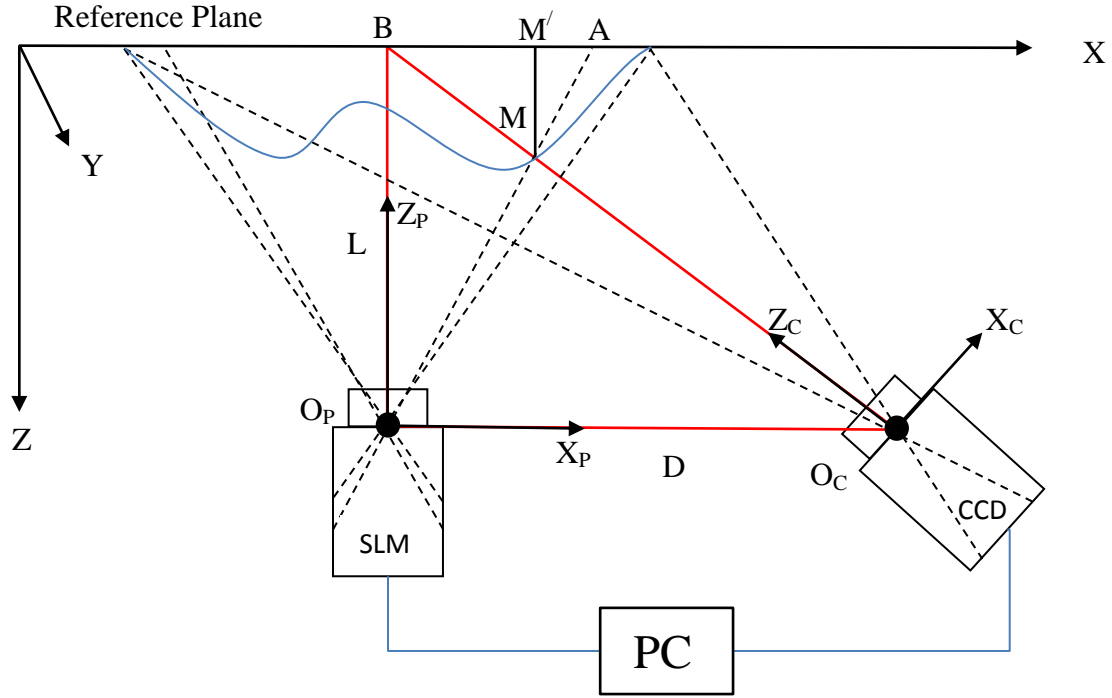
Fig. 2.1. Schematic of fringe projection system being developed with the CCD camera separated by a triangulation angle from the spatial light modulator (SLM).

Triangulation is the key concept used to determine the height of the measured object, which is directly related to the configuration of the CCD and SLM [Xiaobo, 2008]. In Fig. 2.1, each component of the system is represented in its appropriate coordinate axis, where O_P and O_C represent the origins of the projector and camera coordinate systems, respectively. The distance from the projector to the camera, D, is known, as well as the distance from the pupil of the projector to the reference plane, L. The camera and projector intersect at a point, M, on an object. Knowing that triangles $\Delta O_P M O_C$ and ΔAMB are similar, we can write:

$$\frac{\overline{AB}}{\overline{O_C O_P}} = \frac{\overline{MM'}}{L - \overline{MM'}} \, .$$

(2.1)

The height of the object, Z_M, is equivalent to the distance between the object and the reference plane, i.e.,

$$Z_M = \overline{MM'} .\tag{2.2}$$

It's important to note that the reference plane is related to one of two planes – a physical plane recorded and subtracted from the measured phase value or a mathematically removed plane that is subtracted from the measured phase value. In either case, the relation between one point and another in the measured data is the same. The only difference lies in the 2π modulation that occurs from the nature of fringe projection, which introduces a mathematical plane. The phase variation can be calculated as a function of the position shift of the projected light ray on the reference plane [Su and Zhang, 2010]:

$$\Delta\varphi = \varphi - \varphi_0 = 2\pi f_0 \overline{AB} ,\tag{2.3}$$

where the change in phase, $\Delta\varphi$, is the difference between the phase induced by the projection fringes on the object, φ, and the phase induced by the projected fringes on a reference plane, φ_0. f_o is the spatial frequency in scaled coordinates. Solving Eq. 2.1 for AB and using the relation from Eq. 2.2 results in AB in terms of Z_M:

$$\overline{AB} = \frac{dZ_M}{L - Z_M} .\tag{2.4}$$

Based on Eq. 2.4, the solution for the value of Z_m gives the height of the object of interest:

$$Z_M = \frac{L\Omega}{2\pi f_0 D + \Omega} ,\tag{2.5}$$

where Ω is the unwrapped phase. In many cases, the distance of the system to the object, L, is much larger than height distribution, Z_M. Thus, Eq. 2.5 can be modeled as a linear relation:

$$Z_M = \frac{L\Omega}{2\pi f_O D} \ .$$

(2.6)

A comparison between the linear and nonlinear model and its relation to calibration techniques is analyzed by [Jia et al., 2007]. Mathematically, and by looking at Fig. 2.1, the larger the angle, the higher the sensitivity of the system because the triangle formed from the object to the reference is better defined. This is directly related to the accuracy of the system in resolving the height distribution and the determination of triangle ΔAMB. A realization of the setup in the laboratory environment is shown in Fig 2.2.
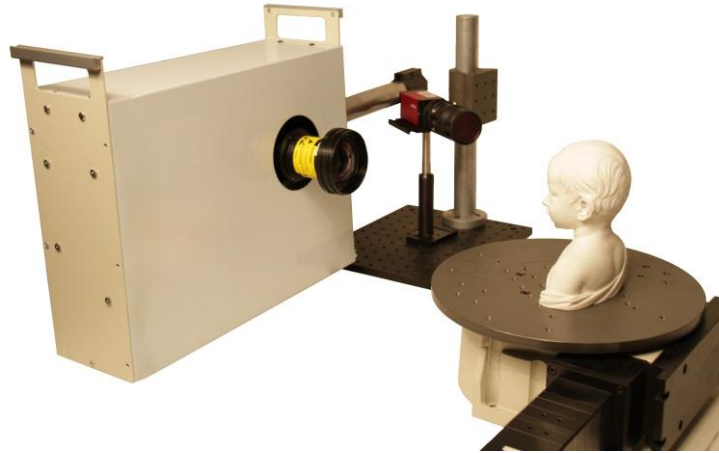
Fig. 2.2. Realization of our system with an art sculpture under examination.

The physical setup is one component that affects the accuracy of the system. Other factors are related to the advancements in the spatial light modulator technology and camera technology. Additionally, defining the best projection technique is critical to recover the highest quality

images. Research has been done on the projection technique and how it relates to image quality. An investigation of projection techniques is critical to an understanding of how to gain the highest quality images while still having the versatility to accommodate different applications.

2.2. Projection techniques

Different coding strategies exist in structured light projection to produce a pattern or group of patterns that can be used to extract 3D shape information. Classifications of these projection codes have been outlined and categorized into three major groups [Salvi et al., 2004]:

- Time Multiplexing

- Spatial Neighboring

- Direct Coding

A basic understanding of the advantages and disadvantages of each of these methods provides a well-rounded investigation of the chosen projection pattern as related to the objective of the developed system. Most important is the integration of the projection pattern as related to the advanced system components.

2.2.1. Time multiplexing

The time multiplexing technique uses a set of binary images that are projected onto an object that vary temporally. The very basic projection method is the binary system that uses a single spatial frequency of the fringes that varies by only two levels, 0 or 1, corresponding to

completely dark or completely light vertical bands, Fig. 2.3. Summation of the binary values at each pixel level creates a binary sequence, or code word, for each particular pixel [Salvi et al., 2004].

<div align="center">(a)   (b)</div>
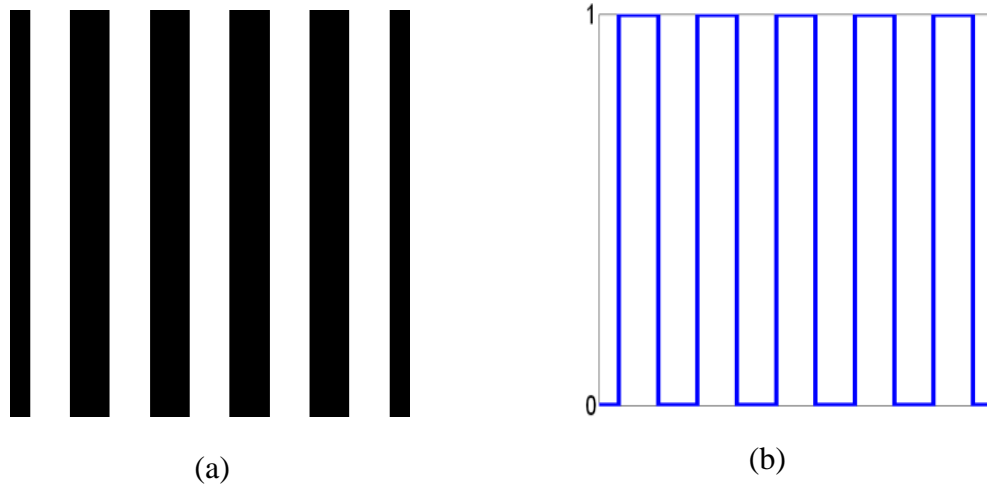
Fig. 2.3. One type of projection pattern: (a) 2D binary image; and (b) corresponding cross section.

This technique can be improved by implementing gray code, or reflected binary code, to more accurately extract 3D information. The advantage of gray code is that one value in the binary sequence changes between neighboring values, corresponding to a hamming distance of one, to thus discretize pixels with certainty rather than the ambiguity that arises in binary code. Depending on the bit level, more density variations can be acquired by varying the spatial fringe frequency in time, Fig. 2.4. The maximum number of patterns that can be projected using this binary method is the maximum resolution of the system, which is also directly related to the line pairs per millimeter (lp/mm) of the camera-lens system. The disadvantage of this method is particularly clear in high speed applications because large sets of images are needed for projection. This technique is not applicable for dynamic situations. Additionally, the resolution

<div align="center">17</div>

of the system is compromised by the resolution of the projection system and phase shifting must be used to improve resolution. An example sequence of gray code is shown in Fig. 2.4. Hybrid techniques include multiple pattern projects and phase shifting to improve spatial resolutions.
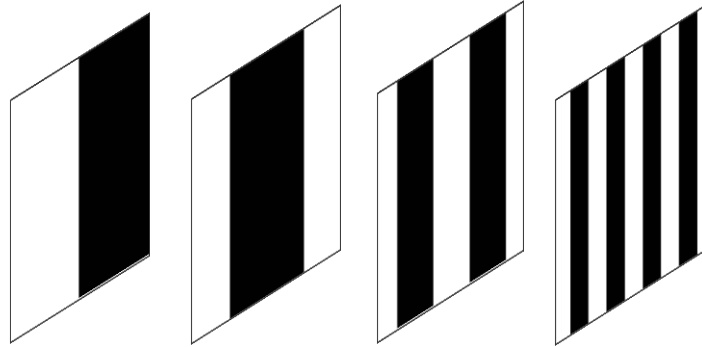
Fig. 2.4. Sequence of increasing density for time multiplexing technique using binary projection patterns.

2.2.2. Spatial neighboring

A second type of fringe projection method is through encoding all the information in a unique pattern. This type of spatial neighborhood technique is more complicated in terms of decoding information. Basically, the theory focuses on determination of pixel code words based on isolated regions from specified patterns. Algorithms must be implemented to decode the information based on a variety of parameters depending on the projection pattern.

The advantage of this sequence is the ability to measure dynamic events. Compared to time multiplexing, the spatial resolution is decreased and the codification and implementation is more complex. Additionally, there is a general assumption that the measured objects have a relative small gradient from point to point. Otherwise, errors are created from large discontinuities in the measurement surface [Salvi et al., 2004].

18

2.2.3. Direct coding

The final coding method is called direct coding, where pixels can contain given information of a certain location [Salvi et al., 2004]. One method is based on gray levels. By modulating the pixel, the intensity can be controlled and a gray level can be achieved. This method is highly sensitive to the stability and repeatability of the projection system for measurements. Inaccuracies in measurements can be due to noise and non linearities in the projection system. The main disadvantage is in the increased error when using commercial projection systems due to quantization effects from the projector resolution and bit depth [Xiaobo et al., 2008].

Another method is codification based on color. Using the full spectrum of RGB information the phase map can be calculated using 24-bit color images [Spagnolo et al., 2000]. Projecting each fringe pattern individually and isolating the channels the phase map is calculated. One factor to note is that cameras have a different absorption spectrum at different ranges of the wavelength. These factors directly affect the phase map, particularly when examining each color channel. Some methods use a combination of three-phase step contained in a single frame isolated by red, green, and blue fringes. Post-processing can be done to isolate each channel and perform the three-phase step algorithm. One of the major drawbacks of this method was directly related to the large bandwidth associated with the use of LCD projection systems that cause ambiguity among intensity values between pixels. Additionally, the effects of noise from the system play a large role in the applicability of this technique.

2.3. Fringe projection system

Based on the analysis of different structured light projection techniques, the method of direct coding provides the best resolution and accuracy along with high speeds. This technique has the potential to combine phase shifting for improved results and the versatility to accommodate high speed applications. Incorporation of this method into the development of the system requires an understanding of the mathematics behind fringe projection.

For fringe projection, sinusoidal patterns are critical because they minimize discontinuities and errors in the reconstruction algorithms. This project explores the mathematical importance of sinusoidal projections while analyzing their quality via quantification of processed images, which will help in the continued development of our system as a combined high-speed, high resolution versatile measurement device. From a mathematical standpoint, a 1D Fourier approximation, $f(x)$, contains only the summation of continuous cosine and sine approximations, with integration functions, a_n and b_n, discontinuities will appear as high frequency components [Zervas et al., 2011]:

$$f(x) = I_o + \sum_{n=1}^{\infty} [a_n \cos(nx) + b_n \sin(nx)] . \tag{2.6}$$

A theoretical sinusoidal fringe pattern projection, Fig. 2.5a, shows a corresponding cross section and power spectrum, in the frequency domain. The center DC component with a frequency component based on the number of fringes is shown. Figure 2.5b shows a resulting power spectrum of a square wave projection with many other higher frequency components that do not contain any shape information, but can be regarded as noise from the discontinuous square function. The energy density for a sinusoidal projection and square wave with a

frequency of one fringe are 694 and 1351, respectively, proving that sinusoidal fringe projection results in better image resolutions.
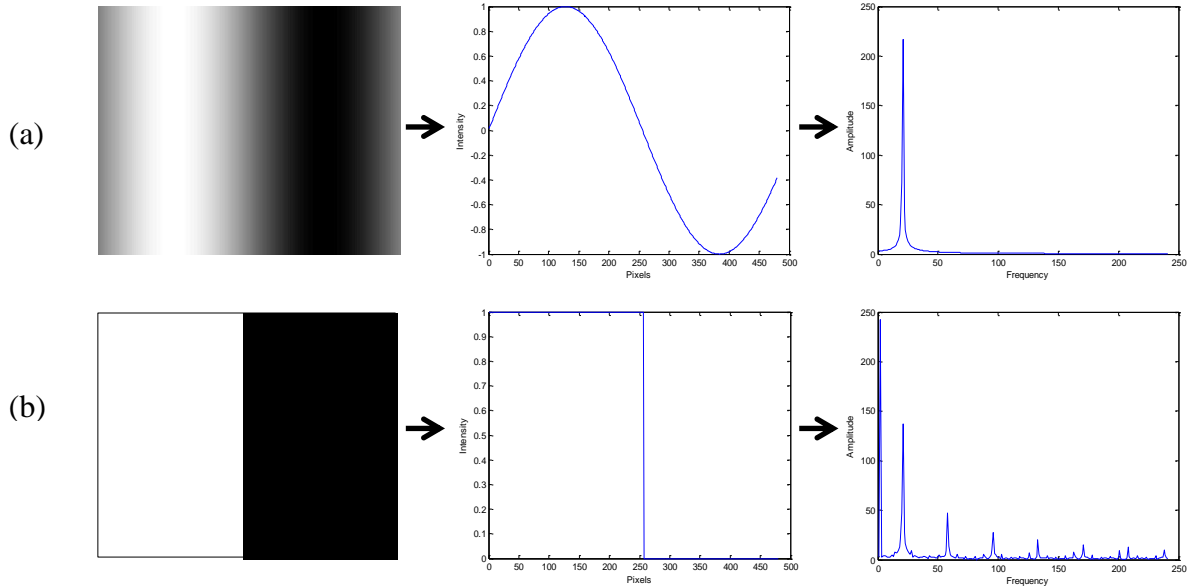
Fig. 2.5. Projected fringes: (a) 512 x 512 sinusoidal fringe projection pattern with a sample cross sectional area and power spectrum; and (b) 512 x 512 square projection pattern, cross section and power spectrum.

The greatest compromise of speed and quality lie in a dynamic system that projects sinusoidal patterns. Phase stepping can greatly improve the quality of the 3D information. Incorporating a series of acquisition methods into the system can make it adaptable and versatile to a number of different applications. In particular, the major advantage of the developed technique is that it uses this higher resolution sinusoidal fringe projection. Contrary to many other methods, the incorporation of this method with phase shifting separates it amongst other systems and results in much higher quality and resolution images, as explained in further details in the chapters that follow.

3. OPTICAL PHASE CALCULATION AND UNWRAPPING

An understanding of the basic system configuration is an initial step in the development of the 3D shape measurement system. A more detailed understanding of the acquisition and unwrapping processes for recovering 3D information is required. To gather information in versatile conditions, at high speeds and high resolutions, different algorithms must be implemented. An understanding of signal processing is essential for maximizing image quality.

3.1. Interference phase equation

Each image that is captured by the camera is defined by a matrix representing the intensity value at each pixel [Kreis, 2005]:

$$I(x,y) = a(x,y) + b(x,y)\cos[\Delta\Phi(x,y) + \Omega(x,y) + \alpha_i] \,, \tag{3.1}$$

where the recorded intensity distribution, I, is a function of the brightness, a, the amplitude, or contrast, b, the random phase, $\Delta\Phi$, the known induced phase shift, α_i, and the fringe-locus function, Ω, containing shape information for each pixel (x, y). In most cases, the changes in a, b, and $\Delta\Phi$ vary slowly as compared to the carrier frequency due to the synthetically introduced fringes [Takeda et al., 1981]. A least-squares method can be used to solve for Ω by minimization of the summation of quadratic errors [Kreis, 2005]. In general, increases in the number of phase stepped images used to recover phase information, decreases random electronic noise and inaccuracies in phase shifting, $\Delta\Phi$. Using more images for reconstruction increases the measurement and processing time, but could be advantageous to particular applications that are not time critical.

3.2. Fast-Fourier Transform (FFT) single frame phase calculation

For high speed applications, single images must be used to recover 3D information. A Fast-Fourier Transform (FFT) evaluation is one technique for acquiring phase information via a single image. Processing is done on a captured image with sinusoidal fringes projected onto the object of interest. The density of the fringes is chosen based on the FOV and desired resolution. The FFT essentially fits a sequence of harmonic spatial functions with increasing frequency to the acquired image, which converts the data from the time domain into the frequency domain. The basis behind the theory is that a signal can be decomposed into a series of its sine and cosine functions.

Mathematically, the Fourier Transformation, $F(u)$, can be written in terms of the amount of each frequency that makes $f(x)$. The important characteristic of the Fourier Transform is that the spatial signal can be recovered by an inverse transformation:

$$F(u) = \int_{-\infty}^{+\infty} f(x)e^{-2\pi iux}dx \,, \tag{3.2}$$

$$f(x) = \int_{-\infty}^{+\infty} F(u)e^{-2\pi iux}du \,. \tag{3.3}$$

This phenomenon can be applied to a single image by utilizing Euler's identity shown in Eq. 3.4 to simplify Eq. 3.1:

$$\cos(\Omega) = \frac{e^{i\Omega} + e^{-i\Omega}}{2} \,. \tag{3.4}$$

Thus, Eq. 3.1 is rearranged for convenience into Eq. 3.5 and extended into 2D for image analysis.

$$I(x,y) = a(x,y) + c(x,y) + c^*(x,y) \,, \tag{3.5}$$

where

$$c(x,y) = \frac{1}{2}b(x,y)e^{i\Omega(x,y)} .$$
(3.6)

The complex conjugate is represented as c^* in Eq. 3.5. Applying a 2D FFT to the image results in the direct representation of the DC component, $a(u,v)$ and the spatial frequency, $c(u,v)$ and $c^*(u,v)$, Eq. 3.5. The information is now transformed into the frequency domain where it can be viewed as a function of the amplitude, also known as the power spectrum, Eq. 3.7.

$$F(u,v) = \sqrt{real\big(F(u,v)\big)^2 + imag(F(u,v))^2} .$$
(3.7)

Based on the Nyquist Sampling Theory, the summation is performed on half of the image pixel dimension, but the result is a complex number which means the total number of terms is the same as the input image size. The power spectrum, or magnitude, is the combined amplitude of the summations of sine and cosine functions. Since the analysis is done on a real signal, the FFT matrix is point symmetric with respect to the DC term at $I(0,0)$ [Kreis, 2005]. A sample FFT is shown in Fig. 3.1 with high density fringes on a sculpture. For viewing and filtering purposes, a logarithmic scale showing only the real components are plotted. Also, the zero-frequency component was shifted to the center of the image by shifting quadrants.
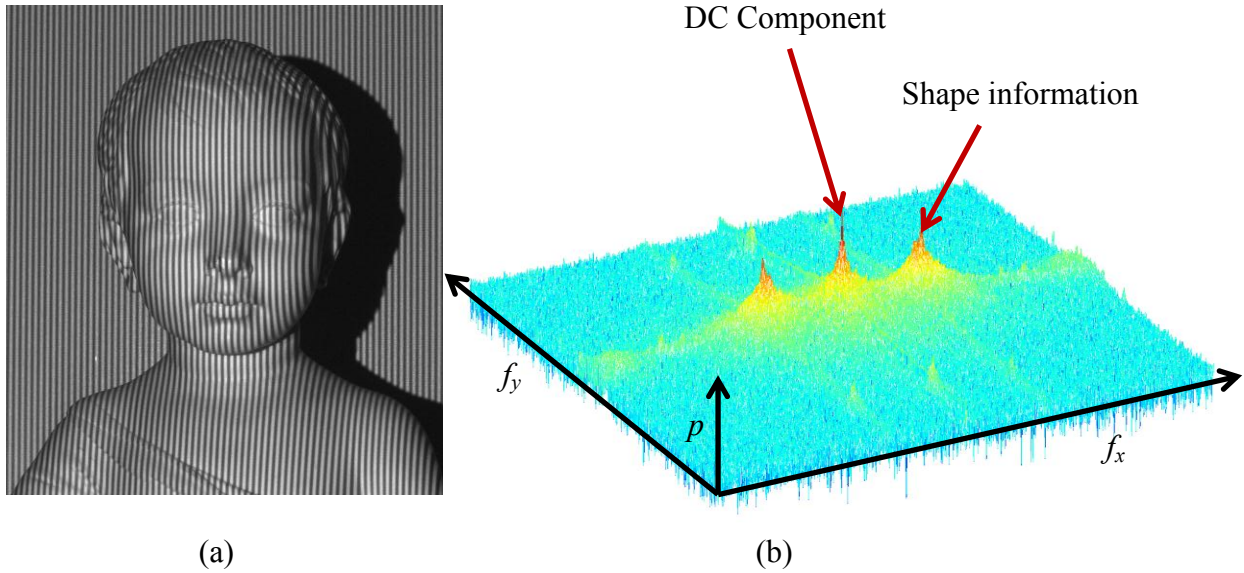
Fig. 3.1. Fast Fourier Transform of an image of a sculpture with fringes: (a) 2D image of a sculpture with fringes; and (b) corresponding 2D FFT showing the DC component and shape information contained within the power spectrum.

Typically, advanced analyzing software tools use a form of zero-padding that's added to the information matrix to reduce the processing time and more accurately represent a periodic function. Filters can be applied to the FFT to isolate only one peak containing the shape information of the deformed fringes. By shifting the FFT back to its original quadrants, the inverse FFT function can be performed to return the image back to its spatial coordinates. The phase map can be calculated as an arctangent function based on the relative proportions of sine and cosine, Eq. 3.8.

$$\Omega(x,y) = arctan\left[\frac{imag\big(c(x,y)\big)}{real\big(c(x,y)\big)}\right]. \tag{3.8}$$

It's important to note the relationship between the carrier frequency, f_o, and the density of the projected fringes. This carrier frequency can be seen in Fig. 3.1b, as the difference between

the frequency values of the DC component peak and shape information peak. Theoretically, the broader the fringe density, the lower order of the term that is needed to represent the fringe frequency and the closer the peak will be to the central DC component. The larger the fringe frequency, the higher order of the term that represents the fringes and the further away from the central DC component it will be, thus resulting in a larger carrier frequency. The resulting wrapped phase map can be seen in Fig. 3.2.

Fig. 3.2. 2π wrapped phase map via FFT method.

3.2.1. Image filtering techniques

An understanding of signal processing and image filtering is required to successfully calculate the phase via the FFT method. There are two major types of filters, one called a low-pass filter and the other called a high-pass filter, both of which can be observed in Fig. 3.3.

(a)　　　　　　　　　　　　　　　　　(b)
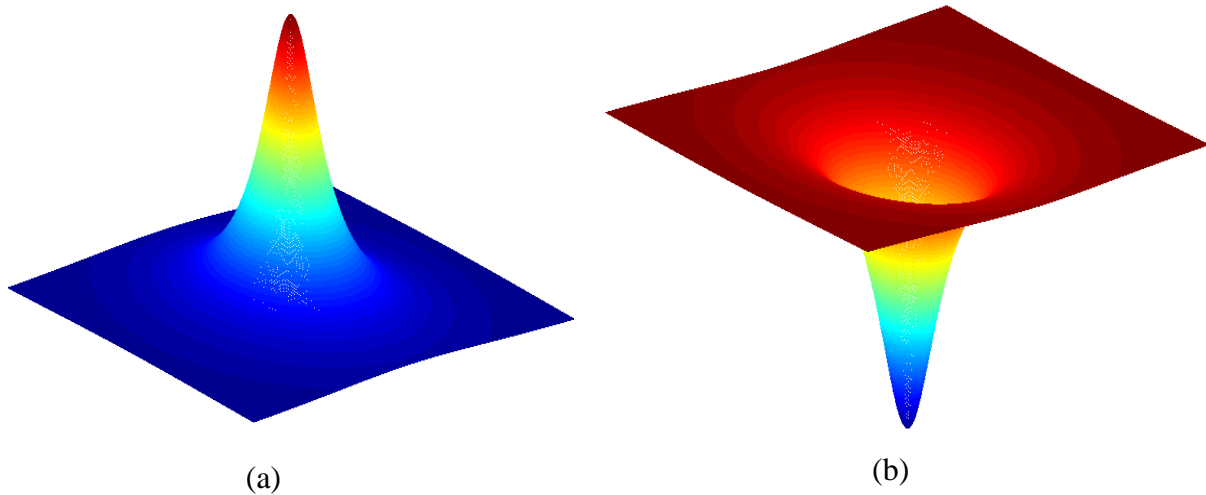
Fig. 3.3. Frequency domain filters: (a) Butterworth Low Pass Filter; and (b) Butterworth High Pass Filter.

The low-pass filter is also known as a smoothing frequency filter. For image processing, a Butterworth Low-Pass Filter (BLPF) was used of order *n* with a cutoff frequency at distance D_o from the center, Eq. 3.9 [Gonzales et al., 2009]:

$$H(u,v) = \frac{1}{1 + [D\,(u,v)/D_o]^{2n}} \,, \tag{3.9}$$

where *H(u,v)* is the filter transform function. A customary function for *D(u,v)* based on a Euclidian distance function was formed from the matrix size of the input image. Each element value is the Euclidian distance to the nearest corner. Converse to the BLPF, the Butterworth High-Pass Filter (BHPF) is used for 'sharpening' images by eliminating the low frequencies and retaining only the high frequency components.

$$H(u,v) = \frac{1}{1 + [D_o/D\,(u,v)]^{2n}} \,. \tag{3.10}$$

Several notes should be made about these filters. First, they do not contain any sharp discontinuities at D_o which eliminates any source of high frequency noise once the phase map is recovered. Also, these filters are applied to the shifted FFT spectrum, where the low frequency components are directly shifted to the origin. The filter transform functions can be directly multiplied by the FFT spectrum, such that the following applies:

$$f(x, y) \star H(x, y) \Leftrightarrow H(u, v)F(u, v) \,, \tag{3.11}$$

where $\star$ is the convolution of two functions. Convolution in the spatial domain is equivalent to the direct matrix multiplication in the frequency domain. The reverse also exists, but we only consider the first phenomenon in Eq. 3.11 because filtering and phase calculation is critically dependent on frequency domain analysis. The $\Leftrightarrow$ symbol represents a Fourier Transform pair [Gonzales et al., 2009]. Appendix A shows the FFT method implemented into MatLab.

In order to isolate the fringe locus function, two of the major types of filters, shown in Fig. 3.4, were experimented, where black represents a value of zero and white a value of one. The edges of the filter are padded to reduce high frequency noise in the final phase map. A balance exists between the size of the filter and quality of the image. The high frequency contained in the FFT improves the 'sharpness' of the wrapped phase map between boundaries. If the filter is too narrow and only isolates directly the shape information, the quality of the image is degraded.

(a)   (b)
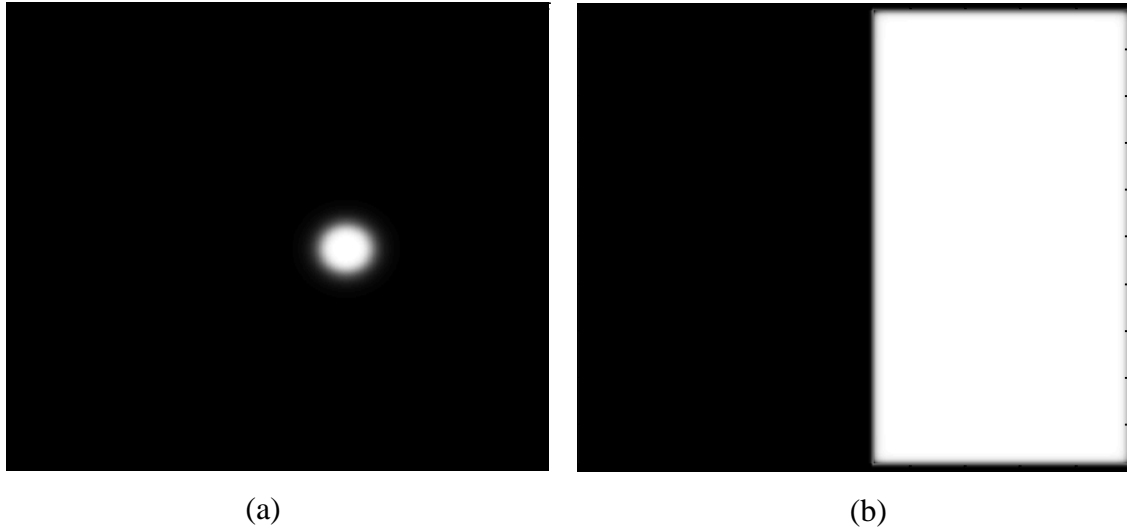
Fig. 3.4. Frequency domain filters applied to images: (a) BLPF; and (b) zero padded square
filter.

Several critical factors affect the ability to recover phase in the frequency domain and
applicability of each filter. First is the relationship between the fringe density and the DC
component. The high amplitude peaks associated with fringes have to be sufficiently separated
from the DC component, Fig. 3.5, for the best filtering and phase results. Otherwise, there is
overlapping of information that cannot be separated using the filters. The extent of the DC is
also directly proportional to the variability in the reflectivity of the object.

Figure 3.5 shows two fringe frequencies and the corresponding shape information
contained in the highest amplitude peaks offset from the center DC component. Figure 3.5a is of
a high density, 4 pixels per fringe. Aliasing can be seen from the high amplitude peaks at higher
frequencies. Figure 3.5b shows lower density fringe, 16 pixels per fringe, with high amplitude
peaks located significantly closer to the DC component.
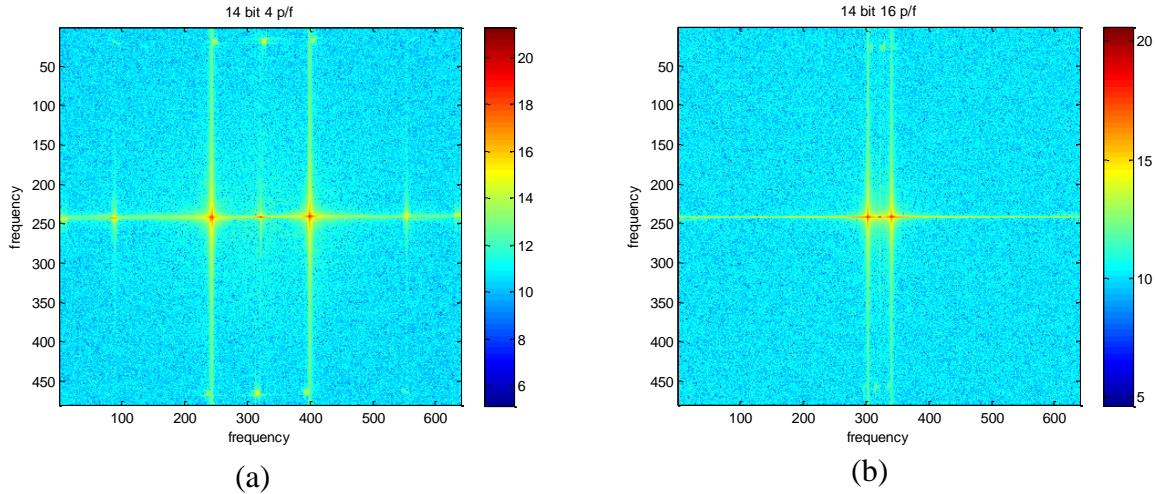
Fig. 3.5. FFT of two different fringe densities across a flat reference surface: (a) high density projection of 4 pixels per fringe; and (b) low density projection at 16 pixels per fringe.

In terms of the filters, when there is other high-frequency noise in the images from aliasing affects as those seen Fig. 3.5a, a BLPF can be used to isolate only the shape information over a narrow area to produce a high quality phase map. Conversely, if there is little aliasing effects then the square filter could be used to incorporate more high frequency components for a sharper result.

3.3. Phase Shifting Method (PSM) of interferometry

In high resolution applications where measurement accuracy is paramount, considerations have to be placed on the method of phase determination. Phase stepping provides an advantage of directly recovering the three unknown variable of brightness, contrast, and phase in the intensity equation by introducing a known shift. By using at least 3 phase stepped images, a phase map can be resolved. Unlike most other phase stepping applications, the developed

30

system is nearly insensitive to phase shifting calibration due to precision control of the projection pattern that is explained in greater details in chapter 4.

One general method for determination of the phase value via phase shifting is the Gaussian least squares approach. The simplified basic intensity equation as a function of *(x,y)* pixel location, the fringe locus function and phase shift is:

$$I(x, y) = a(x, y) + b(x, y) \cos[\Omega(x, y) + \alpha_i] \tag{3.12}$$

Equation 3.12 can be transformed based on the following trigonometric identity using the summations of two variables within a cosine function.

$$\cos(a \pm b) = \cos(a) \cos(b) \mp \sin(a) \sin(b) \tag{3.13}$$

Utilizing the identity of Eq. 3.13, the value of the cosine function in Eq. 3.12 can be revised to form the following results:

$$I(x, y) = a(x, y) + b(x, y) \cos[\Omega(x, y)] \cos(\alpha_i) - b(x, y) \sin[\Omega(x, y)] \sin(\alpha_i) \tag{3.14}$$

For simplification the values of *u* and *v* are set to the following:

$$u(x, y) = b(x, y) \cos[\Omega(x, y)] \tag{3.15}$$

$$v(x, y) = -b(x, y) \sin[\Omega(x, y)] \tag{3.16}$$

Thus, the intensity equation can be simplified by substituting Eqs. 3.15 and 3.16 into Eq. 3.14. The pixel positions *(x,y)* are omitted for clarity:

$$I_n = a + u \cos(\alpha_i) + v \sin(\alpha_i) , \tag{3.17}$$

where n is the image number. Summation of the quadratic errors needs to be minimized by setting the equation to zero and partially differentiating with respect to each of the three variables. The results are a system of three equations with three unknowns that can be summarized by the matrix shown in Eq. 3.18, with the full solution in Appendix B.

$$
\begin{bmatrix}
m & \sum \cos \alpha_i & \sum \sin \alpha_i \\
\sum \cos \alpha_i & \sum \cos^2 \alpha_i & \sum \sin \alpha_i \cos\alpha_i \\
\sum \sin \alpha_i & \sum \sin \alpha_i \cos\alpha_i & \sum \sin^2 \alpha_i
\end{bmatrix}
\begin{bmatrix} a \\ u \\ v \end{bmatrix}
=
\begin{bmatrix}
\sum I_n \\
\sum I_n \cos\alpha_i \\
\sum I_n \sin \alpha_i
\end{bmatrix}.
\tag{3.18}
$$

Noting that the value of the wrapped phase is equal to:

$$
\Omega(x, y) = \arctan \left[\frac{-v(x,y)}{u(x,y)} \right].
\tag{3.19}
$$

The system of equations in Eq. 3.18 can be solved for an arbitrary number of phase stepped images, resulting in the wrapped phase:

$$
\Omega = \frac{-\sum_{i=1}^{m} I_i \sin[\alpha(i-1)]}{\sum_{i=1}^{m} I_i \cos[\alpha(i-1)]},
\tag{3.20}
$$

where α is the value of the phase shift in degrees. With an arbitrary number of shifts, the phase can be calculated. The algorithm is implemented for 4, 8, and 16 phase steps using MatLab and shown in Appendix C.

3.4. The unwrapping problem

Processing and viewing the information at varying speeds requires an unwrapping algorithm. The shape information contained in the phase map of the data is wrapped within an upper and lower boundary of π to $-\pi$ due to the arctangent function in the mathematics of the phase calculations [Ghiglia and Pritt, 1998]. When an upper or lower boundary is achieved, a discontinuity occurs in the form of a 2π phase jump. Figure 3.6 shows an example of 1D signal with a wrapped phase map.
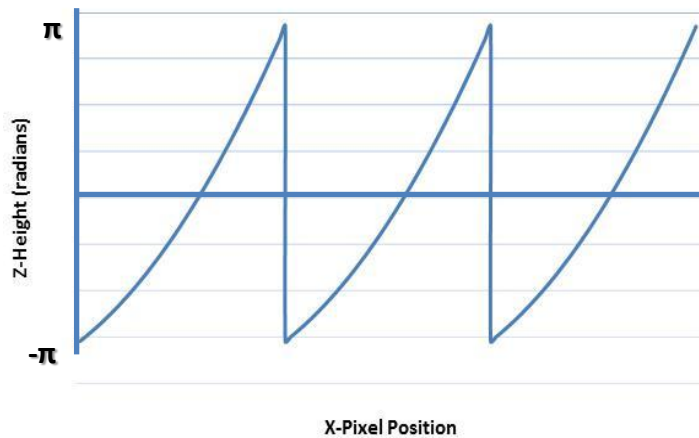
Fig. 3.6. 2π wrapped 1D signal.

The process of unwrapping is the procedure used for resolving the discontinuities by shifting the value of a group of pixels appropriately by a certain value to create a continuous signal. Typically, the fringe order is determined based on whether the discontinuous jump is negative or positive. Figure 3.7 shows the fringe orders graphed as a function of pixel position for the signal in Fig. 3.6.
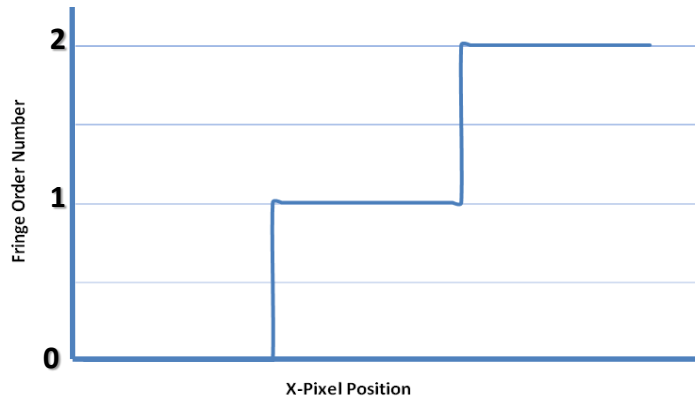
Fig. 3.7. Fringe order numbers corresponding to a shift in the 1D signal
for a continuous phase.

The continuous phase map, known as the unwrapped signal, is graphed in Fig. 3.8. The challenge is reproducing a 2D signal for both high speed and low speed applications, where there may be different signal to noise ratios and resolution requirements.
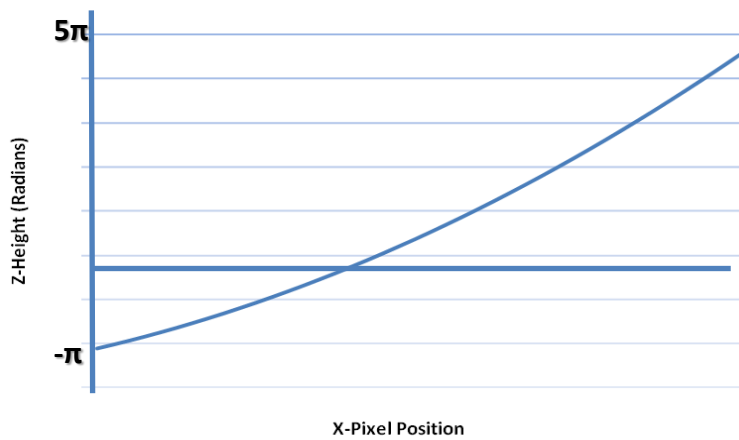
Fig. 3.8. Unwrapped 1D signal.

Understanding of the basic unwrapping problems aids in an understanding of the advantages and disadvantages of other unwrapping algorithms. The key feature is utilizing the appropriate unwrapping algorithms based on the particular requirements of the application.

3.4.1. Spatial unwrapping

High speed applications may require one image or only a few images to reconstruct 3D models. In these applications, spatial unwrapping is required based on a pixel by pixel relation. Post processing on single phase maps can be done using the software developed in the CHSLT called HoloStudio. The algorithm implemented in HoloStudio is based on flood fill procedure that orders regions based on the difference between neighboring pixels [Harrington, 2011]. Figure 3.9 shows 8-direction recursive flood filling based on 'similar' color from a starting position chosen in Fig. 3.9a. All of the squares with the similar attribute programmed into the algorithm are grouped together, Fig. 3.9b [Furlong, 1999].

(a)   (b)
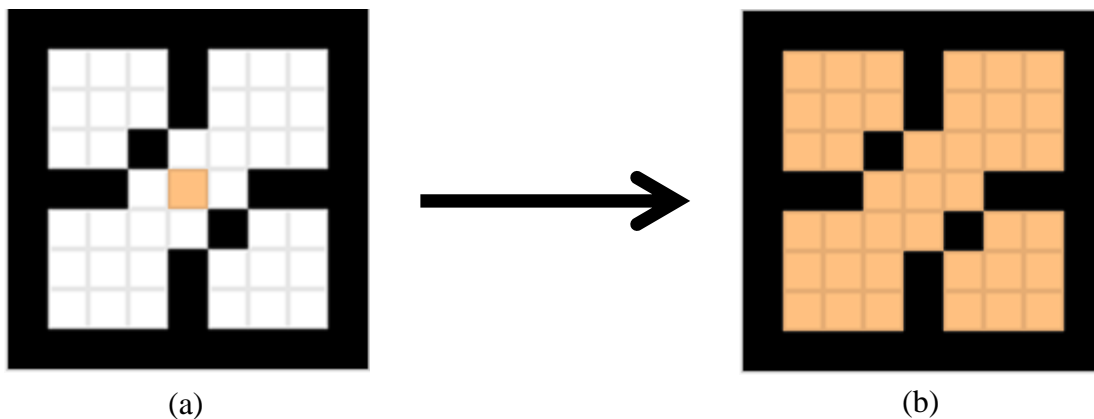
Fig. 3.9. Flood filling algorithm: (a) seed point; and (b) filling of similar grouped pixels [Furlong, 1999].

The algorithm is completed using four sequential steps with four parameters that include the seeding point, group size, threshold, and extent. The algorithm begins by first picking a starting point, or pixel p, which is called the seeding point, similar to the starting point shown in Fig. 3.9a. From this point, the algorithm works outwards by adding neighboring pixels, p', to create one group for all pixels contained by the threshold, t, in radians based on the relation in Eq. 3.20:

$$|p - p'| < t \,. \tag{3.20}$$

Once no more pixels can be added to the group, the algorithm determines if the group is smaller or larger than the minimum group size, g. If the group is smaller than g then the group is discarded and those pixels are marked as null [Harrington et al., 2011]. Starting again at an alternate seeding point, the proceeding steps are repeated until all pixels are assigned to a group or discarded. The difference between pixels of neighboring groups is recorded. The first group with its seeding point, is assigned a level of $N=0$ representing no modification to its values. Next, each group is examined sequentially to find the longest border with a neighbor. That neighbor is assigned a value of N relative to the group that is known. This is done by using the value of the difference between two neighboring groups and using relation in Eq. 3.21:

$$d < -\pi \quad or \quad d > \pi \,. \tag{3.21}$$

If the group is less than π, then the value of the new group is assigned a value N one less than the reference group. The opposite is true for neighboring groups that have a value greater than π, in which case the group is then assigned a value N greater than the reference group. The final step is reassignment of the value of the pixels, Eq. 3.22, by the addition of 2π multiplied by the group value, N:

$$p_{new} = p + 2\pi N \, . \tag{3.22}$$

The developed algorithm for spatial unwrapping runs approximately 10-50 times faster than the previous spatial unwrapping algorithm [Harrington et al., 2011]. Speed is critical in processing of large sets of data, particularly for high speed applications. The effectiveness of the algorithm depends directly on the quality of phase map and the signal to noise ratio in the image.

3.4.2. Temporal phase unwrapping

Spatial unwrapping techniques have drawbacks from discontinuous neighboring pixels on the surface profile that create and propagate errors in the *2π* unwrapping [Huntley and Saldner, 1997]. Thus, temporal unwrapping is another algorithm for resolving discontinuities in the wrapped phase map of an image. Unlike 2D spatial unwrapping, temporal unwrapping is executed in 1D along the time axis, using differing fringe densities. Consequently, pixels are not affected by poor signal to noise ratios in neighboring pixels, reducing errors seen in spatial unwrapping [Kinell, 2000]. This approach is also called a hierarchical technique, by varying the fringe period, *P*, from the largest period to the smallest period, the temporal unwrapping algorithm can be implemented. The broadest fringe density, *K*, should have no *0-2π* discontinuities, Fig. 3.10.
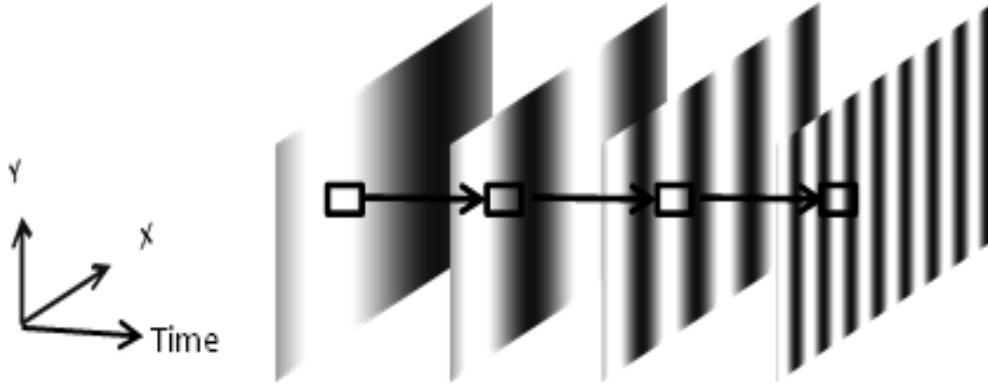
Fig. 3.10. Temporal phase unwrapping is executed along the time axis, with increasing fringe frequency.

The critical parameter in this unwrapping algorithm is the error term, ε, that is determined experimentally between consecutive wrapped images. The standard deviation, σ_Φ, is calculated between consecutive wrapped phase images of the same density that vary only temporally. The difference between the two consecutive sets of wrapped phase maps and the standard deviation of the points is used as an approximation of the error induced by electronic noise and errors in the phase shifter:

$$\varepsilon = 3\sigma_\Phi \, . \tag{3.23}$$

The error estimated is three times the standard deviation, which encompasses 99.73 percent of the data and assumes a small number of corrupt pixels [Burke et al., 2002]. Values of temporal error term, ε, must be lower than 180° for the algorithm to unwrap properly in the time domain. Additionally, this can be directly related to the maximum phase jump increase in the progression sequence for the temporal unwrapping algorithm. The greater number of images

used in the temporal phase unwrapping, the better the quality of the unwrapping. This can be

seen directly in the equation for the temporal unwrapping [Burke et al., 2002].

$$u\Phi_{i+1}(x, y) = \Phi_{i+1}(x, y) + 2\pi N_{i+1} \pm \varepsilon \; , \tag{3.24}$$

where Φ represents the wrapped phase and N is the fringe order number that characterizes phase

jumps with the addition or subtraction of integer values; thus, images are corrected and have no

phase jump discontinuities. An error term, ε, is added due to electrical noise and effects of

uncertainties in the algorithm. A particular resolution can be reached by determining how the

error term propagates through varying numbers of images used to recover the unwrapped phase.

Figure 3.11 shows a theoretical representation of how the error is minimized as more images are

used in the TPU.
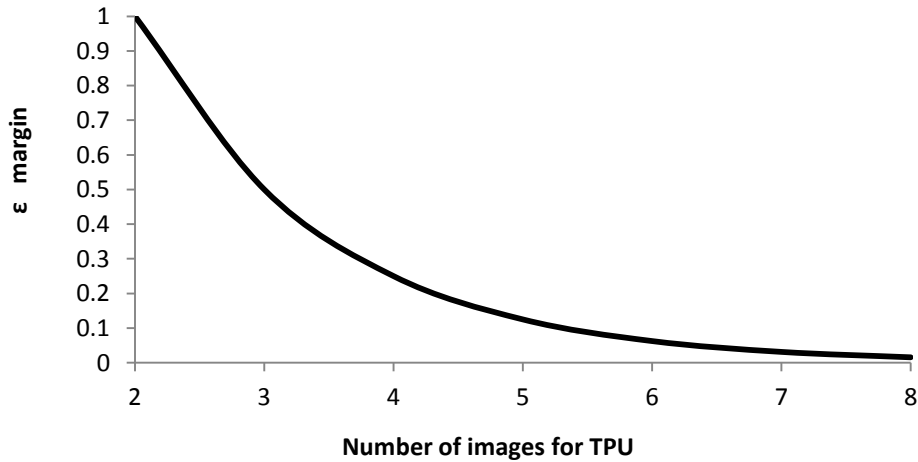
Fig. 3.11. Error propagation as a function of the number of images used in the TPU algorithm.

Although the error approaches zero, the maximum fringe frequency is limited to the

DMD pixel. Thus, higher resolutions can be achieved by using more images in the unwrapping

algorithm in situations where time is not a critical factor. The TPU unwrapping sequence can be determined based on the particular application and its requirements.

Measurements based on varying the temporal unwrapping sequence can be seen in Fig. 3.12 for a flat diffusive surface. A linear sequence was implemented beginning with 512 pixels per fringe and varied linearly to 4 pixels per fringe. It's clear the noise is decreased as more images are used for unwrapping.
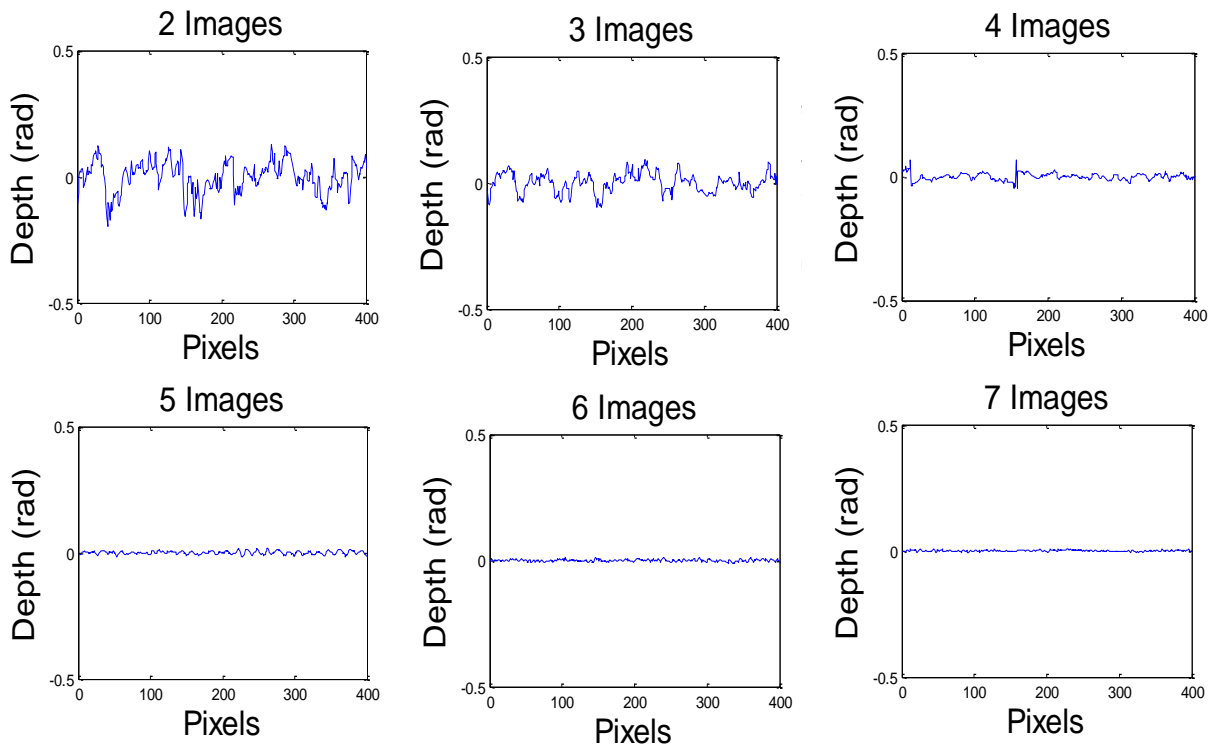
Fig. 3.12. High frequency noise observed in measurements reduced as more images are used for TPU.

A linear progression of increased fringe frequency was tested against an exponential sequence. Figure 3.13 shows the progression sequence as a function and the standard deviation between data points starting from the minimum number of images and increasing.
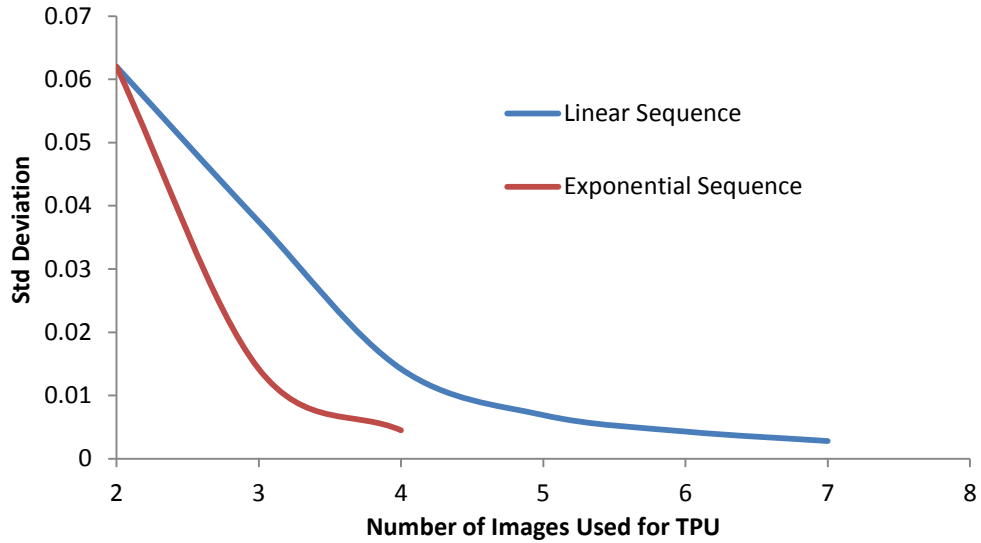
Fig. 3.13. Minimization of errors as function of number of images used in TPU for linear and exponential sequences.

Based on the results, the error is minimized faster when using the exponential sequence, but the major limitation is the number of images used for the unwrapping. The exponential sequence can use a maximum of 4 images corresponding to 512, 256, 64, and 4 pixels per fringe, which is the maximum range of our system.

4. SYSTEM DEVELOPMENT AND ANALYSIS

The Fringe Projection system consists of two major components, a spatial light modulator (SLM) and a digital charged-couple device (CCD) camera. Varying parameters, such as exposure time, fringe density, and field of view, affect the system's resolutions and image quality. Yet, these factors are heavily dependent on the application requirements and object of interest. Based on the first generation prototype, evaluations on the basic effects of varying differing exposures, the quality of the sinusoidal projected patterns, and the effects of varying the CCD and SLM configuration were explored.

4.1. System design

The development and design of the fringe projection system for 3D shape measurements is based on advanced technologies achieved through sophisticated integration of a SLM with a CCD camera. The SLM, packaged by Vialux, contains a digital light processing (DLP®) unit from Texas Instruments called DLP Discovery™ [Texas Instruments, 2010a]. Utilizing the functionality of a field-programmable gate array (FPGA) integrated circuit, the fringe projection system was customized for high speed, sinusoidal fringe projection. The major advantage of this circuit is the ability to directly configure and reconfigure to accommodate a variety of projection patterns based on a particular application.

4.2. MEMS based system improvements

The system uses a Digital Micro-mirror Device (DMD) with a 1080 x 1920 chip resolution that enables sinusoidal fringe projection [Texas Instruments, 2010a]. Based on previous research, this particular system is idealized for the use of gray scale sinusoidal projection because of direct control of each micro mirror. The system has high precision, repeatable achieved by controlling each of the mirrors, or pixels, in the DMD, Fig. 4.1.

(a)   (b)
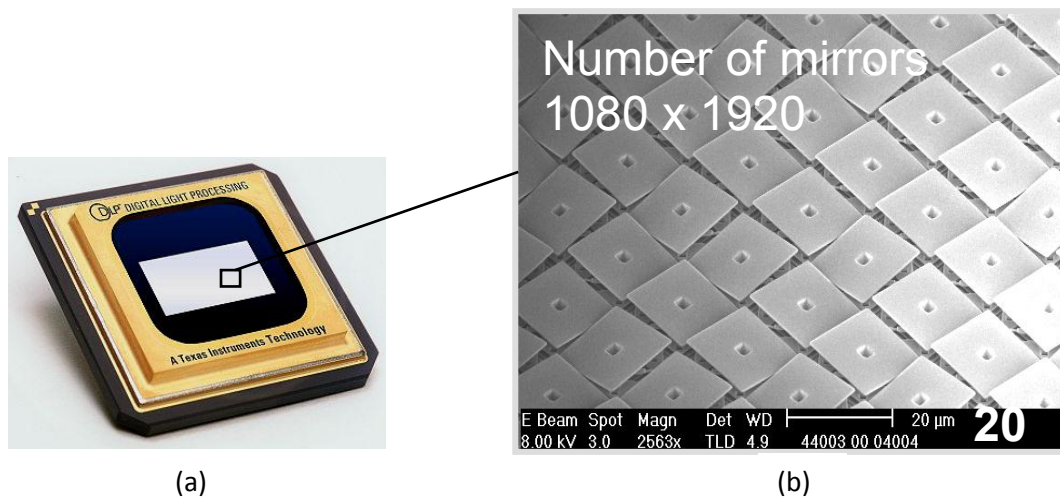
Fig. 4.1. Device developed by Texas Instruments and used in our fringe projection
system: (a) DMD chip; and (b) Enlarged view of micro mirrors enabling
sinusoidal projection [Texas Instruments, 2010b].

The system, created by Texas Instruments and shown in Appendix D, works by direct control of the mirror's position, which can be in one of two states - on or off. The center of each $10x10$ μm^2 device is held by a support post and controlled precisely by a MEMS based component. The mirrors are made to rotate at an angle of ± 10 degrees that depend on the binary state of the cell below the mirror, Fig 4.2. When a particular voltage is applied to the electrode below a mirror, an electro-static force is created that positions the mirror in a particular

43

orientation. The reliability of the method has been greatly improved by advancing manufacturing techniques and life cycle studies of the hinge system [Sontheimer, 2002].
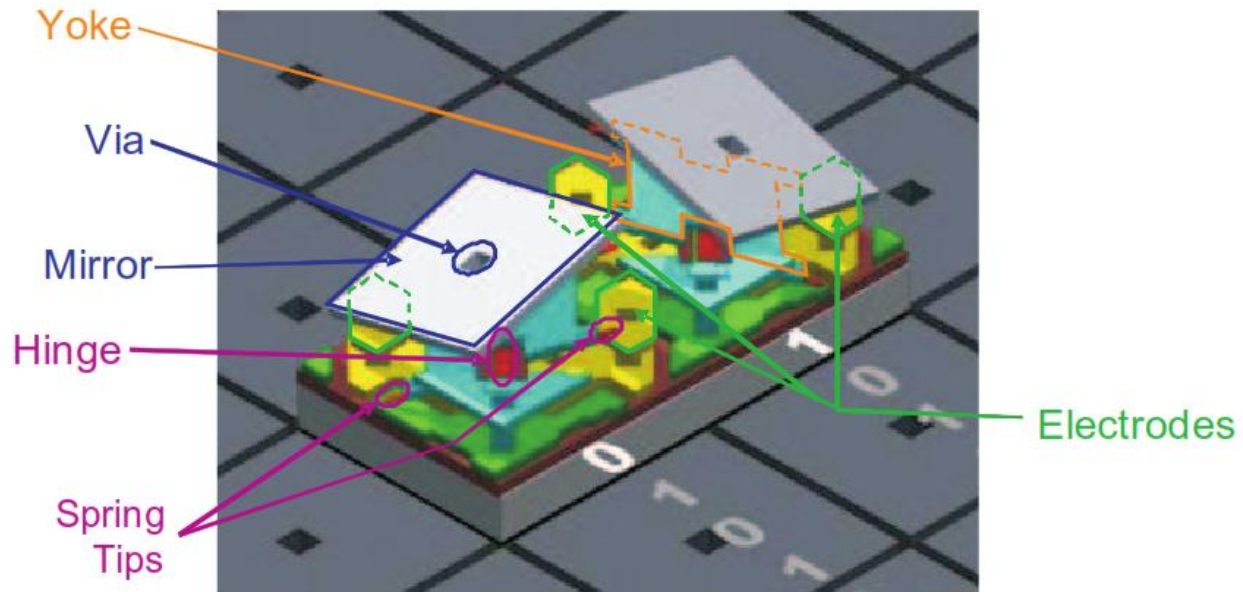
Fig. 4.2. Individual micro mirror component breakdown [Texas Instruments, 2008].

This advanced technology provides a superior tradeoff as compared to other diffraction – based systems in terms of a high contrast ratio, approximately 2000:1, and brightness efficiency [Van Kessel et al., 1998]. The measured power output of the DMD projector was 450 μW, as compared to 97.8 μW recorded from a commercial projector. A ThorLabs Power Meter measured the intensities on 1161 cm^2 (180 in^2) of projection area for an equivalent evaluation. The measurements were recorded at a central projection wavelength of 624 nm.

With precision control of each mirror and camera integration, precision gray scales can be produced. The duty cycle, or amount of time each mirror is on the on/off state is controlled. In the developed system, the camera's exposure time is set to a level corresponding to the

maximum time a mirror can be in the on-state to represent a completely bright fringe. Over this exposure, the camera will integrate, or average, the light intensity of other pixels and produce an equivalent to a gray scale level [Hornbeck, 1997] and [Hofling and Aswendt, 2009]. In basic terms, the total time that each mirror is in the 'on' state varies over a sinusoidal projection. The 14 bit monochromatic CCD Pike-AVT camera integrates the light intensity of each pixel as a function of the camera exposure. This directly produces a gray scale, based on varying intensities in the images.

Current developments enable the projector to change bit-depth rapidly from 5 to 14 bits, and an equivalent range of 32 to 16384 gray levels. An approximation method determines the duty cycle to produce the most appropriate gray scale depending on fringe density. Higher bit-depths result in more accurate sinusoidal representations, but slow the acquisition speeds to a few frames per second (fps). Lower bit-depth projections can maintain speeds, as well as process and display information on the order of 200 fps. Table 4.1 shows the relationship between projected gray scale, the corresponding capture speed, and exposure time.

Table 4.1. Gray scale projection and system speeds.

Bits Gray Scale	System Speed (fps)	Exposure Times (ms)
1	6072	0.016
2	3036	0.033
3	1518	0.066
4	759	0.13
5	379	0.26
6	189	0.52
7	94	1.05
8	47	2.11
9	24	4.22
10	12	8.43
11	6	16.9
12	3	33.7
13	1.5	67.5
14	0.7	135

Although the system can theoretically reach speeds of up to 6,000 frames per second, the major limitation lies in the camera acquisition speed and the required fringe density. For instance, if 512 pixels per fringe are projected at 6 bits then 64 gray scale levels are used to simulate 256 gray levels of the projection. Testing was conducted at 512 pixels per fringe to determine the differences in phase maps as a function of time and the results are shown in Fig. 4.3. The standard deviation in degrees is plotted as a function of the projection bit depth using a flat surface perpendicular to the projector at 2 meters distance.
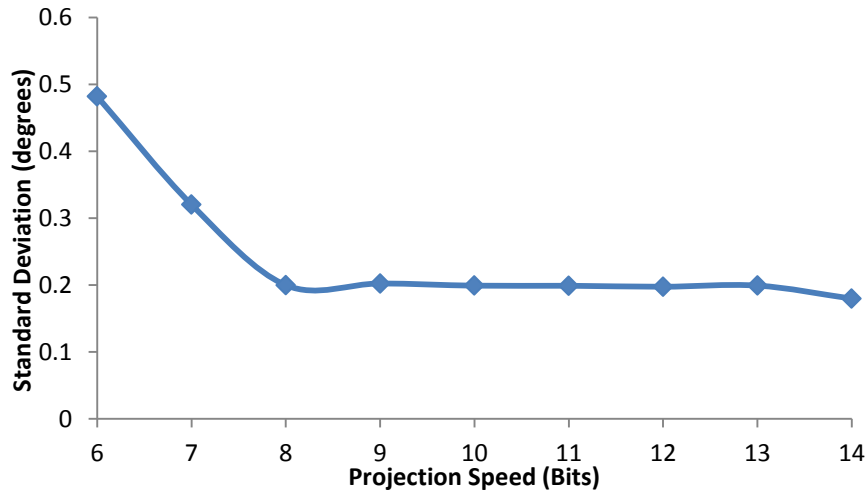
Fig. 4.3. Error effects as a function of the projection speed.

The important feature to notice is that the standard deviation reaches a threshold level when the projected bit depth level is equivalent or greater than the number of gray levels required to construct a sinusoidal projection pattern. At higher fringe densities, the effects of speed are reduced significantly, particularly at 8 or 16 pixels per fringe. Yet, depending on the unwrapping algorithm used to recover the 3D shape, both higher and lower densities may

become an important factor. Additionally, these results are valid amongst a range of distances from the object to the system, thus representing an overall trend and relationship between the system speed and potential 3D reconstruction quality.

4.3. Projector-camera software integration

The relationship between the projector and camera are critical for true representations of the sinusoidal projection. Software developments and improvements were made for integration of the varying bit depths, speeds, and camera triggering for the fringe projection system [Harrington et al., 2011]. The CHSLT developed LaserView software was modified appropriately with a DMD fringe projection module, Fig. 4.4. Options are available to change resolution of the camera and the center, *(x y)*, position of the AOI of the camera if at values other than the highest resolution.
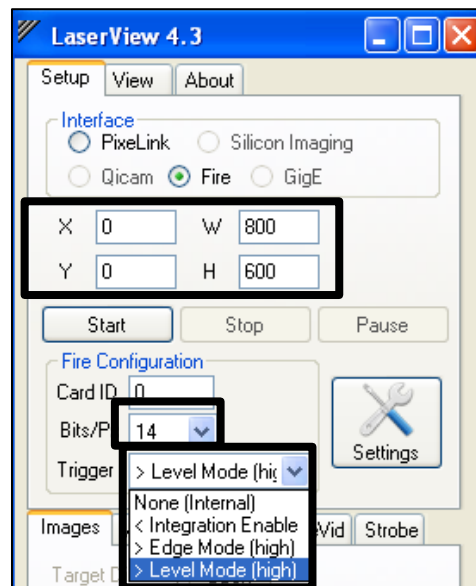
Fig. 4.4. LaserView startup selection user selection mode.

47

The type of camera integration can also be chosen. Internal integration is free run of the camera at video speeds, approximately 60 frames per second. Edge mode-high action is related to the D4100 Explorer software, which is part of the packaged TI DMD device, and only controls camera trigger. During this mode, the exposure time can be adjusted directly and maximum speeds are limited to approximately 25 frames per second by the D4100 Explorer software, although delays can be added to run at slower speeds. Typically, this mode is used for testing of different projection patterns developed without direct programming of the DMD chip. The disadvantage of using the D4100 software is that there is no control of the gray-level. The DMD device can only be in the on/off state without control of the duty cycle of each mirror. When experimentation is conducted at this level a common 'defocusing' technique is used to remove sharp discontinuities from the projected image for improved image quality. Level mode-High action is the programmed, high resolution fringe projection mode used for application testing and system evaluation. Under this mode, exposure time of the camera is set by the chosen bit depth from the user. The gray scale level is achieved by now directly varying the duty cycle of the mirrors and controlling the exposure time of the camera.

In Level mode-High action, the DMD module directly controls the projector via integration with the programmable FPGA board. When the DMD is enabled via the fringe projection module, the user can choose from eight preprogrammed fringe densities that are labeled in terms of pixels per fringe. The highest fringe density reads 4 pixels per fringe and the density increases by a factor of two up to the broadest fringe density of 512 pixels per fringe, Fig. 4.5.
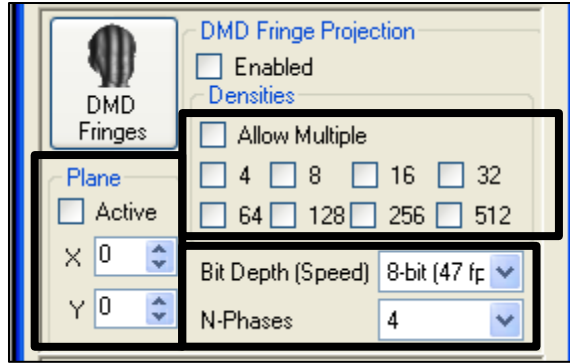
Fig. 4.5. DMD fringe projection module for LaserView.

Another menu allows the user to choose the projection speed in bits that ranges from 5 bits to 14 bits. When the projection speed exceeds the speed of the camera, integration fails and the camera begins to capture at non sequential frames, resulting in phase calculation errors. Depending on the application different number of images can be chosen to calculate the phase map. LaserView has the option to use 4 phase steps, 8 phase steps, or 16 phase steps. It's important to note that for the 8 phase step sequence, the highest fringe density that can be used is 8 pixels per fringe with a 1 pixel phase step. A similar relation exists with the 16 phase step algorithm; the highest projected density is decreased to 16 pixels per fringe. Thus, there is a balance between the image quality and the highest spatial resolution in terms of pixels per fringe. At the same time, using only 4 gray scale levels to model a periodic function could potentially increase discontinuities and reduce system resolutions. In many cases, the minimum fringe density is application dependent. For more information on the LaserView software developed, see [Harrington et al., 2011]

The final feature of the DMD Fringe Projection module is the ability to mathematically remove the plane of the fringes, in the *x* and *y* directions, resulting from the synthetic wavelength

49

produced. This provides users the ability to directly view the fringes from the deformation of the object. It is important to note that as the density is increased by a factor of two, so too is the angle of the plane in the x and y directions. Further optimization includes automatic plane removal based on a fringe counting algorithm to reduce the number of fringes, or groups bounded by 2π phase jumps in an image.

4.4. First generation prototype

The first generation packaging system, Fig. 4.6, was designed and manufactured with the intention of having maximum versatility and robustness for a variety of applications. The enclosure for the projection system was built using stock parts machined on site as well as parts purchased from outside retailers. The main structural components are two aluminum plates (1) and four aluminum rails (2) connecting the two plates. Each plate is made of 3/8" 6061 Aluminum while each rail was purchased from 80/20 Incorporated. Holes were drilled into the aluminum plates to allow for attachment of the four structural rails. Standard fasteners were used to connect the aluminum rails to the plates.
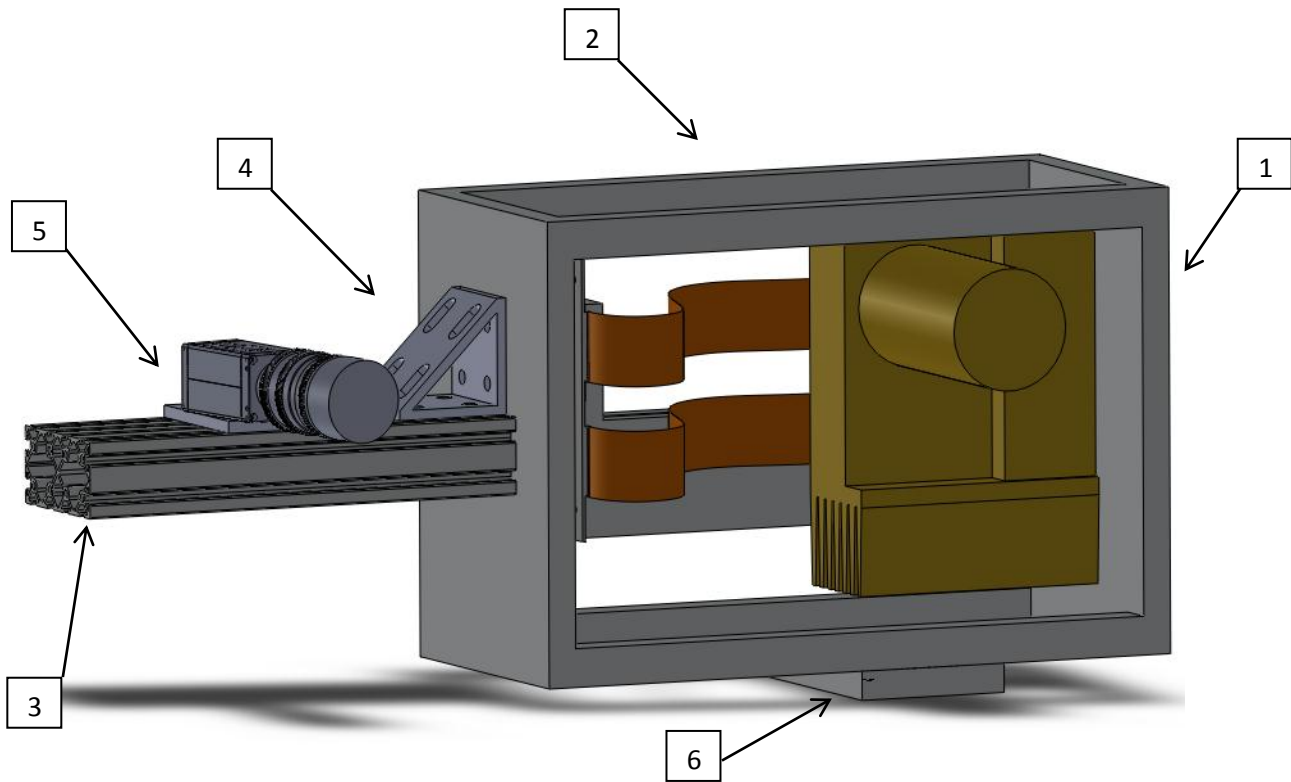
Fig. 4.6. First generation prototype of system: (1) aluminum plates for projector/FPGA board support, (2) rails for structural support, (3) camera mounting arm, (4) camera mounting bracket, (5) camera adaptor plate, and (6) tripod adaptor plate.

The camera mounting arm (3) uses the same rail as the box enclosure. This allows for easy adjustment of the camera while also providing a stable base. The camera arm is attached to aluminum side plates via a mounting bracket (4). Four holes were drilled into one of the side plates. Bolts were then used to secure the mounting bracket to the plate. The arm is attached to the mounting bracket using 1/4"-20 screws that interface with threaded adaptors placed in the mounting arm. The camera is mounted on a plate (5) that allows for rotation parallel to the mounting arm. This is to allow for adjustment when looking at objects at different distances from the projection system.

A tripod and half ball adaptor are used to hold the system steady when it is in use. The tripod selected was a Manfrotto 545B Tripod with a 100 mm half ball adaptor for leveling. The half ball adaptor uses a 3/8"-16 screw to attach to cameras, a standard in the photography industry. In order to allow this system to interface with the ball adaptor a plate (6) was machined to attach to the bottom two structural rails. Four 3/8" diameter holes were drilled into each corner of the plate to allow for 1/4"-20 screws to attach the plate to the rails. A 3/8"-16 tapped hole was then drilled into the center of the plate to allow for attachment to the half ball adaptor. Figure 4.7 shows the realization of the system.

Fig. 4.7. Realization of system setup on a tripod viewing a sculpture for measurement.

4.5. Analysis of system parameters

Once the system was prototyped, an evaluation of the performance had to be conducted, particularly in terms of key parameters that are variable in the system. The first comparison

explored the quality of the sinusoidal fringe projection, which essentially determines the quality of the recovered 3D information. Additionally, the effects of the exposure time and aperture on the image quality were determined. Finally, a direct comparison was made between 4, 8, and 16 phase step methods in experimental conditions. Each of the evaluated parameters has a direct effect on the image quality. Understanding these relationship between parameters are key indicators of appropriate system settings based on the requirements of the application.

4.5.1. Analysis of projected pattern

As explained in the chapter 2, the importance of a sinusoidal projection is critical and directly related to high frequency noise in unwrapped images. Evaluation of the projection by images captured from the camera, under laboratory conditions is critical. As verification, a diffusive, flat surface was setup. For evaluation purposes, a 25 mm telecentric lens with a limited FOV was used to reduce distortions. The projected pattern, at 128 pixels per fringe, and the corresponding cross section in Fig. 4.8 shows the ability to successfully project sinusoidal images from the SLM. A cross-section analysis was conducted on the captured image. The intensity can be seen as a function of the pixel value along the *x-axis*.
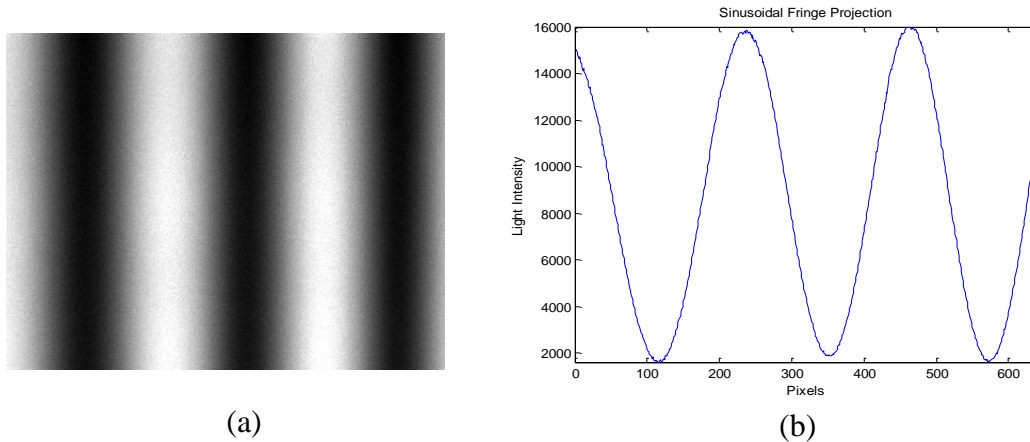
Fig. 4.8. Analysis of projected fringe pattern: (a) capture fringe pattern at 128 pixels per fringe; and (b) corresponding cross section.

For this particular test, there were sufficient gray scale values to accurately resolve the sinusoidal pattern. Yet, it's important to note the direct relation between the number of gray scales used and the fringe density. At high densities, such as 4 pixels per fringe, only 4 gray levels are used to reconstruct the sinusoidal pattern.
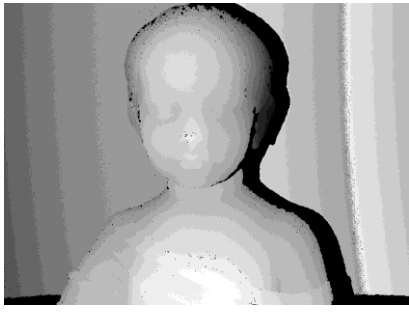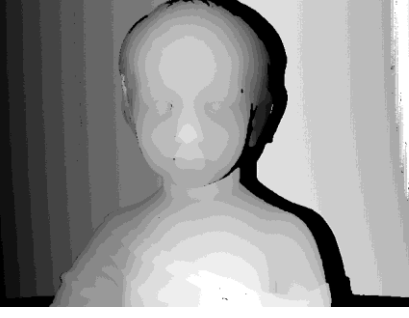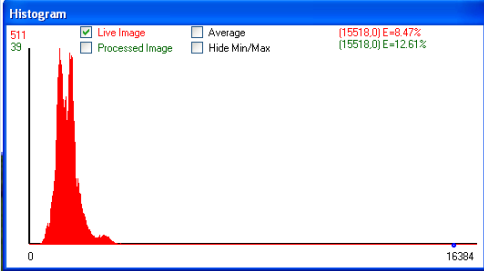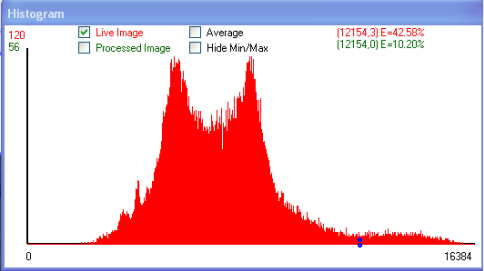
4.5.2. Effects of exposure time and aperture on image quality

The most important quality of each and every measurement is a large dynamic range of gray scales that represents the 3D information of the object shape. One of the ways to improve the dynamic range is by physically increasing the angle of the camera in reference to the object. Another way is to ensure that each measurement has the maximum contrast without saturation. By viewing a histogram of the raw data, the parameter of the exposure should be optimized

based on the largest gray scale range. This ensures the most variation from pixel to pixel and an improved quality of the 3D information.

In order to directly test the effects of the exposure time, information was gathered at two different exposures and F/#. The exposure time represents the amount of time photons of light are reaching the sensor of the camera and the F/# is representing the diameter of the aperture of the lens. As the F/# increases, the amount of photons hitting the sensor of the camera decreases. In Table 4.2, the wrapped phases and spatially unwrapped phases are shown. Additionally, the corresponding histograms with the dynamic range of the gray scale are shown. The images were captured at 14 bits, corresponding to 16,384 gray scale levels, which is the *x-axis* of the displayed histograms.

Table 4.2. Comparison of exposure time and F/# on image quality.

	Measurement at F/#: 1.8 and Exposure Time: 0.995 ms	Measurement at F/#: 2.8 and Exposure Time: 8.155 ms
Raw Images		
Unwrapped Phase		
Histogram of Raw Images		

An analysis was conducted on each set of unwrapped images to quantify which set had the better image quality. One indirect method was to look at the cross section of the data across one line of the sculpture. The high frequency noise in the cross section would be directly visible in the power spectrum in the frequency domain. As a result, a 1D FFT of each cross section was taken and compared. Thus, larger signal amplitudes mean nosier images. A direct comparison is

shown in Fig. 4.9 in terms of decibels. Again, the logarithmic scale was chosen for viewing purposes, which is the reason for the portions of power spectrum residing below the zero line.
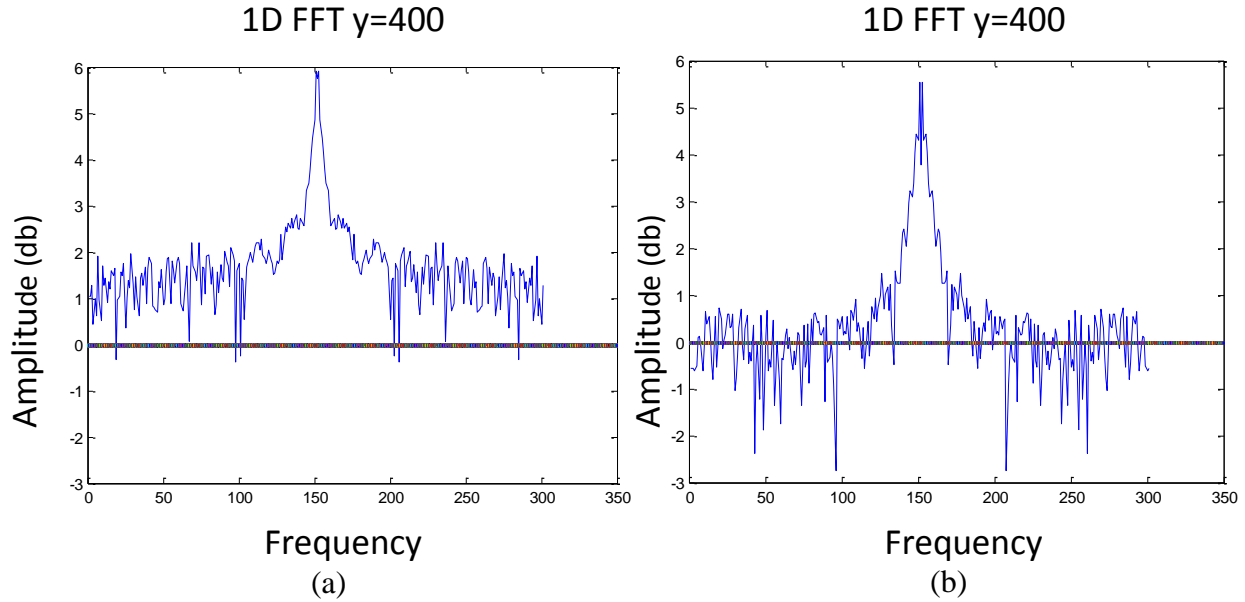
Fig. 4.9. 1D FFT: (a) poor dynamic range with narrow histogram; and (b) large dynamic range.

Based on the results of the preceding analysis, evaluations on the dynamic range via the histogram will be conducted prior to making measurements as part of a 'testing procedure'. The histogram was added as measurement model in the LaserView software along with cross-section analysis for convenience. Clearly, improved dynamic range and better contrast reduced high frequency components in the unwrapped image.

4.5.3. Comparison of phase calculation method on image quality

Depending on the requirements of the application, speed has a potential to be an important factor. Therefore, in all cases, large numbers of phase steps may not be used to calculate the wrapped phase. In any case, it's necessary to understand the relationship between the high frequency noise in images and the number of phase steps used. Theoretically, the more images used, the greater reduction in the random noise, but experimentation is needed to explore the magnitude of this effect. Once again, a diffusive, flat surface was setup for measurement. The camera and aperture setting were kept constant. The wrapped phase map is shown in Fig. 4.10 and was calculated via MatLab.
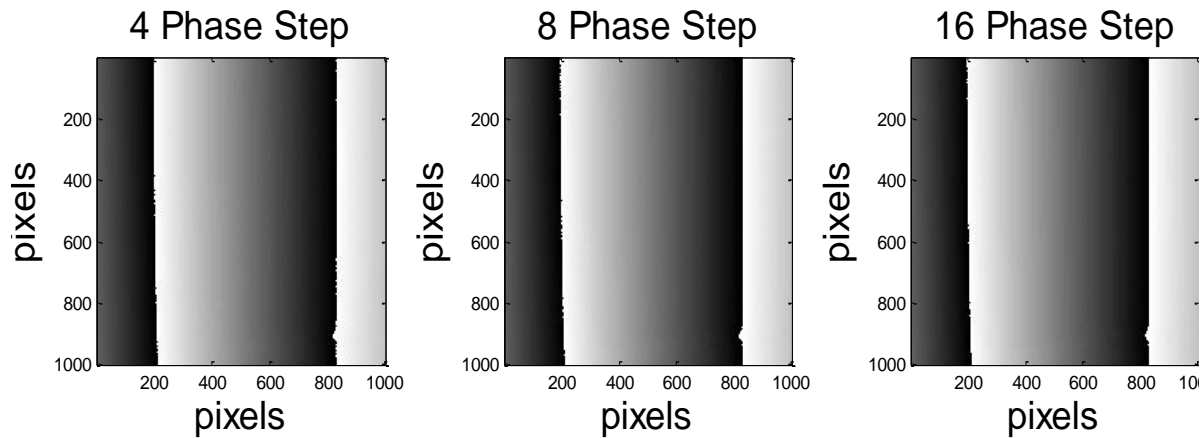
Fig. 4.10. Wrapped phase maps for 4, 8 and 16 phase steps.

A cross section of the wrapped phase is shown in Fig. 4.11 for all values across the 200th row. For each case, the arctangent function modulates the data between vales of $-\pi$ and π.
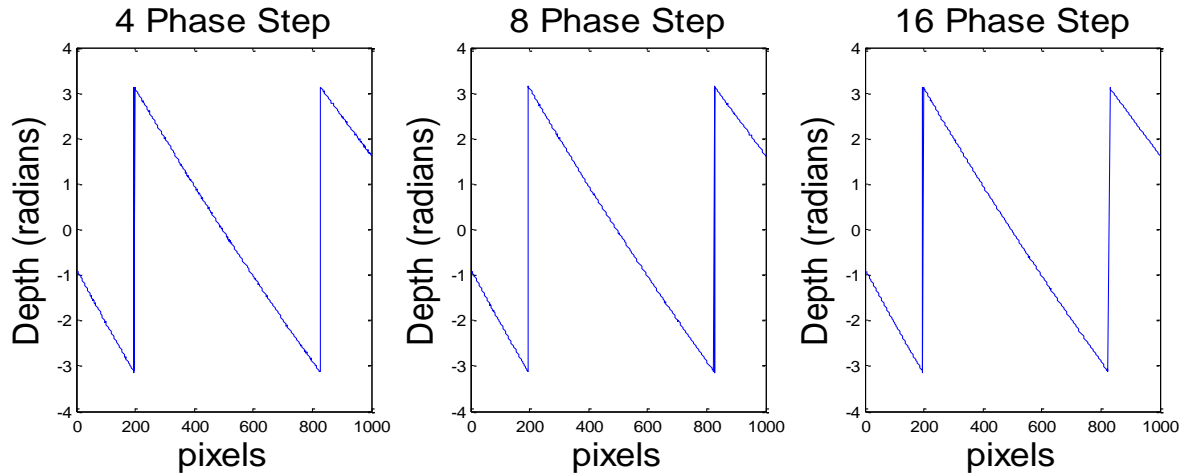
Fig. 4.11. Cross section of wrapped phase map from Fig. 4.10.

A mathematical plane was directly subtracted from the data and a second order polynomial was fit to the line. The actual data and the fit line were directly subtracted. The standard deviation was calculated in each case and plotted, Fig. 4.12.
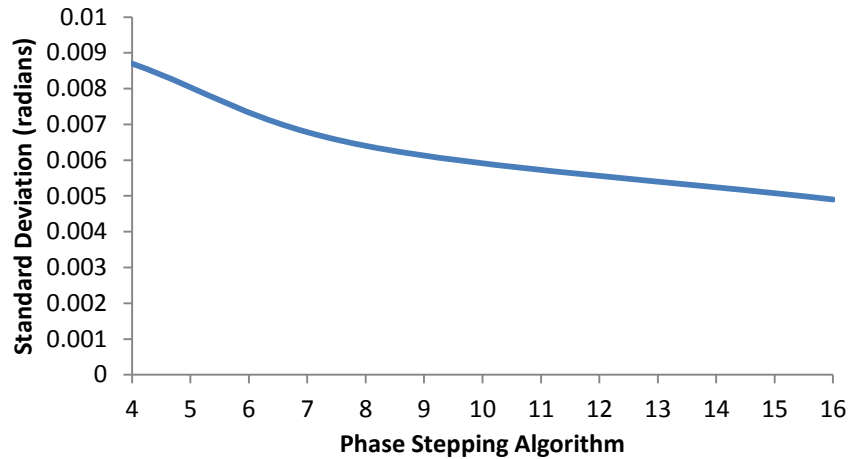
Fig. 4.12. Error effects as a function of phase stepping algorithm.

Based on the results, the standard deviation is significantly reduced as a function of the numbers of images used to calculate the phase. Therefore, just as predicted in the theoretical case, the electronic noise is reduced as a function of the number of phase steps.

5. SYSTEM CALIBRATION

Calibration of the system is important for the accuracy of the 3D shape measurement system. One particular effect of the configuration is the changing fringe frequency that occurs in the viewing 'eye' of the camera. This can be considered the effect of perspective on the system and its measurements.

5.1. Theoretical calibration effects

Removal of perspective is critical, particularly in high speed applications with the use of the Fourier Transform Method of phase calculations. This is due to the nature of the phase calculation method. When isolating the high frequencies associated with the fringe density, non-calibrated images have a varying density across the length of an image. When analyzing in the frequency domain, a form of smearing of the high frequencies occurs rather than a very dense, image with high frequencies associated as seen in Fig. 5.1.
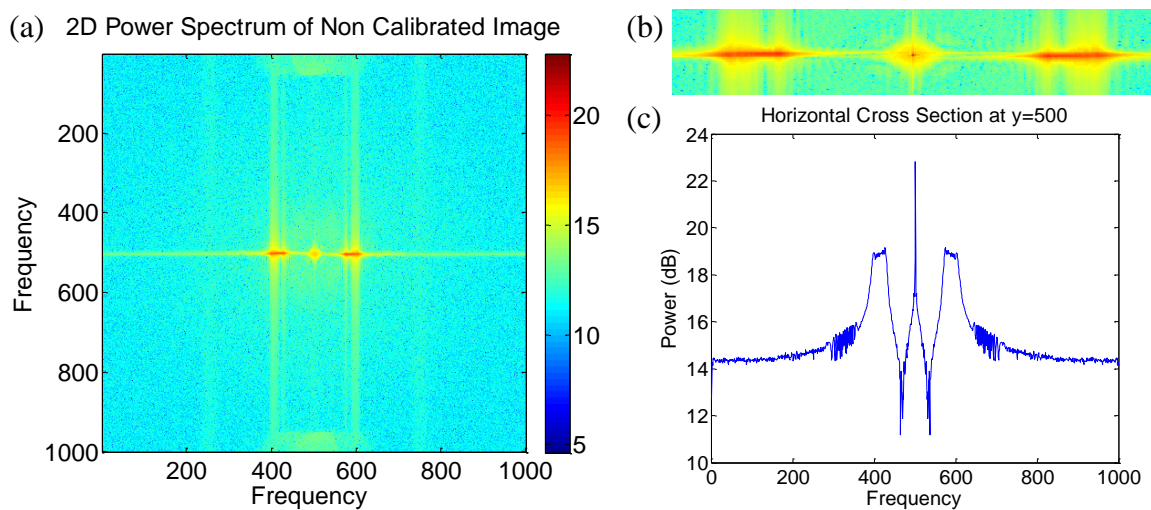
Fig. 5.1. FFT of a non calibrated image (a) Original non calibrated power spectrum; (b) Skewed shape information; and (c) Cross section showing several high amplitude peaks.

Taking a closer look at 3D reconstruction via triangulation, Fig. 5.2, the local spatial frequency of the fringes along the *x-axis* remains constant due to the SLM's perpendicular configuration from the reference plane.
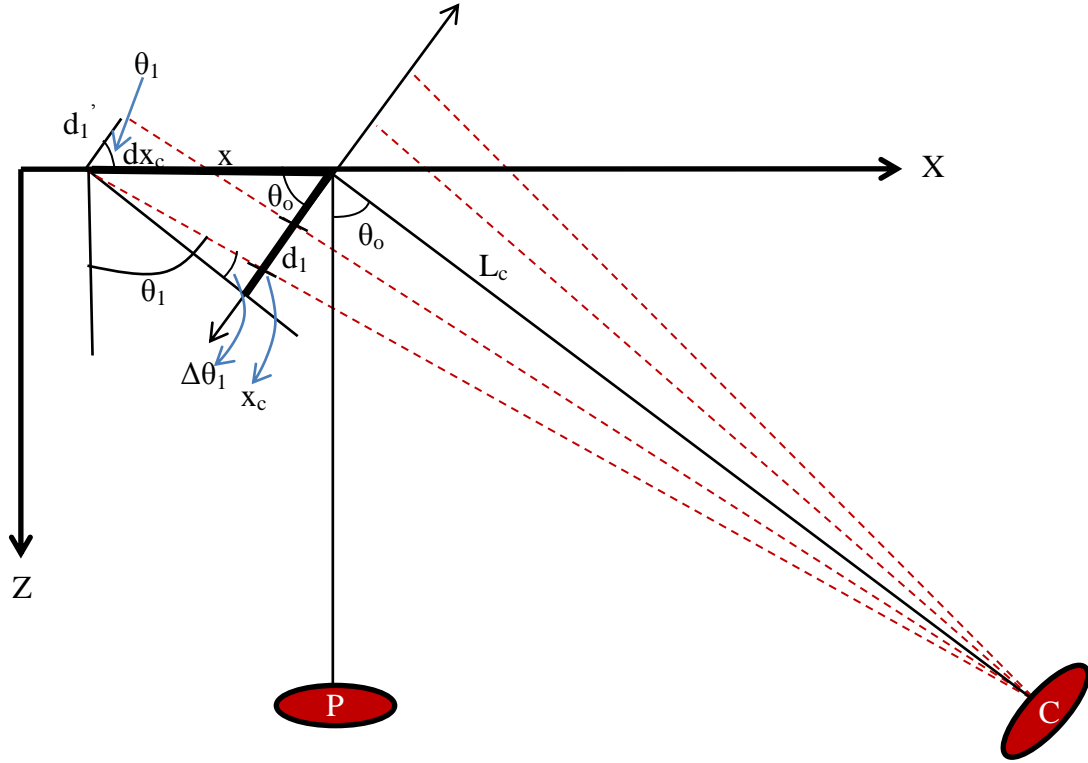
Fig. 5.2. Schematic showing the effects of perspective on the fringe pattern frequency.

Images captured by the camera separated by an angle will have varying fringe frequencies due to perspective effects of the camera. The spatial frequency is characterized by the distance, *d*, between two fringe maximas and is described by Eq. 5.1, where the *p* represents the fringe period and *m* represents the magnification factor [Spagnolo et al., 2000]:

$$d = mp .$$ (5.1)

Magnification values vary based on the distance of the object, pixel size of the camera, and optical zoom from the lens. The spatial frequency captured varies along the surface of the

plane perpendicular to the projector, directly resulting from the angle of the camera. From basic geometry, the corresponding period viewed by the camera is can be calculated using Eq. 5.2 from Fig. 5.2:

$$d_{X_c} = \frac{d_1}{\cos(\theta_1)} \ .$$

(5.2)

The value of the θ_1 needs to be determined. The equations can be simplified by looking at the right triangle from the center to the calculated fringe period:

$$\theta_1 = \theta_o + \Delta\theta_o = \theta_o + \frac{x\cos(\theta_o)}{L_c} \ .$$

(5.3)

Similarly, the following holds true based on similar triangles:

$$\frac{d_1}{L_c} = \frac{d_1{'}}{L_c + x\sin(\theta_o)} \ ,$$

(5.4)

$$d_1' = d_1\left(1 + \frac{x}{L_c}\sin(\theta_o)\right).$$

(5.5)

Substitution of Eqs. 5.4 and 5.5 into Eq. 5.2 result in:

$$d_{Xc} = d_1\left(\frac{1 + \left(\frac{x}{L_c}\right)\sin(\theta_o)}{\cos[\theta_o + \frac{x\cos(\theta_o)}{L_c}]}\right) \ .$$

(5.6)

The trigonometric identity described by Eq. 3.13 can be applied to the cosine function in the denominator of Eq. 5.6 to yield:

$$d_{Xc} = d_1 \left(\frac{1 + \left(\frac{x}{L_c}\right)\sin(\theta_o)}{\cos(\theta_o)\cos[\frac{x\cos(\theta_o)}{L_c}] - \sin(\theta_o)\sin[\frac{x\cos(\theta_o)}{L_c}]} \right). \tag{5.7}$$

The camera distance is large as compared with the illumination area of $x\cos(\theta_o)$ which means that the cosine value approaches one. Also, the sine function can be approximated to equal the ratio of $x\cos(\theta_o)$ over the distance from the camera, L_c. Thus, Eq. 5.7 can be simplified to:

$$d_{Xc} = d_1 \left(\frac{1 + \left(\frac{x}{L_c}\right)\sin(\theta_o)}{\cos(\theta_o)\left(1 - \left(\frac{x}{L_c}\right)\sin(\theta_o)\right)} \right). \tag{5.8}$$

Knowing that the frequency of the fringes is equal to the inverse of the period, d_{Xc}, the local spatial frequency along the x-axis can be determined. Again, assuming that the value of $x\cos(\theta_o)$ and $x\sin(\theta_o)$ is much larger than the length, L_c, a simplified solution for the local spatial frequency is shown [Spagnolo et al., 2000]:

$$T(x) = \frac{\cos(\theta_o)}{d_1}\left(1 - \frac{2x}{L_c}\sin(\theta_o)\right). \tag{5.9}$$

As part of the calibration procedure, it's important to have an understanding of how an image is transformed from the real world coordinate system to the coordinate system of the camera. In order to demonstrate this, a pinhole model was researched.

5.2. Pinhole Model

Calibration is a complex task that is critical to accurate 3D reconstruction and has been studied extensively [Yamauchi et al., 2008]. The developed calibration procedure for the fringe projection system is based on the pinhole model, Fig. 5.3, that defines both intrinsic and extrinsic parameters [Yamauchi et al., 2008]. The intrinsic, or internal, parameters include the focal length, lens distortions, pixel skew factor, and pixel size. The extrinsic parameters include the position or orientation of the camera. The basic pinhole model defines a geometric relationship between a 3D point and its 2D corresponding projection based on the center optical axis of the camera [Morvan et al., 2007].
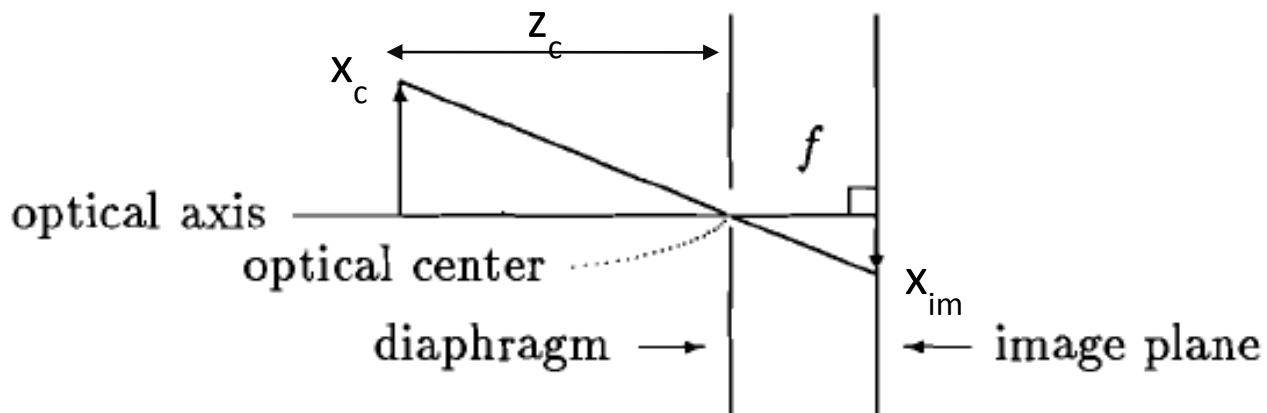
Fig. 5.3 Pinhole model showing the image plane and optical axis

From basic geometry, the values of *x* and *y* on the plane of the image can be scaled appropriately as follows:

$$x_{im} = f \frac{x_c}{z_c},$$

(5.10)

$$y_{im} = f \frac{y_c}{z_c},$$

(5.11)

where *x-value* of the image is related to the focal length, the distance of the sensor to the focal point and its corresponding height dimension. A similar relation can be established for the scaled *y-value*. The important factor is the conversion from 3D points in space to the corresponding 2D points. Figure 5.4 shows a point *p* on the surface of an object with a coordinates in the world coordinate system, (x_w, y_w, z_w), and in the camera lens coordinate system, (x_c, y_c, z_c).
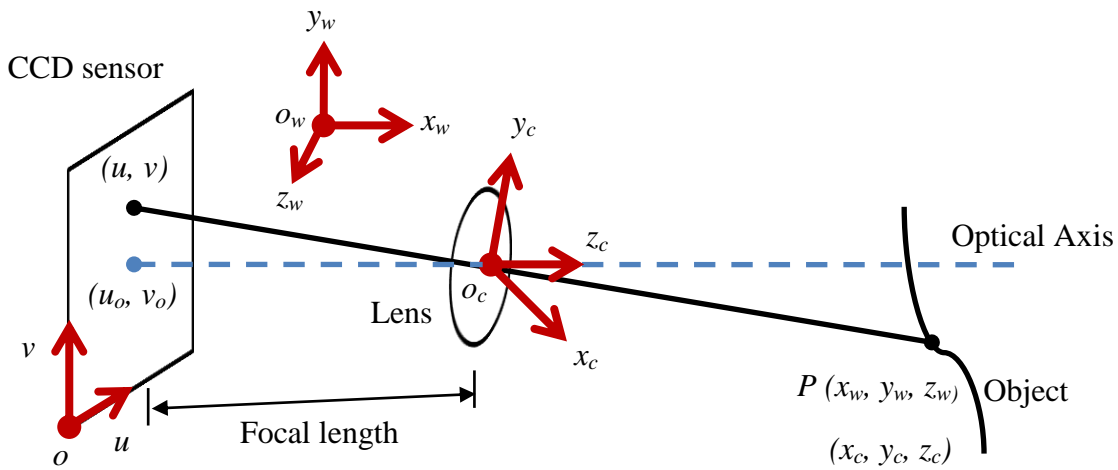
Fig. 5.4 System model schematic

The coordinate of the point of the object as projected on the sensor of the CCD is represented by point located *(u,v)*. Thus, the relationship between the location of the point on the object and on the sensor can be modeled mathematically in Eq. 5.12:

$$sI = A[R, t]X_w ,\tag{5.12}$$

where *s* is the scaling factor, *I* is the homogenous coordinate of the projected imaged on the sensor such that $I=(u,v,1)^T$ in the conversion from Cartesian to homogenous coordinates, and X_w

is the homogenous coordinate in the world coordinate system such that $X_w=(x_w, y_w, z_w, 1)^T$ [Zhang and Huang, 2006]. Homogenous coordinates are critical in simplification by adding another term in the coordinate system. Essentially, this allows the use of 3D calibration with the use of a 2D sensor. Matrix *[R, t]* compensates for the extrinsic parameters. The intrinsic matrix A is defined as:

$$A = \begin{bmatrix} \alpha & \gamma & u_o \\ 0 & \beta & v_o \\ 0 & 0 & 1 \end{bmatrix}.$$
(5.13)

Point (u_o, v_o) is the center point of the camera along its optical axis. The variables α and β are focal lengths along the *u* and *v* axis in pixels as described by a linear model. Lastly, γ is the skew coefficient. Determination of the *[R, t]* matrix for the extrinsic parameters and the matrix *A* for the intrinsic parameters encompasses a complete calibration procedure.

5.3. Calibration Procedure

A calibration procedure was implemented with the use of MatLab. The method was a combined calibration method that included intrinsic and extrinsic parameters from the camera as well as distortions from the projector optics. The method was to set up the system parallel to a diffusive flat surface. The DMD device was programmed to project box patterns with three varying densities, 8 square pixels per box, 16 square pixels per box, and 32 square pixels per box. Depending on the FOV of the camera based on the lens and the distance of the object from the projector, the appropriate density would be used to gather between 15 and 128 control points

from the box image. An automated calibration procedure takes an image, Fig. 5.5, and inputs it into a developed program for outputting the calibration matrix.
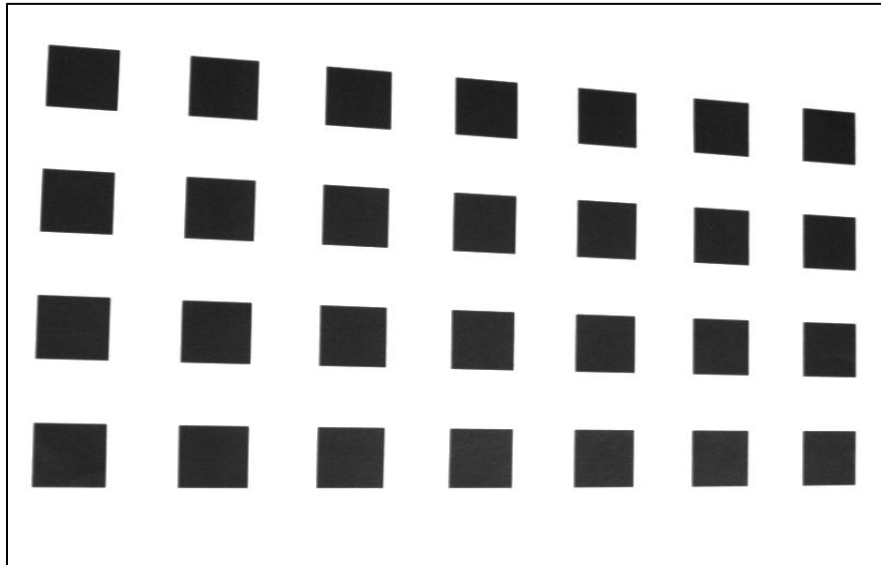
Fig. 5.5. Calibration target image captured by the CCD camera.

The algorithm has been optimized for finding the center location of each of the square based on a type of segmentation procedure. Figure 5.6 shows an example procedure with the centers of the squares selected.
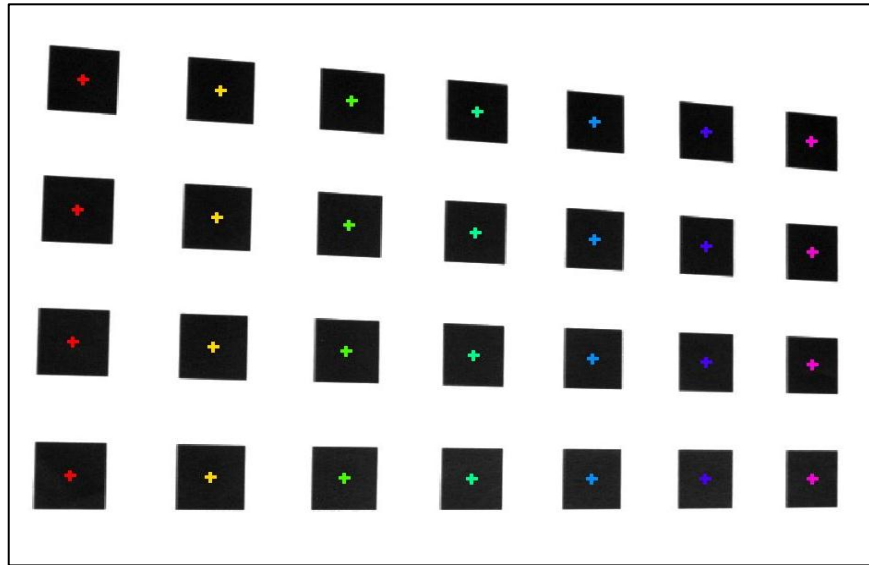
Fig. 5.6. Segmentation Procedure that identifies the center of each box.

A user-defined number of control points are inputted into the program where centers are chosen randomly throughout the image. A base image is then uploaded, of which size is automatically cropped to fit the same size based on the numbers of squares. The same sequence of corresponding square centers is selected in the base image, Fig 5.7.
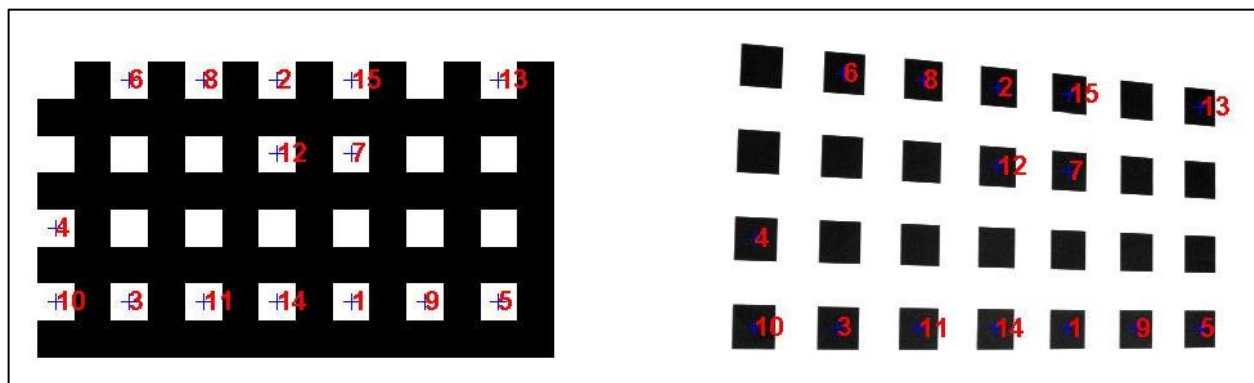
Fig. 5.7. Control point selection based on idealized target point location.

In essence, the program knows where the squares are located in the base image and how the values are distorted in the captured image. A transformation algorithm is built in that corrects distortions and outputs the calibration matrix that can be applied to any set of images taken at this particular configuration. The results of the calibration are shown in Fig. 5.8.
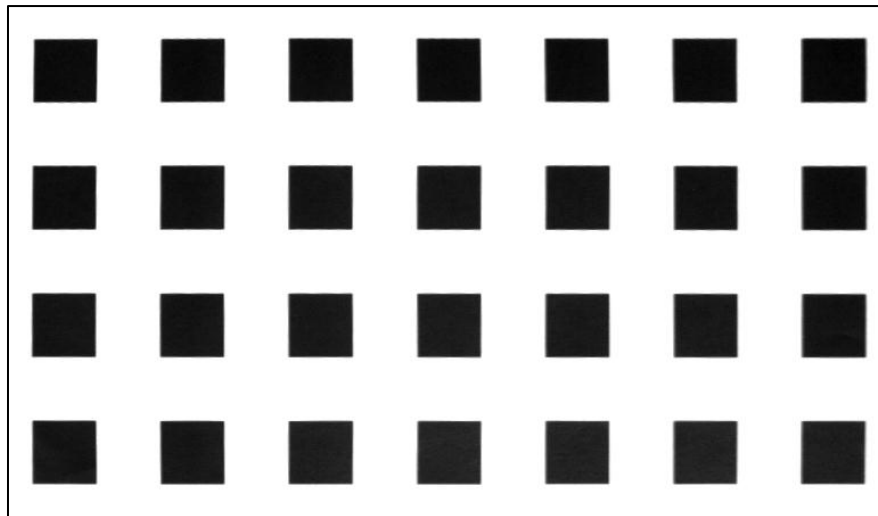
Fig. 5.8. Calibrated image from Fig. 5.6.

In this particular calibration example, the effects of the transformation matrix are difficult to see visual. Yet, for more practical applications, some information is lost after image calibration. This phenomenon is due to the correction of the x and y pixels. As the image is shifted appropriately in space, there are inherently areas of no data so the image is slightly cropped after calibration.

As validation of the calibration procedure, an algorithm was developed that binarizes the image based on thresh holding. The top corner of each of each step was selected automatically, Fig. 5.9. The x pixel position of these points were stored.
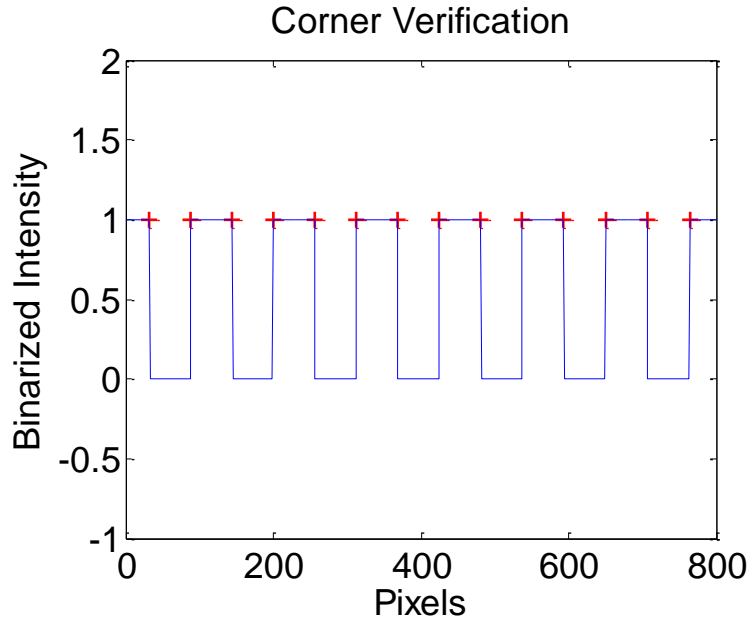
Fig. 5.9. Calibration verification via detection of corner location on
binary image.

The image before calibration had large perspective effects that distorted the distances between squares. Yet, in the calibrated images, this effect would be compensated for and the distances between squares should be the same value. Consequently, the pixel value was plotted at each location and the results are shown in Fig. 5.10.
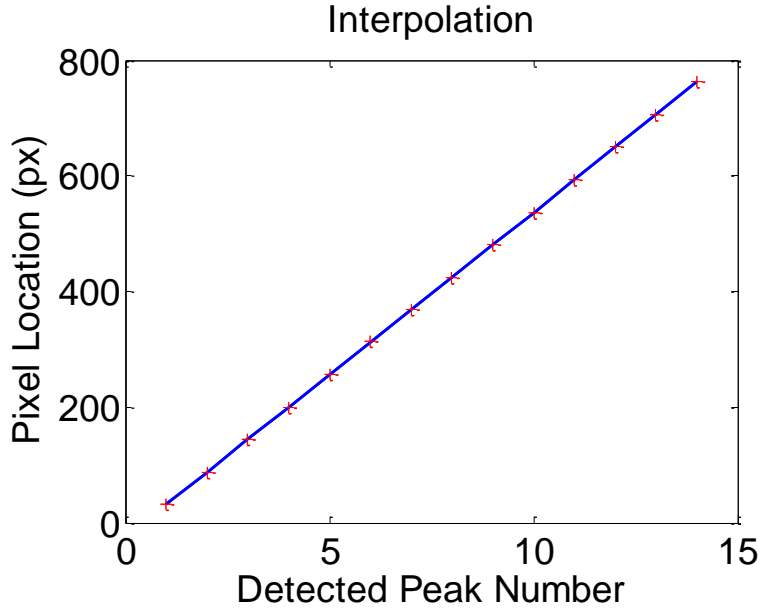
Fig. 5.10. Peak points plotted and best line fit showing period of box
pattern was calibrated.

Results validate the calibration procedure. The standard deviation of the best fit line is

0.75107 pixels. Calibration using this method is advantageous for several reasons. First, the

method is effective in removing aberrations from the camera's intrinsic and extrinsic parameters

as well as from the distortion of the projector's optical system. Second, this technique can be

used directly to calculate the zoom factor for each pixel. By knowing how the pixels size relates

to real coordinates, the *z-axis* can be scaled in the unwrapped images. Inversely, knowing the

scaled size of a projected pattern means that the distance from the object to the projector can be

calculated using basic geometry, Fig 5.11, and knowing the focal length of the project of 1.5

centimeters.
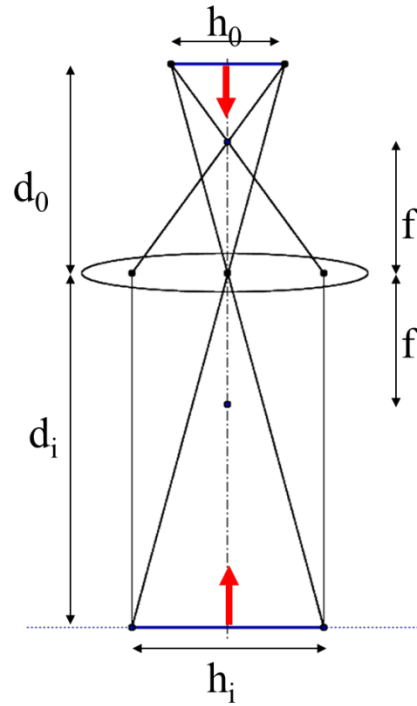
Fig. 5.11. Method for calculating distance of projector to object based on geometry.

The focal distance of the projection optics is defined by f. Also, the size of the sensor is h_o, the FOV is h_i, and the distance of the projector to the object is d_i. In summary, the calibration technique implemented is versatile to a number of applications. The system can be calibrated based on the system requirements easily and precisely. This is the advantage to the developed system. The versatility lies in not just the mobility of the measurement device, but also in all the methods incorporated into its developments.

6. DEMONSTRATION OF SYSTEM CAPABILITIES

The capability to measure 3D information is only as useful as the precision and accuracy of the system. Demonstrating these features validates the applicability prior to making measurements in field conditions. Additionally, based on the results, the resolution, in *(x, y, z)*, can be determined.

6.1. Measurement accuracy and resolution

Using the developed system in a single fixed position and the techniques outlined in chapter 5, the accuracy of the system was evaluated. The relative parameters of the system were measured mathematically, via calibration and imaging of a measuring device, Fig. 6.1a. The number of pixels over a 30.5 cm (12.0 inch) length was evaluated to give the size of the scaled pixel, approximately 0.4031 mm per pixel (0.01587 inches per pixel). Knowing this value, the size of the square in the calibration matrix was determined. Thus, the distance L of approximately 114.3 cm (45.0 inches) from the object to the projector was determined by knowing the corresponding number of pixels per square projected from the system, Fig. 6.1b. The same is valid for the wavelength in inches at the focus plane, knowing the 32 pixels per fringe, the wavelength, λ, is 2.52 cm per fringe (0.99 inches per fringe). The fixed distance from the projector to camera, D, was set at 61.0 cm (24.0 inches).

<center>(a)   (b)</center>
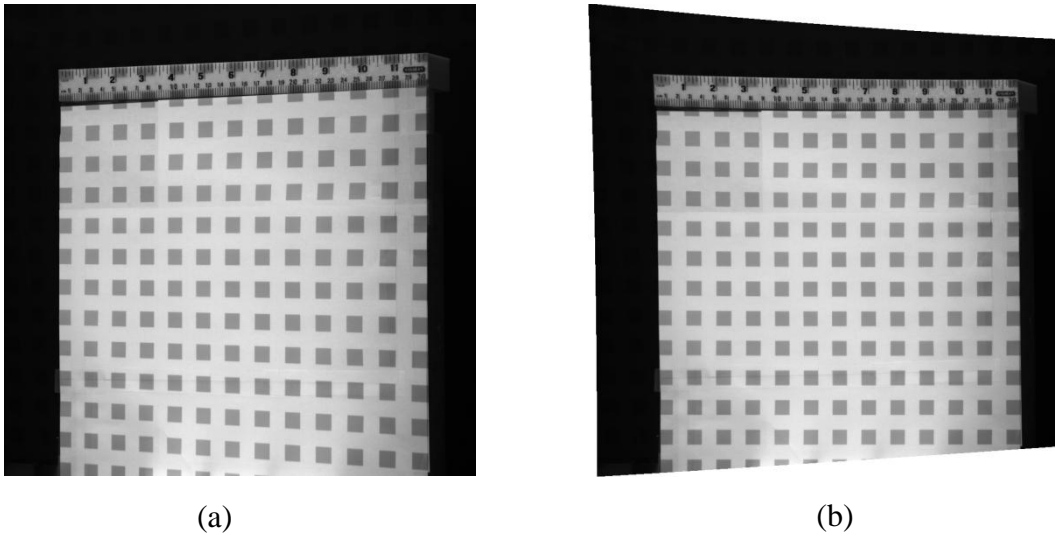
Fig. 6.1. Calibration and demonstration of system accuracy: (a) Original image for calibration; and (b) calibrated image.

Based on these parameters, the object was replaced with a calibrated cylinder that had an outer diameter of 25.4 cm (10.0 inches), shown in Fig. 6.2. Using 32 pixels per fringe setting and the four phase step algorithm, the appropriate scaling was determined for 3D reconstruction.
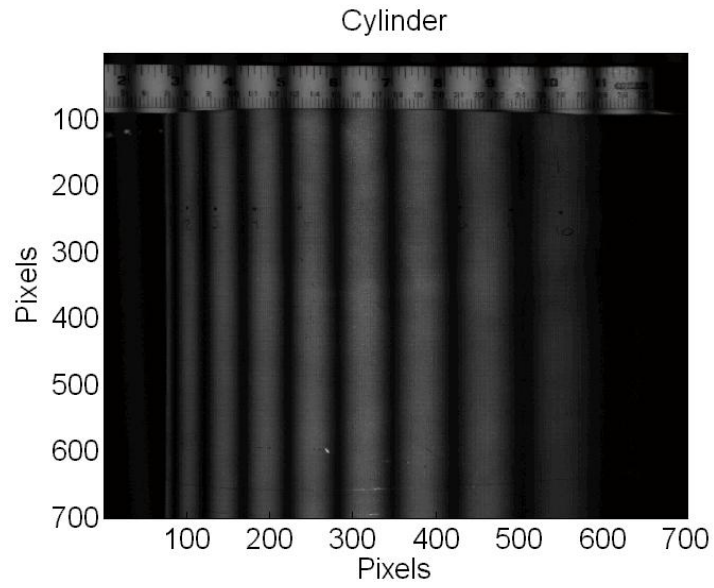
Fig. 6. 2. Calibrated cylinder testing for demonstration of accuracy.

Figure 6.3 shows a 3D representation of the cylinder with appropriately scaled *x, y, z* axies, all values are set in centimeters.
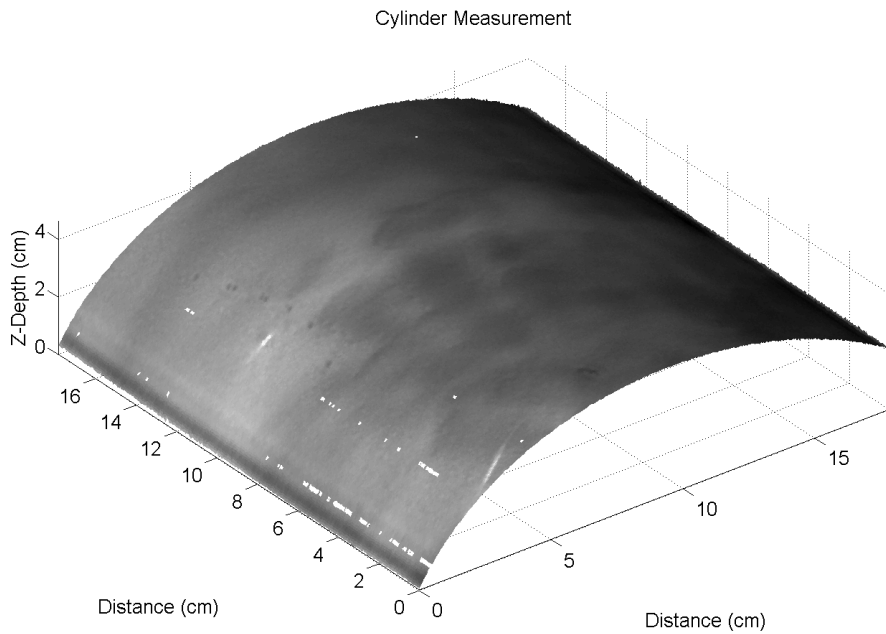
Fig. 6.3. Normalized, scaled 3D representation of cylinder.

Extracting a cross-section from this data, the height variation can be viewed, Fig. 6.4, along position line 250.
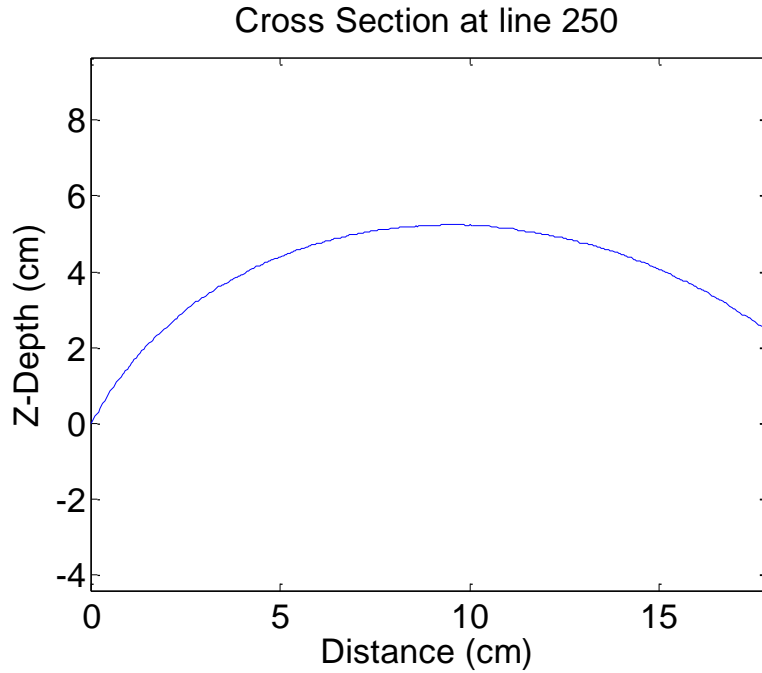
Fig. 6.4. Measured cylinder cross section from Fig. 6.3.

The most important evaluation is in the calculation of the cylinder radius measured from the fringe projection system and comparing this result against the value of the calibrated cylinder. A method for calculating this radius value was incorporated based on the curvature of the surface, Eq. 6.1.

$$r = \frac{|1 + f'^2(x)|^{3/2}}{|f''(x)|} ,$$
(6.1)

where r is the radius of curvature, *f(x)* is a polynomial function fit to the curvature of the data with the first and second derivatives. The average radius was evaluated at 12.714 cm (5.0056 inches). The given calibrated radius was measured at 12.7 cm (5.00 inches), which validates the systems measurement accuracy. From this data, the resolutions of the system can be determined. It's important to note that the *x* and *y* resolutions are directly related to the magnification factor, or the pixel size in the corresponding FOV. The most important factor is the *z-depth* resolution, calculated as the smallest measured step in the height distribution. The *z-depth* resolution was measured at 25.4 μm (0.001 inches), proving the sensitivity of the system.

6.2. Precision of system

The precision of the system is defined as the repeatability between measurements. This is directly related to an uncertainty analysis of the system variables. From chapter 2, the depth of an object can be determined via triangulation, Eq. 2.6.

$$Z_M = \frac{L\Omega}{2\pi f_O D} .$$
(6.2)

The measured values of each of these variables are used in the uncertainty analysis. The values of the unwrapped phase, Ω, was chosen to be a single measured value at a point on the surface of the cylinder, at a value of π in radians. The uncertainty of this variable was determined experimentally as a function of the standard deviation between measurements that vary temporally with the same fringe frequency and parameters. A full uncertainty analysis is shown in Appendix E, with the percentage contribution of each variable to the uncertainty resulting in a total *z-depth* uncertainty of $\pm$ 29.3μm ($\pm$ 0.00115 inches). The largest contribution

was directly from the uncertainty in the distance from the camera to the projector, D. From this data, the theoretical effects on the percentage contribution of each variable were determined as a function of increasing size of the object, which is proportional to an increasing value of Ω, Fig. 6.5.
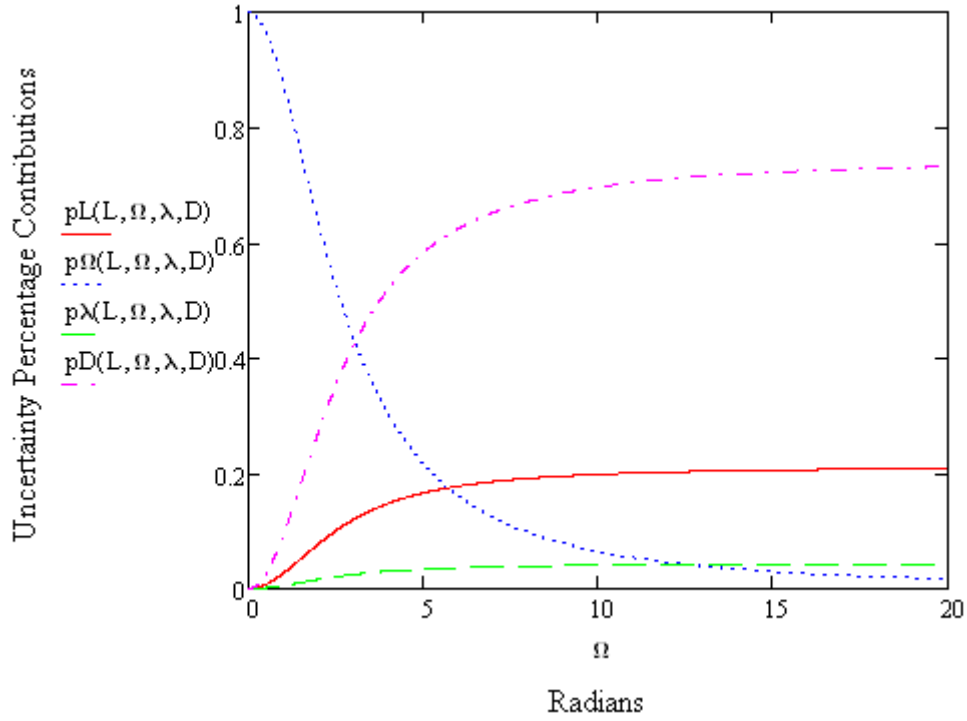
Fig. 6.5 Uncertainty percentage distribution as a function of increasing object depth.

From the graph in Fig. 6.5, it's clear that the as the size of the object increases, the percentage contribution from the value of the distance, *D*, becomes the highest source of uncertainty. The effects propagate significantly over approximately π radians until they level off at a threshold value. Another interesting effect that can be theoretically evaluated is the effects of the uncertainty in the *z-depth* as a function of the size of the object, Fig. 6.6.
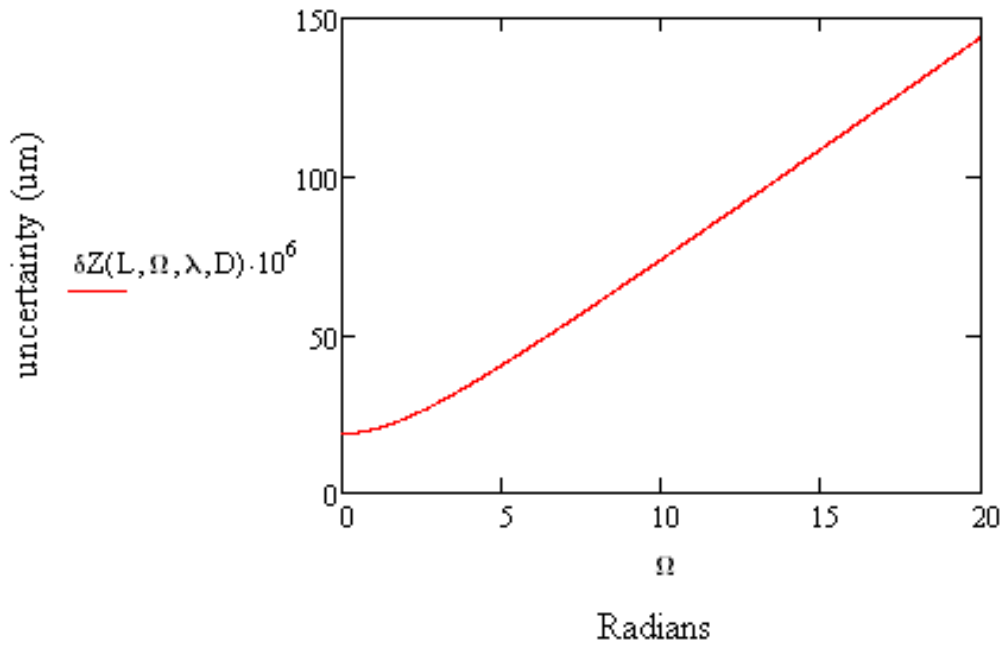
Fig. 6.6 *z-depth* uncertainty as a function of increasing object depth.

As the size of the object increases, the uncertainty in the *z-depth* also increases. These effects are only as significant as the required resolution of the application. Yet, the major result to note is that the uncertainty is proportional to the object size when the wavelength is normalized based on pixel size. Additionally, an assumption is made that the degradation of focus from the fringes does not constitute a major source of error, although it could potentially

play a large role in the system error. These effects are yet to be determined and could be the limiting factor for the depth of the object under measurement.

7. REPRESENTATIVE APPLICATIONS

As validation of the systems versatility and robustness in a variety of applications and conditions, several applications are outlined. The first application was in collaboration with Trilion Optical Test Systems and Northeastern University for the quantification of potholes and cracks in the road. The key attributes of this test were high speed performance under instable conditions. The second test was conducted in collaboration with the Worcester Art Museum (WAM) to digitize an ancient sculpture. The key attribute for this test was accuracy. Both of these applications have completely different requirements and directly test the versatility of the system in environments outside the laboratory.

7.1. Road measurements at driving speeds

Potholes, cracks and uneven pavement cost the average driver approximately $400 each year [Cal Watchdog, 2011]. These conditions can occur as a result of weather, wear, car accidents, or construction and are a danger to both drivers and pedestrians. Therefore, it is important to be able to record and evaluate these conditions so that a base for improvement can be identified.

VOTERS (Versatile Onboard Traffic Embedded Roaming Sensors) is a project designed to provide an accurate, detailed road assessment and maintenance system. The program is part of the National Institute of Standards and Technology's (NIST) Technology Innovation Program that supports "innovative and high-risk, high-reward research in areas of critical need" [VOTERS, 2010]. Its overall goals involve a sensing and detecting system that can be adhered to a vehicle in order to map out large areas. There are three main sensing subsystems to be

developed for this project to gather maximum information of road quality. Acoustic systems will be used to measure particle interaction with tires during normal driving, ground penetrating radar will be used to subsurface delamination and corrosion, and optical profilometry will be used to measure surface profiles and detect anomalies. With the development of the 3D shape measurement system, our system was chosen to be tested for the detection of cracks at driving speeds. Other portions of the project are in collaboration with Northeastern University, Trilion Optical Test Systems, The University of Vermont, UMASS Lowell, and Earth Science Systems (ESS).

The team at Worcester Polytechnic Institute is working on the Surface Optical Profilometry Roadway Analysis (SOPRA). The aims are to use optical techniques to map out details such as crack depth. By addressing a compelling societal need, this system has many applications. Eventually, the surface profiles can be expanded to aid in bridge maintenance. Global positioning systems can use thresholding algorithms that warn of cracks of particular dimensions or depth that need maintenance.

The system is incorporated into USPS vans, which means that there is no disruption to daily traffic. This saves time and money by providing real-time information and eliminating the need for work zone analysis. This positively impacts the environment by eliminating additional vehicles and gas consumption to conduct testing. Also, the compact instrument package does not affect the driver, who does not need to interact with the system while it collects data [NIST, 2009].

7.1.1. Application analysis and preparation testing

The key criteria for this application are accuracy, mobility, speed, and range. To summarize, the FOV of the system has to encompass an area of up to one square meters at a distance of approximately two meters from the road. The system has to be mobile and easily mountable. High accuracy is required, with a 1 mm (0.04 inches) *z-depth* resolution. The objective was to make measurements at driving speeds up to 60 mph, thus requiring high operating speeds.

Pretesting was done to evaluate important factors for this application, particular the reflective spectrum off of the pavement. Fig. 7.1 shows the spectrum evaluated by using spectroscopy software with the USB2000+ Miniature Fiber Optic Spectrometer developed by Ocean Optics.
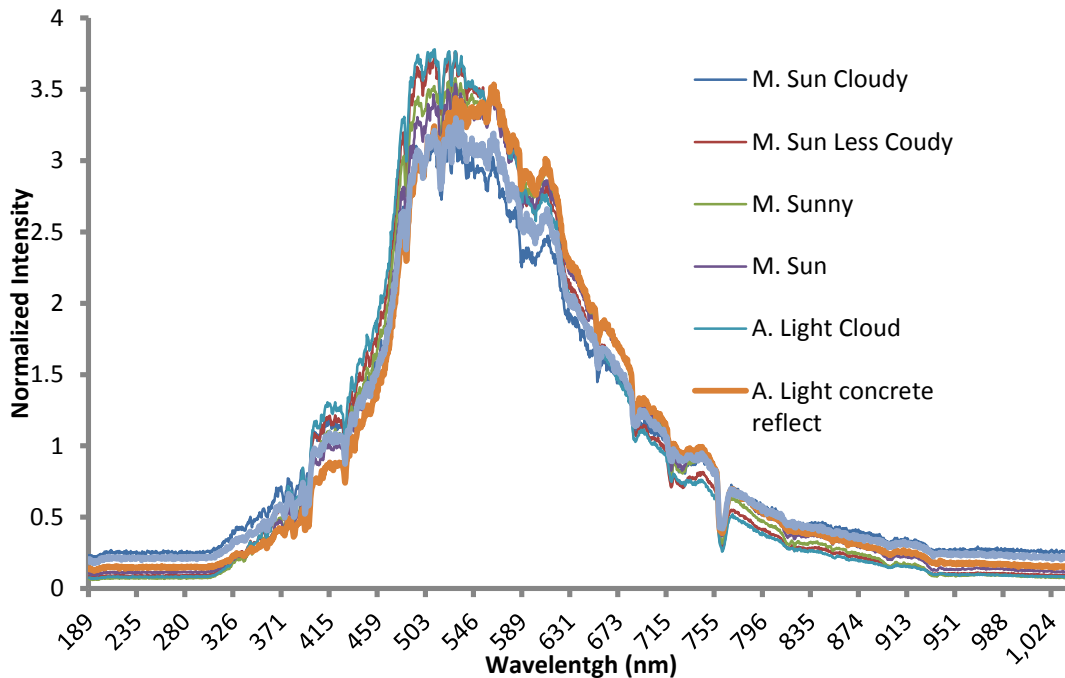
Fig. 7.1. Spectral analysis during different times of the day.

The data shown in Fig. 7.1 is normalized for comparative purposes to see effects during different times of the day, both morning and afternoon, with and without cloud cover, and reflectivity off concrete and asphalt. Camera filter's based on the wavelength of our system, approximately 620 ± 20 nm, improves contrast and must be used in this application. It's important to note that the spectrum intensity is reduced by a factor of approximately 300 under the reflected concrete and asphalt conditions as compared to 'A. Light Cloud' at a wavelength of 620.4 nm.

7.1.2. System setup and integration

A general testing procedure was developed via collaboration with Northeastern University. A Chevy Express van for testing was provided with an environmentally isolated camera housing system. The van had already been optimized for road measurements with the integration of UPS, GPS, and mounting beams on the van roofing. Through collaboration, our setup was modified for the attachment to the mounting beam off the roof. A preliminary design of the mounting configuration can be seen in Appendix F, with the incorporation of both the camera and projector using a 3 beam system. In the final stages of the iterative design process and via collaboration with Northeastern University, an optimized configuration was chosen by the adding an adapter plate used to attach the system to the mounting unit. Therefore, the entire system was directly attached to a single ten foot mounting beam from 80/20 Inc., product 2040, Fig. 7.2. The camera was attached to another parallel 80/20 Inc. ten foot 2040 beam.

Fig. 7. 2. Realization of system mounted onto the van at Northeastern University.

The system was to run with a Pike AVT F-505, 5 megapixel camera to achieve the desired resolution at the given FOV and distance from the road. The camera pixel size was 3.4 x 3.4 μm^2. The maximum frame rate at this resolution is 15 fps, which would gather single images for FFT analysis. To create a continuous animation of the road, captured frames must be overlapped by a minimum of 50 percent. Therefore, using this criterion as a baseline and knowing that each frame covers one full meter minimum, the maximum speed of the van under current conditions was calculated to be 16.8 mph, which was obtained by:

$$\frac{15 \; frames}{second} * \frac{.5 \; meters}{frame} * \frac{2.237 mph}{1 \frac{m}{s}} = 16.8 \; mph \,. \tag{7.1}$$

One of the major concerns for this application is the effects of vibrations on the system. Future work would focus on improving the stability and reducing vibrations that could affect

measurements. Yet, preliminary resonance frequencies were modeled using SolidWorks Simulations. The results can be seen in Fig. 7.3 for the first bending and torsional mode with the system fixed at the location where the beam is directly attached to the roofing of the van.

<table>
<tr><td>(a)</td><td>(b)</td></tr>
</table>
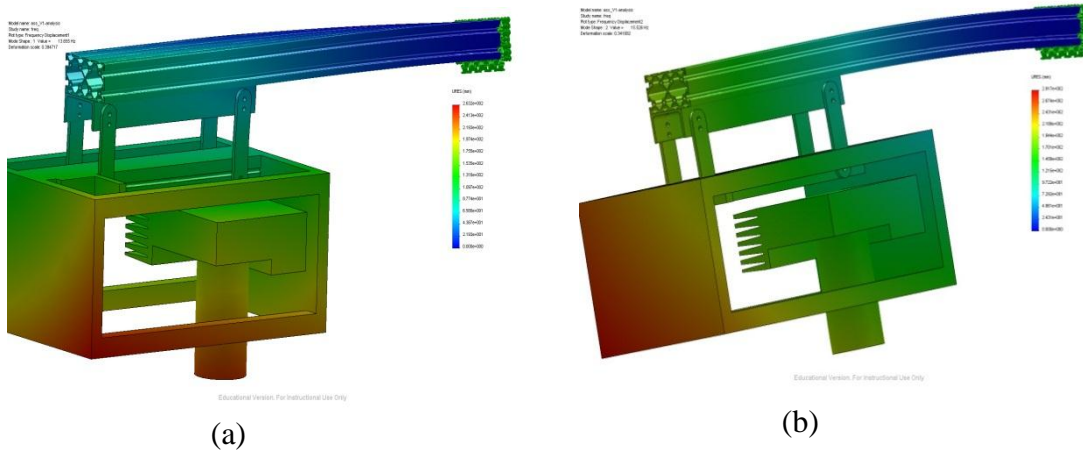
Fig. 7.3. FEM modal analysis of the optical system: (a) first torsional mode; and (b) first bending mode.

The results can be summarized in Table 7.1 for the first five modes of vibration, where frequency numbers 1, 3, and 5 are torsional modes and frequency numbers 2 and 5 are bending modes:

Table 7.1. FEM prediction of the first five frequency modes of vibration.

Frequency Number	Hertz
1	13.655
2	15.526
3	47.291
4	58.02
5	88.664

The results are important because they show another limitation of the current developed system for use at higher speeds. Cross winds, amongst many other factors, will generate to large vibration modes that will have to be corrected for in the data analysis. For that reason, lower speeds from 0-10 mph were used for testing. A more complex mounting system would be used for the final integration of the system.

Calibration was done by using the same procedure as outline in chapter 4. Yet, in this case, the system was calibrated once it was attached to the van system. Using a relatively flat surface and projecting a box pattern, the deformation can be observed and calibration matrix recovered, Fig. 7.4.
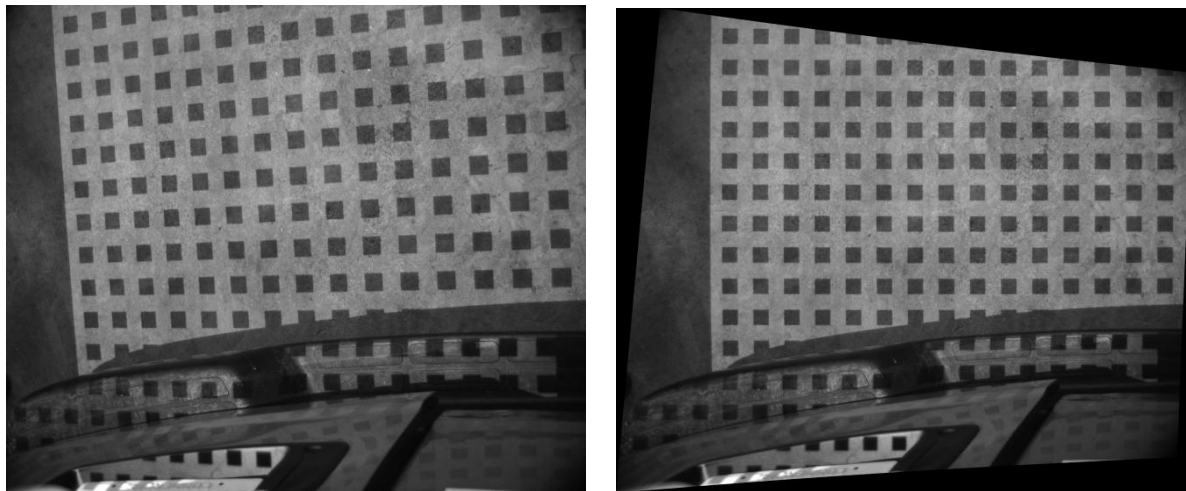
(a)   (b)

Fig. 7.4. Calibration procedure: (a) original image; and (b) calibrated image.

7.1.3. Static Testing

Once the system was properly mounted to the vehicle, static testing was done at one location. For this, the exposure time was increased to approximately 25 ms at full aperture to improve the quality of the image. A sequence of sinusoidal projections were captured and evaluated. The results can be seen in Fig. 7.5 using the 4 phase step method and a surface overlay to keep the same texture of the road.
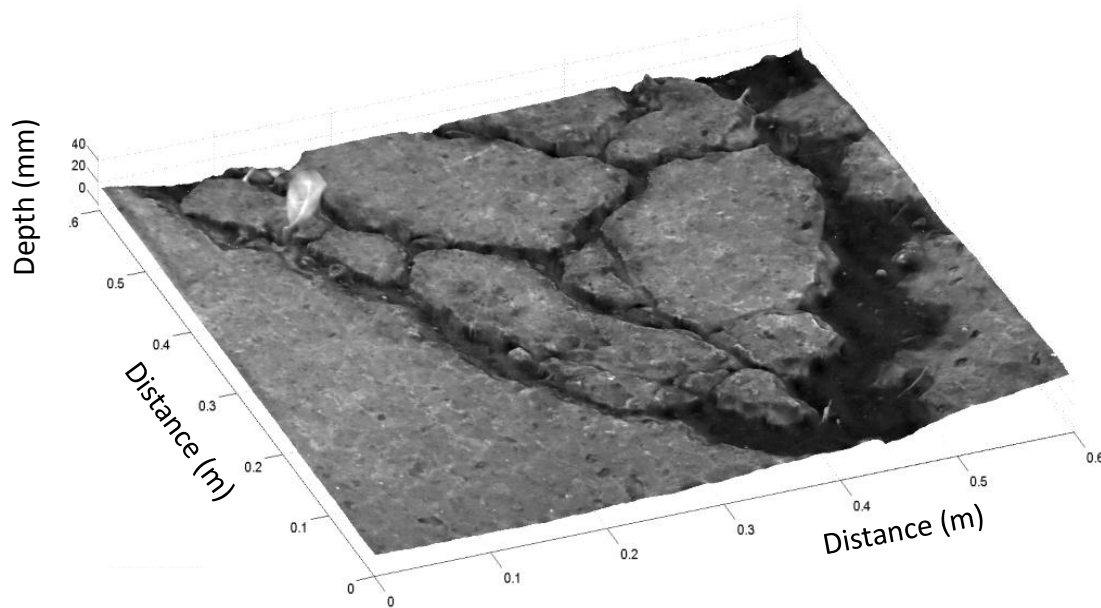
Fig. 7.5. 3D scaled model of the road .

The data was appropriated scaled in the *x, y, z* directions in order to get quantitative measurements from the road surface. The typical *x* and *y* resolutions at this distance were approximated to be 0.254 mm (0.01 inches). Based on experimental calculations the *z-depth* resolution has been approximated at $\lambda/30$ value, where λ is the scaled value of the fringe

wavelength. Thus, the *z-depth* resolution was approximated to be 0.737 mm (0.029 inches) based on a value of λ of 2.2 cm (0.866 inches). A cross section of the data was taken at 0.4 meters vertically and plotted. The results can be seen in Fig. 7.6.
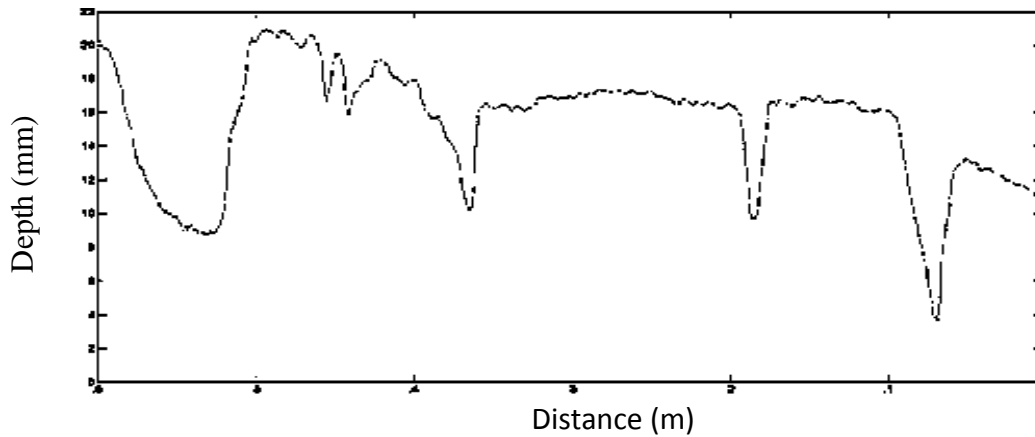
Fig. 7.6. Quantitative cross section of the road measurement data.

7.1.4. Dynamic testing at driving speeds

Preliminary testing was conducted at speeds ranging from 0-10 mph. Images were captured and analyzed using FFT methods and the results are displayed in Fig. 7.7.
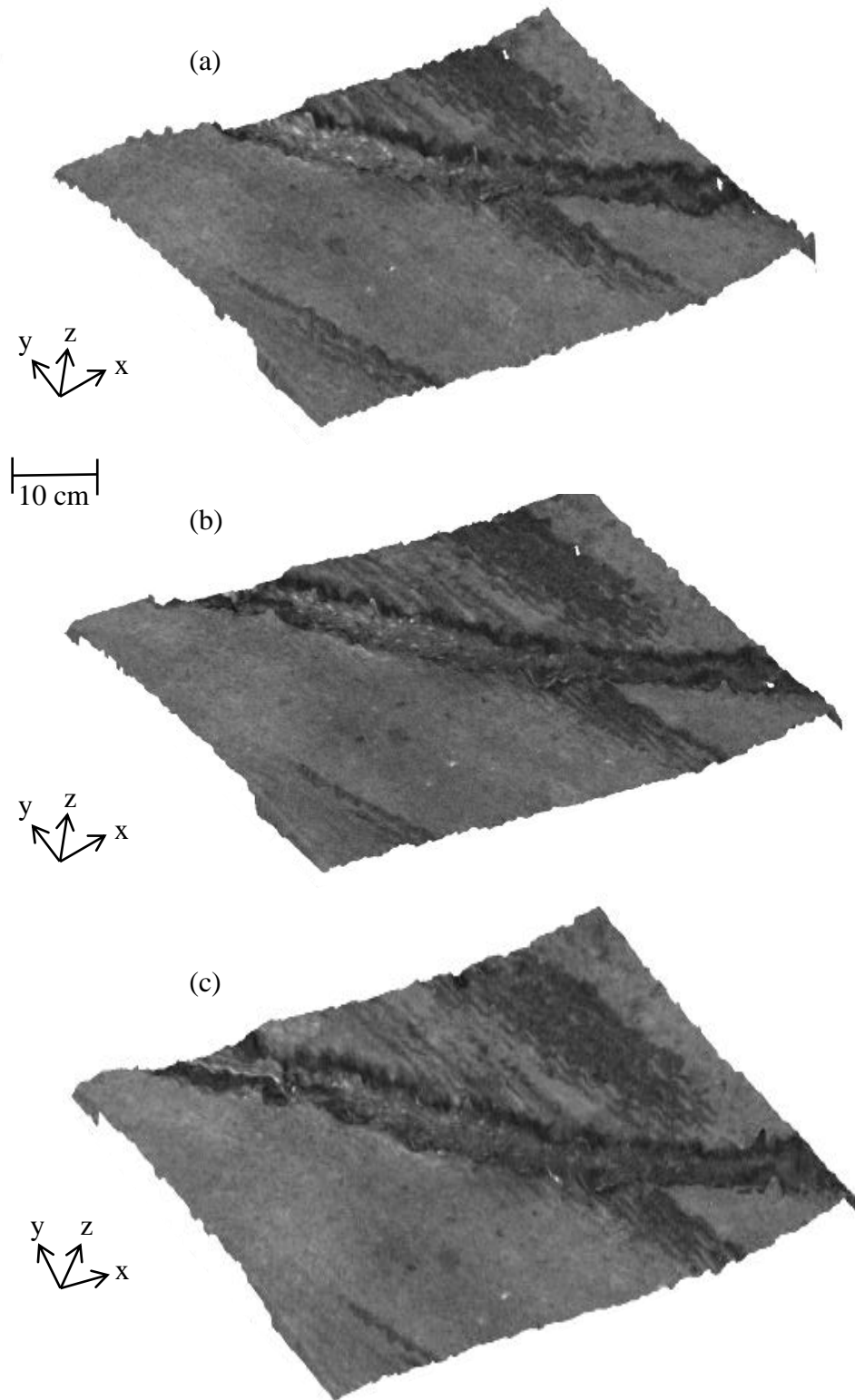
Fig. 7.7. Measurement analyzed using FFT methods at 5 mph driving speeds (a) starting position, (b) position 2, and (c) position 3.

The measured speed of the system was completed by knowing the distance travelled between frames and the exposure time of the camera. Thus, a simple calculation can be performed to convert to the standard miles per hour. The developed system was successful able to capture, analyze, and render quality images in instable conditions. This validated the applicability of the system under dynamic environments. Additional steps will be taken to use correlation algorithms to stitch images of the road together to create dynamic scenes. Together with GPS systems, cracks and breaks in the road, such as those identified in Fig. 7.7 would be flagged for maintenance.

7.2. Sculpture digitization for art conservation

With the overabundance of artwork that has been acquired by museums, the study of art has become an important phenomenon. Sculptures and other three dimensional art forms portray important parts of history dating back thousands of years. It is astounding that some have survived to date. The information and education they can provide to students and art enthusiasts is endless. Over the recent years, cultural pieces have been threatened by many factors including population growth, urban development, possible natural disasters, man-made environmental hazards, and potentially the most dangerous threat - lack of money for preservation [Pieraccini, 2001]. Therefore, preservation of these priceless pieces relates directly to the scientific field via digitization using non-invasive techniques. Additionally, there is an advantage to having quantitative 3D representations of models for a number of reasons:

- Direct comparison of original models before and after restorations to examine the quality of the restoration.

- Visual preview of a restoration before implementation for minimal impact on the sculpture.

- Original 'vibrant' color representation can be modified and previewed.

- Replication process using a digitized model is safer and quicker than a molding process.

- Models can be implemented in a virtual environment for wider use.

As important as it is to study these art forms, conservation is critical for their survival. However, probes and other similar devices shouldn't be used because of the artwork's sensitivity. In addition, some pieces cannot be moved or placed into a specific area for measurement. Therefore, there is a great need for a novel non-contact, portable method for art conservation. This method does not affect the integrity of the sculpture and eliminates the possibility for damage. It is unique because one can easily transport it to a specific location if the artwork cannot be moved. For example, this device can be brought on location to archeological sites. Images can be taken, digitized, sent anywhere within a few hours. This provides fast, widespread access to information as well as a safe, detailed projection of the artwork. Another advantage is the affordability of this type of system and simplicity of a developed system for measurements.

There are several requirements for the system. First, a full field of view must be available. Next, one must be able to record at large resolutions, which will help to attain details and greatly aid in art restoration by producing quantitative information as to the size and shape of the object. For example, using a digitized image, a sculpture can be restored based on the location of a particular crack. The restoration can be validated simply be digitizing the new sculpture. Using this technology, one would be able to see what a restoration would look like prior to applying it. By providing this prediction system, the result is more accurate, realistic

restorations. To test the applicability of the system for this type of environment, the system was

tested in laboratory environments and the results can be seen in Fig. 7.8. The results shown are

from a sculpture 'David' from a single orientation.
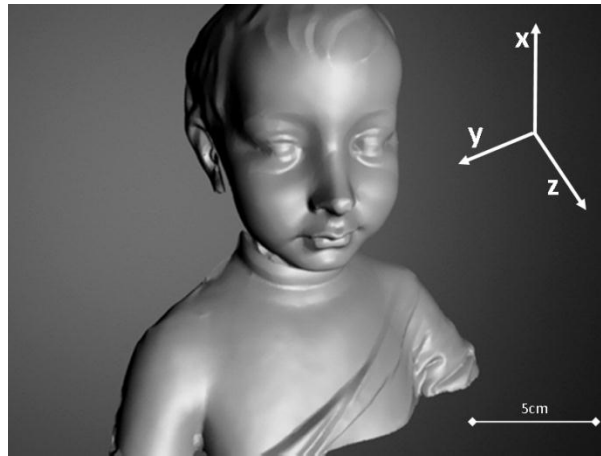
Fig. 7.8. Digitized sculpture in laboratory conditions.

The lab render was successful and has potential for further sculpture digitization. Some

important attributes to consider are the sculptures original colors. The sculpture used in lab

testing was a uniform white, although many ancient sculptures have complex surface colors and

features. By combining this technique with chemical analysis there is a potential to determine

the type and colors of original paint used, thus providing more information on the history of the

piece. One would also be able to use the digitized image to change colors of portions of the

sculpture to more accurately represent the model. This original replica can be used for restoration

or digital record keeping.

As a proof of concept, the fringe projection system developed was demonstrated and tested at the Worcester Art Museum in Worcester, Massachusetts. Measurements were made on a late 4th century-3rd century BCE Orant sculpture. Figure 7.9 shows two of the Orant Sculptures that are currently under restoration at the Worcester Art Museum.

Fig. 7.9. Orant Sculpture at the Worcester Art Museum.

The objects are named *Funerary Statue of a young maiden* made of Terracotta with kaolin slip. Although the artist in unknown, it is evident that the pieces come from Canosa, South Italy [Klausmeyer, 2011]. The rightmost statue in Fig. 7.9 is under consideration because

the head on the sculpture is believed to be cast during the late twentieth century from another sculpture. Due to the casting processes, it's thought that the head is slightly smaller than intended. As a result, there is a small distortion between the head and body. One of the objectives of the testing is to make quantitative measurements on the sculpture that provide an alternative means of analysis and fabrication. The full dimensions of the rightmost Orant sculpture in Fig. 7.9 under consideration are 92.6 cm x 31.6 cm x 22 cm. The system setup and testing procedure for this application are outlined in the proceeding sections.

7.2.1. High resolution static testing procedure

A basic testing procedure was developed, where the sculpture was placed at the center of a room with uniform lighting and projection system was placed at a distance of 2.5 meters away from the object with the camera at an angle of 30 degrees. Figure 7.10 shows a general schematic of the setup with the projection system at a particular angular location and radius, θ_R, from the object.
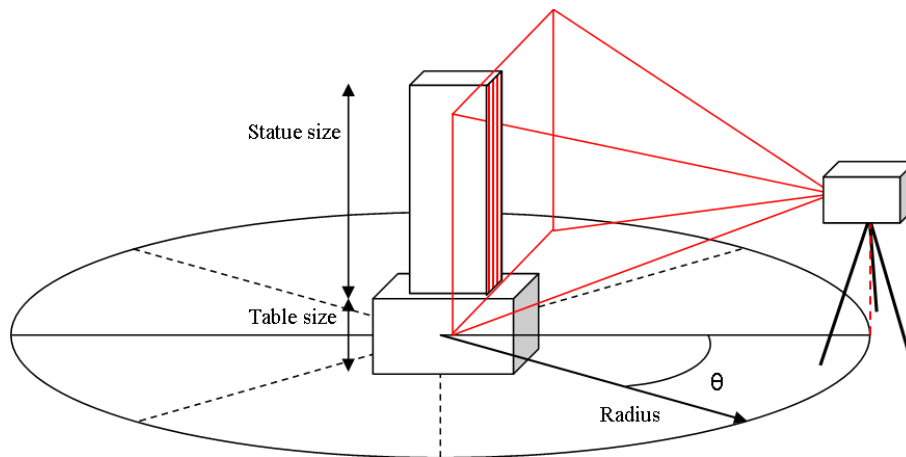
Fig. 7.10. Schematic of Worcester Art Museum system setup.

For most art conservation applications, minimal movement of the object is required for measurements. In the design phase for this particular application, an assumption was made that the statue location was fixed and the mobility and versatility of the system would be utilized to digitize the art piece. Yet, for convenience, colleagues at the Worcester Art Museum placed the piece on a rotational stage. Measurements were taken using a 9 bit 24 fps projection speed acquired with a one megapixel CCD camera. For high resolution results, the 16 phase step algorithm was used to calculate the wrapped phase map. Eight densities were recorded for each position ranging from 4 pixels per fringe to 512 pixels per fringe that could be used in the more robust temporal unwrapping algorithm. The sculpture was then rotated every 30 degrees and the same procedure for data acquisition was used until the entire model was digitized at 360 degrees. An image of the system setup with the sculpture at the art museum is shown in Fig. 7.11.
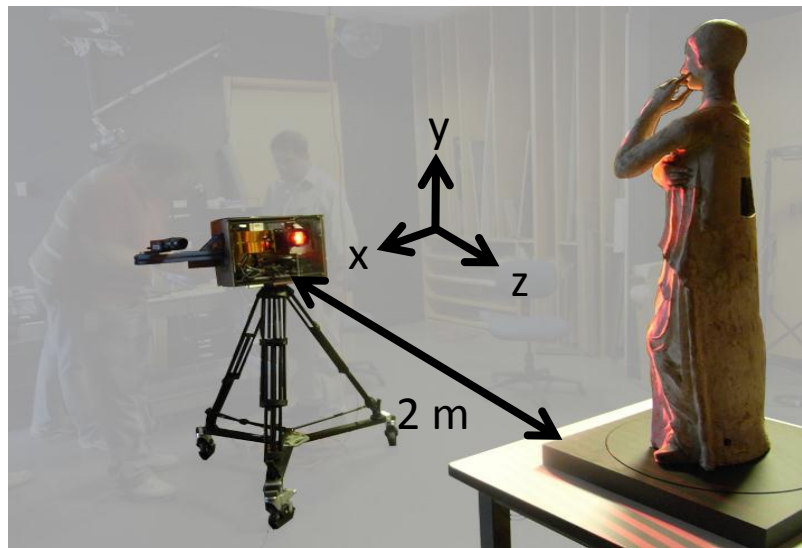
Fig. 7.11. System Setup at the Worcester Art Museum with Sculpture on
Rotational Stage.

Calibration was done using the same procedure outline in chapter 5. The system was at a fixed angle and using a reference surface, the angle was removed statistically along with the aberrations from the lens. Figure 7.12 shows the pre calibrated and calibrated images.

<div align="center">(a)   (b)</div>
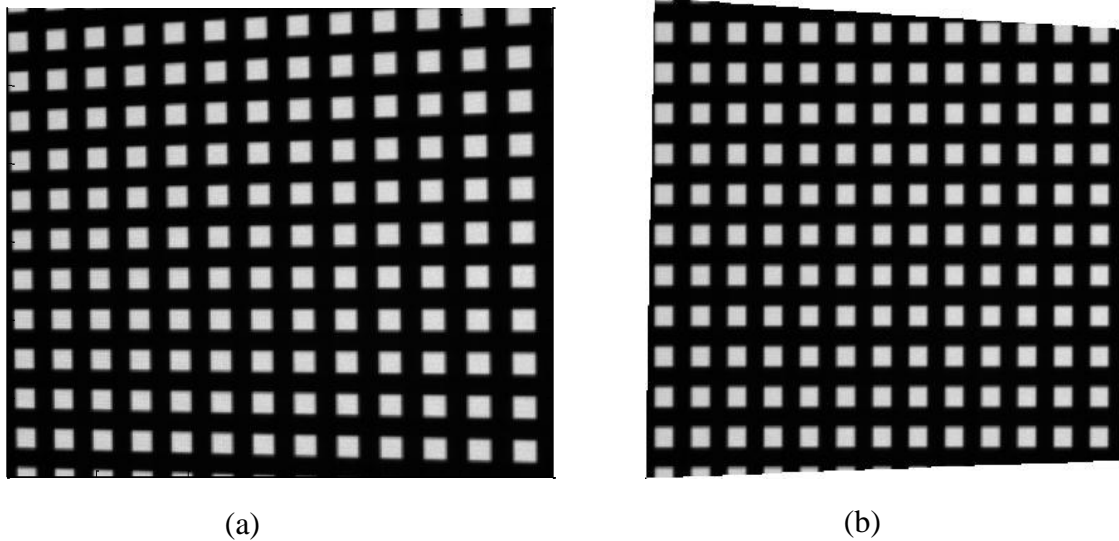
Fig. 7.12. Calibration of system (a) Image before calibration; and (b) after calibration

7.2.2. Representative results

Measurements were taken at two different locations. The first was at the distance from the sculpture of approximately 3.05 meters (10 feet) to get a full FOV of the entire sculpture. Although resolution is decreased at such a large distance, results indicate that the system is able to capture and recover 3D information over the entire sculpture. The given point cloud can be seen in Fig. 7.13a using a software called Leios for rendering. A 3D view of the full sculpture from a single position is shown in Fig. 7.13b.

(a)   (b)
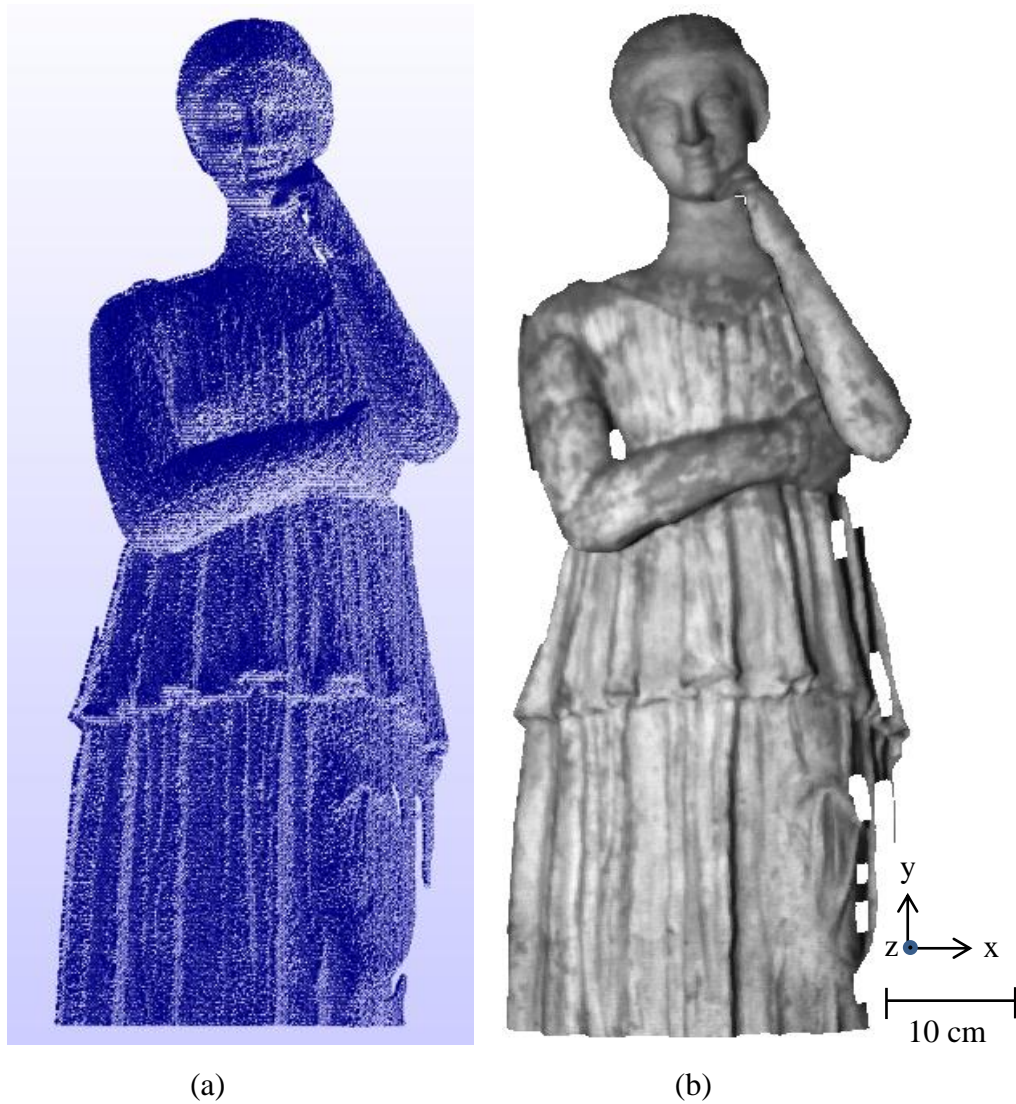
Fig. 7.13. 3D reconstruction of data (a) As viewed in Leios with
mesh; and (b) with color map and shifted orientation.

It's clear from the analysis that there are effects of shadowing and many views are
needed for full reconstruction of measurements. The second position for measurement
was of approximately 1.2 meters (4 feet) from the sculpture to the system. Similar
system resolutions outlined in chapter 6 are expected at this distance. The reason for
choosing this particular distance was because a focus of the experiment was to resize the

particular head of the sculpture. Once again, there is a possibility that the head was cast and current thinking is that the casting process likely contributed to the restoration head being disproportionally small for the body.   A front view of the digitized head can be seen in Fig. 7.14 with a section view showing the quantitative nature of the measurements.

(a)   (b)
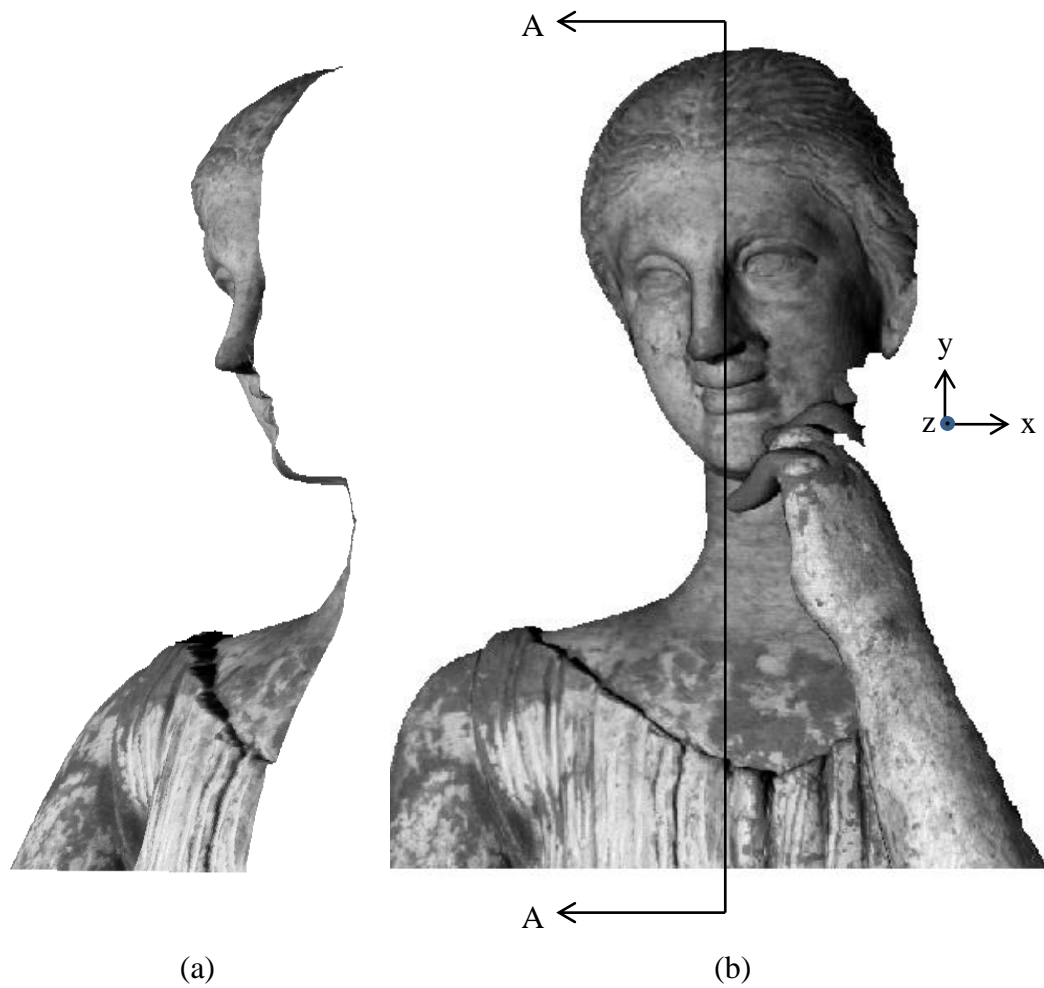
Fig. 7.14. Front view of sculpture (a) Section view through AA showing contour; and (b) full front view.

One of the objectives for this particular application was to digitize the current head and increase its size by an appropriate value based on proportions between the head and shoulder size or the ratio of head to body size. Discussions between curators and conservators on whether to exhibit the figure with or without the restoration head are ongoing, however 3-D modeling of the restoration head using fringe projection may offer a third alternative by providing the means by which to fabricate an accurate reproduction of the restoration head that is proportionally larger and thus more consistent with the original figure.

The same testing procedure was conducted and the sculpture was again rotated every 30 degrees to gather 360 degrees of information for digitization. Preliminary sculpture results are shown in Fig. 7.15 from a rotated view of the sculpture.
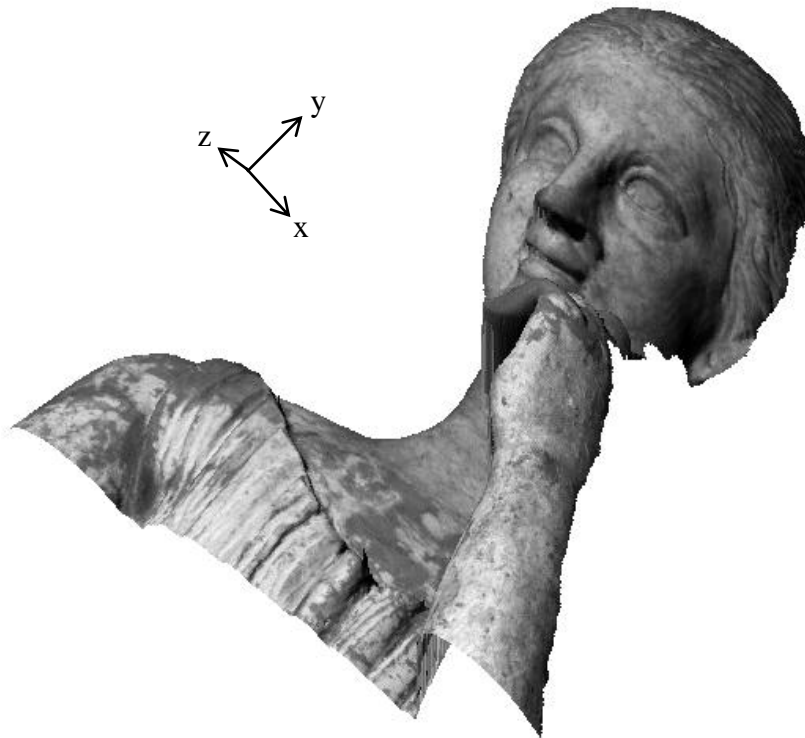
Fig. 7.15. Front view of sculpture at angled orientation.

Data was analyszed from every 30 degree position. To summarize some of the results, every 90 degree rotation has been analyzed and can be seen in Fig. 7.16. For this analysis, the original texture of the figure has been mapped over the data. Altough future work is being conducted on the alterations of the color scheme.
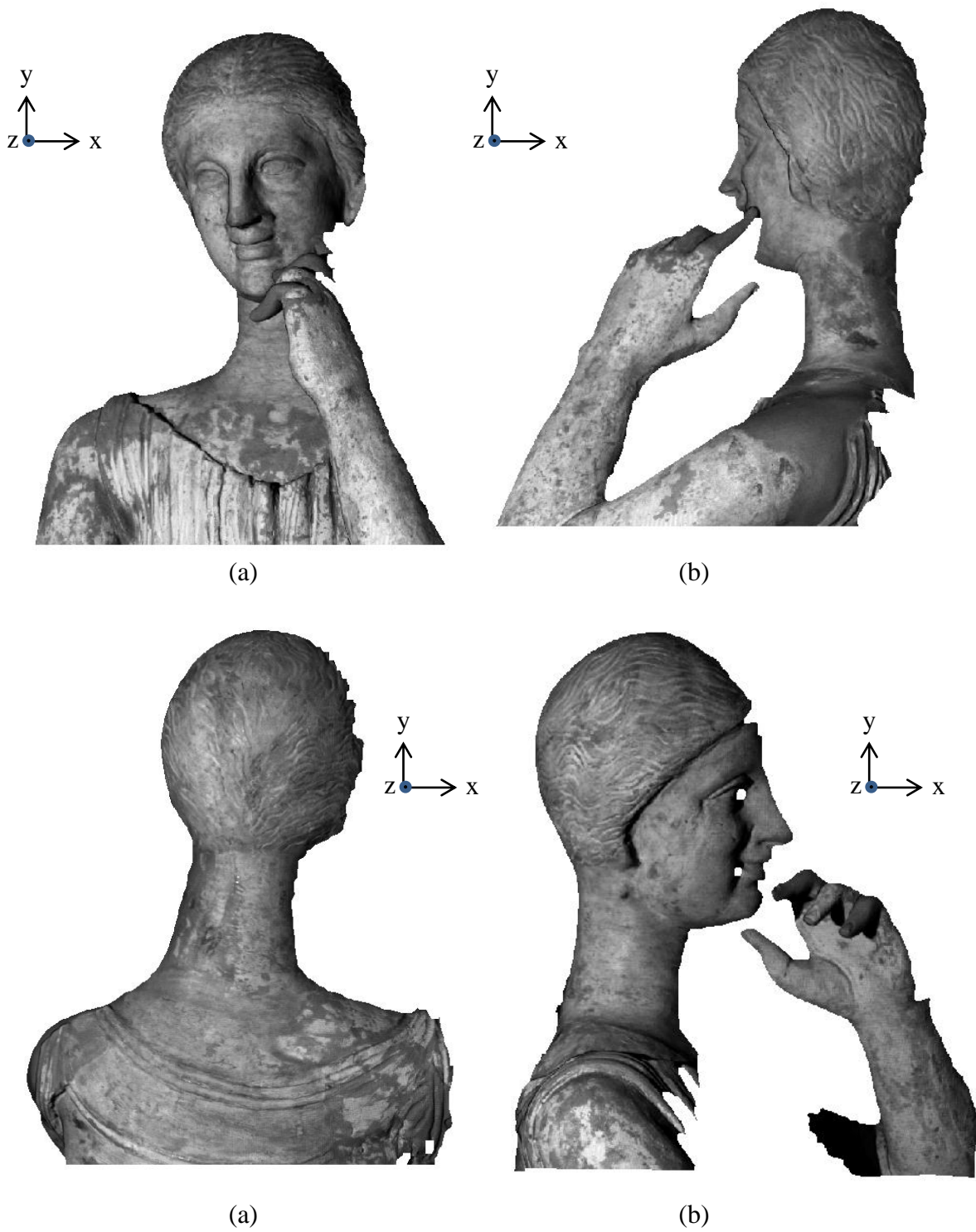
Fig. 7.16. Results of sculpture rendering at 4 views (a) Front side view at no rotation; (b) right side view at 90 degrees rotation; (c) back side view at 180 degrees rotation; and (d) left side view at 270 degrees rotation.

There are several important points to acknowledge with this particular application. The task requires images from many angles because the fine details create shadows that make rendering difficult. Also, to get the full appreciation for fringe projection for art conservation, a stitching algorithm needs to be developed to render complete models.

7.2.3. Analysis of resolutions and potential improvements

Based on the appropriate distance of the Orant sculpture from the object for the measurements of the head, the x and y resolution are approximately at 0.381 mm (0.015 inches). The *z-depth* resolution was approximated at 68.6 μm (0.0027 inches) based on a fringe wavelength value of 2.05 mm at its highest density. To improve this resolution there are several changes to the system that should be made. First, the FOV of the camera and projector should be matched as precisely as possible. Figure 7.17 shows the extent of the projection area, approximately 3 meters, to obtain a less than 1 meter FOV from the camera.

Fig. 7.17. Projection system FOV at approximately 2 meters form the Orant sculpture.

Additionally, by reducing the size of the pixels on the camera, and increasing the fringe frequency on the object, there can be even greater improvements on the spatial resolution in *x, y*, and *z*.

In summary, there are many potential applications for this technology and room for advancements as well. The system has also been tested for forensic applications with footprint detection and measurements on the surface of United States coins [Hanquier, 2011].

8. CONCLUSIONS AND RECOMMENDATIONS

A method for quantitative 3D shape measurements was successfully identified and developed that provides superior versatility for an endless list of applications. Advanced algorithms were incorporated into the system for measurement of dynamic scenes and high resolution static scenes. The versatility is unparalleled in all aspects of the development, from packaging, to unwrapping and calibration techniques. Evaluations conducted on the final system validated the theoretical concepts defined by the mathematics.

The system was applied in two contrary applications. The first was for high speed road measurements where stable conditions were difficult to achieve and high speed acquisition was necessary. The next was for sculpture digitization at high resolutions where speed was less of a concern, but accuracy played a critical role. The system successful recovered quantitative 3D shape information from both of these applications that validate the systems potential.

Future improvements can be made in several aspects of the system. First would be the packaging. A second generation prototype needs to be developed that incorporates automated features, particularly changing the angle of the camera, with a direct feedback system that has a pre calibrated matrix integrated for different camera positions. Secondly, post processing needs to be streamlined and incorporated into LaserView for real-time 3D viewing. In order to do this several aspects must be advanced. First, the spatial and temporal unwrapping techniques must be integrated into the software. Heavy processing power from the software may be required so algorithm optimization is necessary.

Other visualization improvements need to be made to the system. Optimization of meshing procedures could reduce high frequencies and more accurately represent the surface profiles. Additionally, precision stitching of information is necessary in all applications. For

instance in the road measurement application, portions of the road need to be linked to create a 'map' for better visualization. In art conservation, stitching is needed to view the entire full FOV of the sculpture. The accuracies of this method are critical in retaining the accuracy of the system for quantitative measurements. The difficulty lies in the limitation of error propagation as a function of the number of stitched images.

Overall, the development of the system was successful for quantitative 3D shape measurements. Interesting developments could be made with the combination of this system with other optical systems for non-invasive measurements. Some examples include Shearography [Pryputniewicz, 1992] and Reflective Transformation Imaging (RTI) [Malzbender et al., 2000].

9. REFERENCES

Bothe, T., Osten, W., Gesierich, A., and Juptner, W., "Compact 3D-Camera," *Proc. SPIE*, 4778:48-59, 2002.

Burke, J., Bothe, T., Osten, W., and Hess, C., "Reverse Engineering by Fringe Projection," Interferometry XI: Applications, *Proc. SPIE* 4778:312-324, 2002.

Cal Watchdog, On-line: http://www.calwatchdog.com/2011/03/24/wealthy-and-poor-california-spongers/ , 2011.

Cloud, G., *Optical Methods of Engineering Analysis,* Cambridge University Press, 1998.

Dodgson, N., "Variation and extrema of human interpupillary distance," *Stereoscopic Displays and Applications*, *Proc. SPIE* 5291:36-46, 2003.

Dornaika, F. and Hammoudi, K., "Extracting 3D polyhedral Building Models from Aerial Images using a Featureless and Direct Approach," *Proc. IAPR/MVA* 12:378-381, 2009.

Engineers Edge, "Coordinate Measurement Machine CMM About" on-line: http://www.engineersedge.com/inspection/coordinate_measurement_machine_cmm.htm, 2011.

Furlong, C., *Hybrid, experimental and computational, approach for the efficient study and optimization of mechanical and electro-mechanical components*, Ph.D. dissertation, Worcester Polytechnic Institute, 1999.

Ghiglia, D. C. and Pritt, M. D., *Two-Dimensional Phase Unwrapping: Theory, Algorithms, and Software,* John Wiley & Sons, Inc., 1998.

Gonzales, R., Woods, R., Eddins, S., *Digital Image Processing using MatLab*® Gatesmark Publishing, 2009.

Gorthi, S. and Rastogi, P., "Fringe projection techniques: whither we are," *Opt. Lasers Engg.,* 48:133-140, 2010.

Grimm, T., "Selection Criteria for Common Applications," T.A. Grimm & Associates, Inc., 2009.

Hanquier, M., *Personal communication with Maxime Hanquier*, 2011.

Harrington, E., Furlong, C., Rosowski, J. J., and Cheng, J. T., "Automatic Acquisition and Processing of Large Sets of Holographic Measurements in Medical Research," *Proc. SEM,* 5:219-228, 2011.

Hornbeck, L. J., "Digital Light Processing for High-Brightness, High-Resolution Applications," *Proc. SPIE*, 3013:27-41, 1997.

Hofling, R. and Aswendt, P., "Real Time 3D Shape Recording by DLP® Based all-digital Surface Encoding," *Proc. SPIE,* 7210:E-1-E-8, 2009.

Huntley, J. M., and Saldner, H. O., "Shape measurement by temporal phase unwrapping: a comparison of unwrapping algorithms," *Meas. Sci. Technol.* 8:986-992, 1997.

Jia, P., Kofman, J., and English, C., "Comparison of linear and nonlinear calibration methods for phase-measuring profilometry," *Opt. Engg.,* 46:043601, 2007.

Kinell, L., *Shape Measurements using Temporal Phase Unwrapping*, Licentiate Thesis, Lulea University of Technology, 2000.

Klausmeyer, P., *Personal communications with Dr. Klausmeyer from the Worcester Art Museum*, 2011.

Kreis, T., *Handbook of Holographic Interferometry,* Wiley-VCH Verlag GmbH& Co. KGaA, Weinheim, 2005.

Malzbender, T., Gelb, D., Wolters, H., Zuckerman, B., "Enhancement of shape perception by surface reflectance transformation," *Tech. Rep. HPL- 2000-38R1.* Hewlett-Packard Laboratories, Palo Alto, California, 2000.

Morvan, Y., Farin, D., de With, P. H. N., "Acquisition, compression and rendering of multi-view Video," NXP Workshop, Eindhoven Technical University, The Netherlands, August 2007.

NIST, Technology Innovation Program: Project Brief, on-line: http://tipex.nist.gov/tippb/prjbriefs/prjbrief.cfm?ProjectNumber=080046, 2009.

Pieraccini, M., Guidi, G., and Atzeni, C., "3D digitization of cultural heritage," *Journal of Cultural Heritage* 2:63-70, 2001.

Pryputniewicz, R. J., "Electronic shearography and electronic holography working side by side," *Proc. SPIE*, 1821:27-37, 1992.

Salvi, J., Pages, J., Batlle, J., "Pattern Codification strategies in structured light systems," *Pattern Recognition*, 37:827-249, 2004.

Schuon, S., Theobalt, C., Davis, J., and Thrun, S., "High-quality scanning using time-of-flight depth superresolution," *IEEE Computer Society Conference on Computer Vision and Pattern Recognition Workshops*, 2008.

Sontheimer, A., "Digital Micromirror Device (DMD) Hinge Memory Lifetime," Texas Instruments, Inc. DLP Products, 2002.

Spagnolo, G. S., Guattari, G., Sapia, C., Ambrosini, D., Paloetti, D., and Accardo, G. "Contouring of artwork surface by fringe projection and FFT analysis," *Opt. Lasers Engg.*, 33:141-156, 2000.

Su, X., Zhang, Q., "Dynamic 3-D shape measurement method: A review," *Opt. Lasers Engg.*, 48:191-204, 2010.

Takeda, M., Ina., Hideki, I., and Kobayashi, S., "Fourier Transform method of fringe-pattern analysis for computer-based topography and interferometry," *J. Opt. Soc. Am*, 72:156-160, 1981.

Texas Instruments, "DLP System Optics," 2010a.

Texas Instruments, "DLP Technology," on-line: http://www.dlp.com/technology/, 2010b.

Texas Instruments, "DMD 101: Introduction to Digital Micromirror Device (DMD) Technology," July 2008.

Van Kessel, P. F., Hornbeck, L., Meier, R., and Douglass, M., R., "A MEMS-based projection display," *Proc. IEEE,* 86:1687-1704, 1998.

VOTERS: Versatile Onboard Traffic Embedded Roaming Sensors, on-line: http://www.northeastern.edu/voters/documents/VOTERS_one.pdf, 2010.

Whitehouse, D. J., "Review Article: Surface Metrology," Department of Engineering, University of Warwick, Coventry, UK, 21 May 1997.

Xiaobo, C., Xi, J., Tao, J., Ye, J., "Research and development of an accurate 3D shape measurement system based on fringe projection: model analysis and performance evaluation," *Prec. Engg.*, 32:215-221, 2008.

Yamauchi, K., Saito, H., and Sato, Y., "Calibration of a structured light system by observing planar object from unknown viewpoints," *IEEE* doi: 10.1109/ICPR.2008.4761303, 2008.

Zervas, M., Furlong, C., Harrington, E., Dobrev, I., "3D shape measurements with high-speed fringe projection and temporal phase unwrapping," *Proc. SEM*, 5:235-241, 2011.

Zhang, S., Huang, P. S., "Novel method for structured light system calibration," *Opt. Engg.* 45, 2006.

APPENDIX A: MatLab program for Fast-Fourier Transformation (FFT) analysis based on a single image.

```matlab
clc, clear all, close all

% Read Image

image=readRTI('F:\WPI_MS_Thesis\SOPRA\DSCN2849.jpg');
image=image';
image=flipud(image);
[X Y]= size(image)
x=round(X/2)
y=round(Y/2)

%Take FFT of image and separate real and imaginary components

ft_image=fft2(image);
ft_image=log(abs(ft_image));
ft_image=circshift(ft_image, [x y]);

figure
mesh(ft_image)
Grid off

Real=real(ft_image);
Real_shift=circshift(Real,[x,y]);
Img=imag(ft_image);
Img_shift=circshift(Img,[x,y]);

row=X
cols=Y
n=3
offset=486-x

% Filtering

Filter=D_Filter(row,cols,0,offset);
Filter=1./(1+(Filter./30).^(2*n));

Img_shift_filtered= Filter.*Img_shift;
Img_shift_filtered =circshift(Img_shift_filtered,[-offset,0]);
Imaginary_part=circshift(Img_shift_filtered,[-x,-y]);

Real_shift_filtered =Filter.*Real_shift;
Real_shift_filtered =circshift(Real_shift_filtered,[-offset,0]);
Real_part=circshift(Real_shift_filtered,[-x,-y]);

% Convolve, Inverse FFT, phase calculation

C_comb=complex(Real_part, Imaginary_part);
Y_Filtered=ifft2(C_comb);
wphase=atan2(imag(Y_Filtered), real(Y_Filtered));
```

Appendix B: Least Squares Method for Phase Calculation

$$I_n = a + u \cos \phi_{R_n} + v \sin \phi_{R_n}$$

$$\sum_{n=1}^{m} (a + u \cos\phi_{R_n} + v \sin\phi_{R_n} - I_n)^2 = 0$$

$$\frac{\partial I}{\partial a} = \sum I_n = \sum a + \sum u \cos\phi_{R_n} + \sum v \sin\phi_{R_n}$$

$$\frac{\partial I}{\partial u} = \sum I_n \cos \phi_{R_n} = \sum a \cos \phi_{R_n} + \sum u \cos^2(\phi_{R_n}) + \sum v \cos \phi_{R_n} \sin \phi_{R_n}$$

$$\frac{\partial I}{\partial v} = \sum I_n \sin \phi_{R_n} = \sum a \sin \phi_{R_n} + \sum u \cos \phi_{R_n} \sin \phi_{R_n} + \sum v \sin^2(\phi_{R_n})$$

$$\Omega(x,y) = arctan \left[\frac{-v(x,y)}{u(x,y)} \right]$$

APPENDIX C: MatLab program for phase calculation based on 4, 8, and 16 phase stepping algorithms.

```matlab
clc, clear all, close all;

folder_name_Def='F:\WPI_MS_Thesis\TPU_Testing_722011\Pos1\Results';

% 4 Phase Step Algorithm

step=4;
phase_shift=(360/step)*(pi/180);

for i=1:4
        filename_Def=strcat(folder_name_Def,'\','4step_',num2str(i),'.rti');
        image = readRTI(filename_Def);
        Deformed(:,:,i)=image';
        Deformeds(:,:,i)=Deformed(:,:,i).*sin(phase_shift.*(i-1));
        Deformedc(:,:,i)=Deformed(:,:,i).*cos(phase_shift.*(i-1));
end

        catA=cat(3,Deformeds(:,:,:));
        num=-1.*sum(catA,3);

        catB=cat(3,Deformedc(:,:,:));
        den=sum(catB,3);
        phase_4step=atan2(num,den);

        clear step phase_shift Deformed Deformeds Deformedc catA catB num den
image

% 8 Phase Step Algorithm

step=8;
phase_shift=(360/step)*(pi/180);

for i=1:8
        filename_Def=strcat(folder_name_Def,'\','8step_',num2str(i),'.rti');
        image = readRTI(filename_Def);
        Deformed(:,:,i)=image';
        Deformeds(:,:,i)=Deformed(:,:,i).*sin(phase_shift.*(i-1));
        Deformedc(:,:,i)=Deformed(:,:,i).*cos(phase_shift.*(i-1));
end

        catA=cat(3,Deformeds(:,:,:));
        num=-1.*sum(catA,3);

        catB=cat(3,Deformedc(:,:,:));
        den=sum(catB,3);
        phase_8step=atan2(num,den);

        clear step phase_shift Deformed Deformeds Deformedc catA catB num den
image
```

```matlab
% 16 Phase Step Algorithm

step=16;
phase_shift=(360/step)*(pi/180);

for i=1:16
        filename_Def=strcat(folder_name_Def,'\','16step_',num2str(i),'.rti');
        image = readRTI(filename_Def);
        Deformed(:,:,i)=image';
        Deformeds(:,:,i)=Deformed(:,:,i).*sin(phase_shift.*(i-1));
        Deformedc(:,:,i)=Deformed(:,:,i).*cos(phase_shift.*(i-1));
end

        catA=cat(3,Deformeds(:,:,:));
        num=-1.*sum(catA,3);

        catB=cat(3,Deformedc(:,:,:));
        den=sum(catB,3);
        phase_16step=atan2(num,den);

        clear step phase_shift Deformed Deformeds Deformedc catA catB num den
image

figure
subplot(1,3,1)
imagesc(phase_4step)
title('4 Phase Step')
xlabel('pixels')
ylabel ('pixels')

subplot(1,3,2)
imagesc(phase_8step)
title('8 Phase Step')
xlabel('pixels')
ylabel ('pixels')

subplot(1,3,3)
imagesc(phase_16step)
colormap('gray')
title('16 Phase Step')
xlabel('pixels')
ylabel ('pixels')
```

APPENDIX D: Projection System Components

The packaged prjoector from Vialux used a 30mW light emitting diode (LED) at 624 nm center wavelength, model number LED-OM model HP-95-R, Fig. D.1.

Fig. D.1. Projection System.

The projection system is controlled by a field-programmable gate array (FPGA) integrated circuit, Fig. D.2. The D4100 starter board was manufactured by DLP Texas Instruments. Flex cables are used for high speed and high data transfer between the FPGA board and the digital micro-mirror device (DMD).
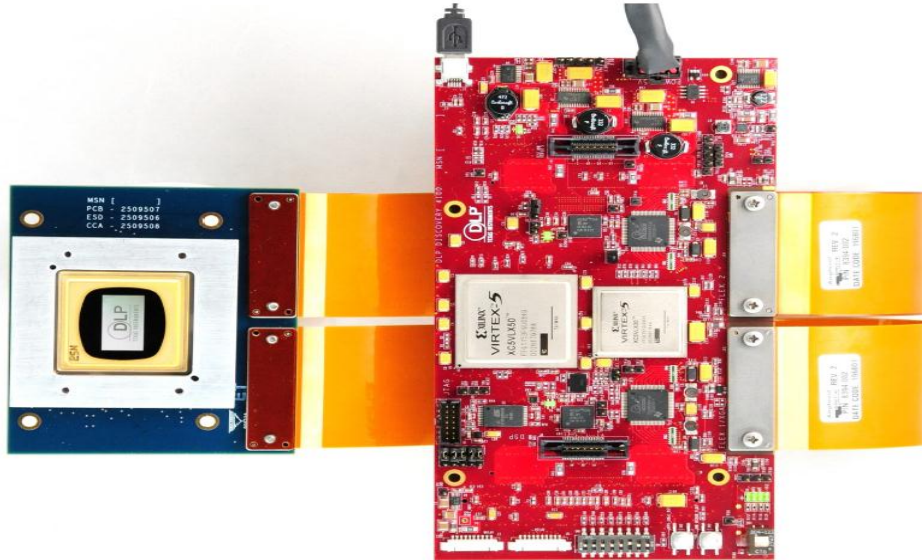
Fig. D.2. D4100 Explorer FPGA.

The DMD microchip in Fig. D.3 is of format 0.95" 1080 p A-Type, packaged by Texas Instruments. Basic specifications include the dimensions at 170 x 190 x 200 mm^3 and the weight of 1800 grams. The image width is >435 mm, working distance >300 mm, projection offset 0%, and throw ratio 0.7.
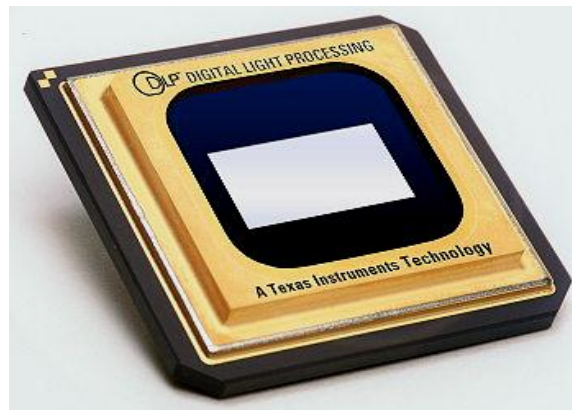

Fig. D.3. DMD Device from Texas Instruments.

Appendix E: Uncertainity Analysis of z-depth Measurement

$L := 114.3$cm $\quad\quad\quad \delta L := 0.05$cm

$D := 61.0$cm $\quad\quad\quad \delta D := 0.05$cm

$\lambda := 2.52$cm $\quad\quad\quad \delta\lambda := .0005$cm

$\Omega := \pi$ rad $\quad\quad\quad \delta\Omega := 0.0025$rad

$$Z(L, \Omega, \lambda, D) := \frac{L \cdot \Omega \cdot \lambda}{2 \cdot \pi \cdot D}$$

Height uncertainty at Ω=πrad:

$$\delta Z(L, \Omega, \lambda, D) := \sqrt{\left(\delta L \frac{d}{dL} Z(L, \Omega, \lambda, D)\right)^2 + \left(\delta\Omega \frac{d}{d\Omega} Z(L, \Omega, \lambda, D)\right)^2 + \left(\delta\lambda \frac{d}{d\lambda} Z(L, \Omega, \lambda, D)\right)^2 .. + \left(\delta D \frac{d}{dD} Z(L, \Omega, \lambda, D)\right)^2}$$

$$\delta Z(L, \Omega, \lambda, D) = 29.259 \mu m$$

Percent contribution at Ω=π rad:

$$pL(L, \Omega, \lambda, D) := \left(\frac{\delta L \frac{d}{dL} Z(L, \Omega, \lambda, D)}{\delta Z(L, \Omega, \lambda, D)}\right)^2 \quad\quad\quad p\Omega(L, \Omega, \lambda, D) := \left(\frac{\delta\Omega \frac{d}{d\Omega} Z(L, \Omega, \lambda, D)}{\delta Z(L, \Omega, \lambda, D)}\right)^2$$

$$pL(L, \Omega, \lambda, D) = 0.125 \quad\quad\quad\quad\quad\quad\quad\quad\quad\quad p\Omega(L, \Omega, \lambda, D) = 0.412$$

$$p\lambda(L, \Omega, \lambda, D) := \left(\frac{\delta\lambda \frac{d}{d\lambda} Z(L, \Omega, \lambda, D)}{\delta Z(L, \Omega, \lambda, D)}\right)^2 \quad\quad\quad pD(L, \Omega, \lambda, D) := \left(\frac{\delta D \frac{d}{dD} Z(L, \Omega, \lambda, D)}{\delta Z(L, \Omega, \lambda, D)}\right)^2$$

$$p\lambda(L, \Omega, \lambda, D) = 0.026 \quad\quad\quad\quad\quad\quad\quad\quad\quad\quad pD(L, \Omega, \lambda, D) = 0.437$$

Appendix F: CAD Drawing of Mouting System to Van